Aalto University
School of Chemical
Engineering

Laura Äkräs

3D BIOPRINTING INKS BASED ON CELLULOSE NANOFIBRILS AND COLLOIDAL LIGNIN PARTICLES

Master's Programme in Chemical, Biochemical and Materials Engineering

Major in Fibre and Polymer Engineering

Master's thesis for the degree of Master of Science in Technology submitted for inspection, Espoo, 15th February, 2019.

Supervisor: *Professor Monika Österberg*

Instructor: *D. Sc. (Tech.) Mika Sipponen*

Aalto University
School of Chemical
Engineering

Author Laura Äkräs

Title of thesis 3D bioprinting inks based on cellulose nanofibrils and colloidal lignin particles

Degree Programme Master's programme in Chemical, Biochemical and Materials Engineering

Major Fibre and Polymer Engineering

Thesis supervisor Professor Monika Österberg

Thesis advisor(s) / Thesis examiner(s) D. Sc. (Tech.) Mika Sipponen

Date 15.02.2019 **Number of pages** 117+13 **Language** English

Abstract

Three-dimensional (3D) bioprinting has been utilized for decades, and today its popularity is up surging. 3D bioprinting is based on the use of the natural, non-toxic, and tissue-mimicking biomaterials which are extruded in the form of bioinks to generate different structures layer-by-layer, from a simple cylinder to the shape of an ear. This method is gaining popularity in the field of regenerative medicine in which the focus is in regenerating and replacing injured tissues and organs. However, the major obstacles in the utilization of the current biomaterials are their insufficient properties, especially in the case of the mechanical strength. Therefore, new materials, hybrid materials, and material composites need to be developed.

In this Master's thesis, the novel CLP-CNF-alginate bioink compositions were prepared with the cellulose nanofibril (CNF) concentrations of 2.5 wt%, alginate concentrations of 0.5 wt%, and colloidal lignin nanoparticle (CLP) concentrations relative to the dry weight of CNF. The rheological properties of these bioinks were measured through the dynamic viscosity and amplitude sweep measurements, whereas the printability of the bioinks was tested in 3D bioprinting. This was followed by the compression tests and the evaluation of the hydrogels in different storage conditions. These various stability tests included freeze-drying, re-wetting, humidity chamber, salt-water solution, and free-standing at room temperature.

The addition of CLPs into the CNF-alginate hydrogel offered many advantages. Most importantly, the existence of CLPs enhanced the printability and structural stability of the hydrogels directly after 3D bioprinting. On the other hand, the addition of CLPs increased the dimensional stability of the CLP-CNF-alginate hydrogels in high humidity and salt-water solutions. Nevertheless, dissolution in the salt-water solution, fast drying in the room air, and the non-toxicity of these hydrogels with the degradation rates inside the human body require further research. However, these multiple intrinsic properties of the CLP-CNF-alginate hydrogels make them a multifunctional material for the regenerative medicine.

Keywords Nanofibrillated cellulose (CNF), colloidal lignin nanoparticles (CLPs), 3D bioprinting, hydrogels, printability, stability, regenerative medicine, kidney regeneration

Aalto-yliopisto
Kemian tekniikan
korkeakoulu

Tekijä Laura Äkräs

Työn nimi 3D-bioprinttaustahnat selluloosan nanofbrilleihin ja kolloidisiin ligniinipartikkeleihin perustuen

Koulutusohjelma Kemian-, biokemian- ja materiaalitekniikan koulutusohjelma

Pääaine Kuitu- ja polymeeritekniikka

Työn valvoja Professori Monika Österberg

Työn ohjaaja(t)/Työn tarkastaja(t) TkT Mika Sipponen

Päivämäärä 15.02.2019 **Sivumäärä** 117+13 **Kieli** Englanti

Tiivistelmä

3D-bioprinttausta on hyödynnetty vuosikymmeniä, mutta nykyään sen suosio on räjähdysmäisessä kasvussa. 3D-bioprinttauksessa käytetään luonnonmukaisia, myrkyttömiä ja kudoksia jäljitteleviä biomateriaaleja, jotka ruiskutetaan biotahnojen muodossa, kerros kerrokselta, muodostamaan erilaisia rakenteita, aina yksinkertaisesta lieriöstä korvanmuotoisiin rakenteisiin asti. Menetelmä on suosittu regeneroivassa lääketieteessä, jossa keskitytään vahingoittuneiden tai sairaiden kudosten sekä elinten korvaamiseen. Suurimmat haasteet nykyisten biomateriaalien hyödyntämisessä liittyvät niiden riittämättömiin ominaisuuksiin, erityisesti mekaanisten ominaisuuksien osalta. Tämän vuoksi uusia materiaaleja, hybridimateriaaleja ja materiaalikomposiitteja on tärkeä kehittää.

Tässä diplomityössä valmistettiin uusia CLP-CNF-alginaatti -biotahnoja, jotka sisälsivät 2,5 p-% nanofibrilloitua selluloosaa (CNF), 0,5 p-% alginaattia ja kolloidisia ligniinipartikkeleita (CLPs) CNF-kuitujen kuivapainon mukaisesti. CLP-CNF-alginaatti -biotahnojen reologiset ominaisuudet mitattiin dynaamisten viskositeetti- ja amplitudimittausten avulla. Biotahnojen printattavuutta sen sijaan tutkittiin 3D bioprinttauksessa, mitä seurasivat kompressiotestit ja varastointimittaukset. Varastointimittauksiin kuuluivat hydrogeelien kylmäkuivaus, uudelleen kostutus sekä säilytys kosteuskammiossa, suolavesiliuoksessa ja huoneilmassa.

Ligniinipartikkeleiden lisäys CNF-alginaatti -hydrogeeliin tarjosi monia etuja. Ligniinipartikkelit paransivat erityisesti hydrogeelien printattavuutta sekä rakenteen stabiilisuutta 3D bioprinttauksen jälkeen. Ligniinipartikkeleiden lisäys kasvatti myös hydrogeelien rakenteellista pysyvyyttä korkeassa kosteudessa ja suolaliuoksessa. Hydrogeelien liukeneminen suolaliuoksessa, nopea kuivuminen huoneilmassa sekä myrkytön hajoaminen elimistössä vaativat kuitenkin lisätutkimusta. Yleisesti ottaen CLP-CNF-alginaatti -hydrogeelit ovat monikäyttöisiä materiaaleja regeneroivan lääketieteen tarkoituksiin.

Avainsanat Nanofibrilloitu selluloosa (CNF), kolloidiset ligniinipartikkelit (CLPs), 3D-bioprinttaus, hydrogeelit, printattavuus, stabiilisuus, regeneroiva lääketiede, munuaisten regenerointi

PREFACE

It is difficult to realize that my time as a Master's thesis student is slowly coming to an end. It makes so many emotions to rise inside me. At the same time, I am relieved, happy that this challenging time full of work, learning and self-growth is finally over, and yet, a little bit nostalgic. Is it indeed over? Above all, I feel proud, proud of myself. Still a few months ago, I could not have even imagined what I had gone through during this time. How much I would need to test my boundaries, and yet, survive as a winner. It is a superb feeling.

However, I am also thankful for the people around me. Without the effort and support of so many people, I would not have come this far. Firstly, I want to thank my Professor Monika Österberg for the opportunity to make a Master's thesis about this interesting topic of 3D bioprinting. Medicine and engineering combined in this one marvelous topic was more than a good choice for me. I have enjoyed my journey when getting to know more about this extremely interesting research area of 3D bioprinting in the field of regenerative medicine. I warmly thank you Monika, for making these new experiences possible for me!

I also want to thank my instructor D. Sc. (Tech.) Mika Sipponen for the kind help through the Master's thesis and my co-instructor M. Sc. Xue Zhang for the marvelous assistance, particularly with 3D bioprinting and rheology measurements. You guys helped me when I really needed it and created the important base for my independent work. My thanks also go to wonderful M. Sc. (Tech.) Rubina Adjary and Dr. Siqi Huan, the 3D bioprinting experts, who were a vital part of my 3D bioprinting journey, and to a very sweet rheology expert M. Sc. (Tech.) Risto Koivunen who selflessly helped me with the rheometer, when I was in a serious trouble. Last but not least, I want to thank my dear family who supported me through this time and gave me strength when I felt I run out of energy. You were my rock! YOU, my dear ones, made this all possible!

Without further parley, my dear reader, I wish you a pleasant journey in the world of hydrogels,

Laura Äkräs

Laura Äkräs

ABBREVIATIONS

AKI	Acute renal injury
SA	Alginate
$CaCl_2$	Calcium chloride
CKD	Chronic kidney injury
NFHs	Cellular-structured nanofibrous hydrogels
CNCs	Cellulose nanocrystals
CD	Collecting duct
CLPs	Colloidal lignin nanoparticles
CT	Computed tomography
CAD	Computer-aided design
CAM	Computer-aided manufacturing
DT	Distal tubule
DLS	Dynamic light scattering
DMA	Dynamic mechanical analysis
ESCs	Embryonic stem cells
E-CNF	Enzymatically-treated CNF
ESRD	End-stage renal disease
ECM	Extracellular matrix
Gel	Gelatin
GG	Gellan gum
HEK	Human embryonic kidney
HA	Hyaluronic acid
HA	Hydroxyapatite
iPSCs	Induced pluripotent stem cells
DBB	Inkjet bioprinting
LBB	Laser-assisted bioprinting
LCNF	Lignocellulosic nanofibrils

LS	Lignosulfonate
LVR	Linear viscoelastic region
MRI	Magnetic resonance imaging
M	Mannuronic acid
MetCMC	Methylcellulose
MBB	Microextrusion bioprinting
MCF	Microfibrillated cellulose
MCNF	Morpholine pretreated CNF
CMCNF	Morpholine preteated and carboxymethylated CNF
CNF	Nanofibrillated cellulose
NaOH	Natriumhydroxide
PRP	Platelet-rich plasma
PLA	Polylactic acid
PDI	Polydispersity index
PEGDA	Polyethyleneglycol-diacrylate
PDMS	Polymethylsiloxane
PT	Proximal tubule
PTC	Proximal tubule cells
SF	Silk-fibroin
SA	Sodium alginate
SKL	Softwood kraft lignin
SLA	Stereolithography
3D	Three-dimensional

CONTENTS

INTRODUCTION

3D printing has been an emerging technology worldwide, offering many possibilities in different industries. In the past few decades, also 3D bioprinting has gained more and more popularity and has became one of the promising technologies for example in medicine (Zhang et al., 2018). This is due to the few main properties related to the 3D bioprinting, which are bio-based and thus biocompatible materials used in 3D bioprinting, and possibility to distribute cells, biochemical factors, proteins, and drugs at the desired locations (Zhang et al., 2018; Francis & Bulletin, 2015; Piras et al., 2017). Due to these many benefits of 3D bioprinting, it has became a promising method for regenerative medicine (Zhang et al., 2018; Savage, 2016). 3D bioprinting could be used for example to cut organ shortage which is inevitable because of the aging population worldwide (Peloso et al., 2016; Radenkovic, Soulouk, & Seifalian, 2016).

The different main technologies of 3D bioprinting are inkjet bioprinting, extrusion bioprinting and laser-assisted bioprinting. Inkjet bioprinters use thermal or acoustic forces to eject drops of liquid onto a substrate (Dzobo et al., 2018; Murphy & Atala, 2014), whereas extrusion-based bioprinters use an air-forced pump, a mechanical screw, or a plunger (Dzobo et al., 2018; Mandrycky et al., 2016). On the other hand, laser-assisted bioprinters are based on the laser pulse which vaporizes a portion of the donor layer, creating a high pressure bubble at the interface of the bioink (Dzobo et al., 2018; Mandrycky et al., 2016; Murphy & Atala, 2014). A recent, competitive 3D bioprinting technology is strereolithography bioprinting which is based on the polymerization by UV light, near-UV blue light, or visible light, utilizing the digital mirror arrays (Wang et al., 2015; Wang et al., 2018).

These 3D bioprinting types have different characteristics. Microextrusion can be used for the bioinks with the widest viscosity range, but it causes the highest cell densities, which in turn decreases the cell viability (Axpe & Oyen, 2016; Mandrycky et al., 2016; Murphy & Atala, 2014). Inkjet bioprinting offers a high printing speed and resolution, but it can be used only for the inks with limited viscosities (Axpe & Oyen, 2016;

Mandrycky et al., 2016; Ozbolat et al., 2017). In the end, laser-assisted bioprinting has a wide viscosity range, possibility for a high printing speed, and, most importantly, the lowest cell densities which results in the highest cell viability (Axpe & Oyen, 2016; Mandrycky et al., 2016; Murphy & Atala, 2014; Ozbolat et al., 2017). As a competitive technology, stereolithography bioprinting has a higher resolution, printing speed, and cell viability (Wang et al., 2015; Wang et al., 2018), when compared to the inkjet bioprinting and laser-assisted bioprinting, and overall shorter printing time (Wang et al., 2015). The suitable 3D bioprinting technology must be considered in the light of the materials used and the desired properties of the end application (Murphy & Atala, 2014).

Despite the many positive factors of 3D bioprinting, it still faces multiple challenges. 3D bioprinting utilizes the main technologies from 3D printing, but all the old technologies do not fit with the cell-friendly and non-toxic demands of 3D bioprinting (Axpe & Oyen, 2016). Other difficulties include the high costs associated with 3D bioprinting, the technical difficulties in mimicking the complex tissue and organ structures inside the human body, the translation of the 3D printed structures into pre-clinical and clinical use, establishing abundant cell sources, and, on the other hand, finding more biomaterials with desirable properties for the different functions in bioinks and in hydrogels (Francis & Bulletin, 2015; Radenkovic, Soulouk, & Seifalian, 2016; Sadri-Ardekani & Atala, 2016; Sultan et al., 2017; Lee & Dai, 2017).

Thus, one solution is to find more suitable biomaterials (Lee & Dai, 2017). A few common and widely researched biopolymers are, e.g., alginate, hyaluronic acid, and collagen (Ullah et al., 2018). Lately, also CNF and cellulose nanocrystals (CNCs) have gained a lot of attention due to their many good properties (Dai et al., 2019; Xu et al., 2018). In this Master's thesis, one biopolymer option, lignin in the form of CLPs, has been researched and its suitability for bioinks has been evaluated. According to the hypothesis, the addition of CLPs was expected to prevent hydrogel shrinking upon drying. Kidneys were selected as the target organ for the possible regenerative applications of CLP-CNF-alginate bioinks. The functional unit of the kidney is nephron which task is to maintain the body homeostasis by regulating the levels of fluid and

electrolytes, using glomerular filtration, selective tubular reabsorption, and secretion (Chuah & Zink, 2017; Lawrence et al., 2018; Moon et al., 2016). This Master's thesis starts with the literature review, materials and methods describtion and ends with the results and conclusions.

LITERATURE REVIEW

1. Regenerative medicine

1.1 *The discipline*

Regenerative medicine (RE) is a field of science, employing both engineering and biology, providing novel therapies that ultimately aim to restore normal function to the damaged or diseased tissues and organs within the human body by replacing or regenerating human cells, tissues, and organs (Atala & Murphy, 2015; Dzobo et al., 2018; Peloso et al., 2016; Sadri-Ardekani & Atala, 2016). This replacing or regeneration process requires cells, natural or artificial scaffold materials, growth factors and/or gene editing, depending on the end application type (Peloso et al., 2016). Advances in tissue engineering (TE), cell biology, nuclear transfer, biological molecule discovery, and biomaterial science have led to new developments and options for cellular therapies, engineered tissues, and organs for the purposes of the regenerative medicine, also considering the techniques of cell harvest, culture, expansion, transplantation, and polymer design (Atala & Murphy, 2015; Sadri-Ardekani & Atala, 2016).

The cells used in the regenerative medicine are embryonic stem cells (ESCs), stem cells found in the adult tissues, and induced pluripotent stem cells (iPSCs) (Murphy & Atala, 2013; Peloso et al., 2016). Among these, embryonic and adult stem cells exist in the human body at all stages of life, however, their stemness potential decreases in time through senescence (Peloso et al., 2016). The highest stemness potential can be found in embryonic stem cells which are in the human embryos. These embryonic

stem cells can differentiate into any cells in the human body (Li et al., 2016; Murphy & Atala, 2013; Peloso et al., 2016). Adult stem cells also have an ability to differentiate, but only into certain cells. However, some adult stem cells can differentiate into cells outside their repertoire (Peloso et al., 2016). These autologous cells do not cause a host immune response, but have the limited regeneration capacity and technical restrictions considering the *in vitro* culture of these cells (Dzobo et al., 2018). Lately, through groundbreaking technology and the understanding of stemness, a new and potential stem cell type called iPSCs have been developed (Atala & Murphy, 2015; Peloso et al., 2016). They have been generated through somatic cell reprogramming using, e.g., retroviral and lentiviral vectors, therefore avoiding ethical production challenges, and have the same function as embryonic stem cells (Murphy & Atala, 2013; Atala & Murphy, 2015).

Many induced pluripotent stem cells can be prepared simultaneously, which enables the use of this stem cell type in clinical therapies (Atala & Murphy, 2015). This is a benefit because ESCs have limitations regarding the clinical translation, e.g., ethical challenges due to the destruction of embryo during the ESC production, formation of special tumors called teratomas, and potential to evoke immune respone due to the allogeneic nature of the cell source (Murphy & Atala, 2013). Clinical translation of iPSCs has its own challenges, to mention a few, the potential of iPSCs to form tumors, difficulties in scalable iPSCs production, and patient selection for the clinical therapies (Li et al., 2016). However, embryonic stem cells and pluripotent stem cells are capable of self-renewal (Lou et al., 2014), and characterized by remarkable anti-inflammatory and immune-modulatory properties (Peloso et al., 2016). These good features offer many benefits when used in clinical therapies in the regenerative medicine.

The subfields of regenerative medicine are cell therapy, tissue engineering and production of artificial organs, and regenerative pharmacology (Atala et al., 2008; Atala & Murphy, 2015). In cell therapy, different stem cell types are utilized in treating diseases, and thus, the ability to understand and efficiently control the function and proliferation of stem cells into specific tissues, with or without chemical inducers and growth factors, has been the central focus in this subfield (Atala & Murphy, 2015;

Kenry et al., 2018). The clinical use of bone marrow–derived stem cells to reconstitute the hematopoietic system acted as a start for the current cell therapy strategies in the 1950s, and nowadays several clinical trials are conducted (Atala & Murphy, 2015). On the other hand, tissue engineering aims at restoring and sustaining functions of diseased organs through the maximization of the innate ability of tissues to repair or regenerate the injury by integrating scaffolds materials with living, biological cells (Kenry et al., 2018; Peloso et al., 2016), or the *ex vivo* bio-fabrication of a diseased organ (Peloso et al., 2016). New approaches have been developed for this second subfield, recently also by decellularization (Schmitt et al., 2017), and 3D bioprinting (Dzobo et al., 2018), but more research is needed, especially when it comes to the regeneration of complex, solid organs (Savage, 2016).

In the end, the last subfield of regenerative medicine is called regenerative pharmacology (Atala & Murphy, 2015). In short, this subfield studies the mechanisms, signaling pathways, and substrates, that mediate pluripotency and differentiation of various stem cells, for the therapeutic use. Traditionally, regenerative pharmacology utilizes expensive growth mediums, such as commercially available and popular mTeSR© medium (StemCell Technologies) for both ESCs and iPSCs growth and differentiation (Atkinson, Lako, & Armstrong, 2013). Recently, the development of small molecule-driven cell renewal of tissue-specific stem cells and their induction into a differentiated phenotype has also shown promise (Atala & Murphy, 2015; Atkinson, Lako, & Armstrong, 2013). These different and cost-effective small molecule inhibitors and activators, such as Butyryl CoA and chlorate, can boost the pluripotency, self-renewal, and survival of different stem cells, at the same time enhancing differentiation protocols (Atkinson, Lako, & Armstrong, 2013). These subfields of regenerative medicine are closely linked. The understanding of human cell function through cell therapy approaches and, on the other hand, the adequate tools for differentiation of the cells from regenerative pharmaceutics are essential parts of cell culturing and tissue and organ regeneration in tissue engineering.

1.2 *Strategies of regenerative medicine*

The core goal of regenerative medicine is to obtain functional cells on demand for the lost cells due to diseases, injuries, and aging (Li et al., 2016). This requires advances in the understanding of stem cell differentiation, induced pluripotency, and the ability to directly reprogram cells into another cell type (Murphy & Atala, 2013). iPSCs have shown potential to meet this goal (Li et al., 2016). Direct differentiation of iPSC, by the cell-based strategies of establishing direct differentiation protocols for every cell type in the body through understanding the signaling pathways that control the embryonic development, or by using small molecules, could be used for *in vivo* transplantation, studying diseases *in vitro*, and discovering new drugs (Li et al., 2016).

Tissue- and organ-based strategies of regenerative medicine include miniature human organoids, decellularization, and, on the other hand, 3D printing and 3D bioprinting (Atala & Murphy, 2015). Differentiation protocols of stem cells are used in producing miniature human organoids, which are formed through the autonomous self-assembly of the cells, resulting in the generation of complex 3D organoids that recapitulate the normal tissue or organ development (Susaimanickam et al., 2017). Miniature human organoids are biological tools that can accurately model physiological tissue function at the micro-scale, having potential applications in disease modeling, drug discovery, and toxicity testing (Atala & Murphy, 2015). These organs-on-a-chip are being developed for, e.g., for the lung, liver, heart, skin, and kidney (Atala & Murphy, 2015). Furthermore, a combined system of organoids representing a body-on-a-chip is in the middle of development, capable of modeling the complex interactions between multiple organ systems (Atala & Murphy, 2015), and predicting drug efficacy (Kimura, Sakai, & Fujii, 2018). This body-on-a-chip or human-on-a-chip is based on the microfluidic devices, containing the functions of multiple organs and tissues (Kimura, Sakai, & Fujii, 2018).

On the other hand, in the decellularization process, all the cellular components and primary immunogenic factors, such as cellular proteins and DNA, have been removed from an organ with the structural architecture left intact (Moon et al., 2016). This is

based on the perfusion of an organ with detergents and other chemical agents through the vasculature, maintaining the structural integrity of the organ's extracellular matrix (ECM) (Moon et al., 2016), and the inherent vascular network (Schmitt et al., 2017). Furthermore, the resulting acellular matrix is repopulated or recellularized with organ-specific cells, undergoing some degree of self-organization (Moon et al., 2016). This technology has provided a promising approach for the production of transplantable organ constructs (Moon et al., 2016), and for tissue engineering of solid tissues with an adequate vascularization (Schmitt et al., 2017).

In the end, producing tissues on demand by 3D printing and 3D bioprinting would revolutionize medicine (Dzobo et al., 2018), by creating readily available transplant organs and tissues, and, at the same time, eliminating the waiting list for replacement parts (Savage, 2016). Printed constructs might be stronger than grafts from the donated tissue, fill the tiny crevices that no surgery could address, leading to greater overall strength, and avoid the need to cut healthy tissue through printing in the shape of the damage (Savage, 2016). In addition, in the future, successive layers of biocompatible material laden with cells might be able to deposit straight into a defect and the human body could be enhanced with new types of tissues (Savage, 2016). The possibilities seem science fiction, but currently, a number of bioengineered tissues are in various stages of development, and several clinical trials have begun (Sadri-Ardekani & Atala, 2016). Succesful outcomes from these clinical trials will help to ensure the future of the regenerative medicine therapies (Sadri-Ardekani & Atala, 2016).

1.3 *The kidneys*

The functional unit of kidney is nephron which is essential for most renal functions (Chuah & Zink, 2017; Lawrence et al., 2018). Human kidney function is underpinned by approximately 1 million nephrons, the number of these nephrons varying substantially for each person (Chuah & Zink, 2017). The nephron consists of the glomerulus and the renal tubule. Filtration of the blood occurs in the glomerulus, whereas the glomerular filtrate flows into the renal tubule, starting from the renal

proximal tubule (PT) located next to the glomerulus. The loop of Henle connects the PT with the distal tubule (DT). DT leads into the collecting duct (CD), and the branched CD tree connects the nephrons with the ureter. (Chuah & Zink, 2017)**.**

The nephrons are in medullas surrounded by the renal interstititum. It consists of cells embedded in a complex ECM, whereas the normal interstitium is constructed of capillary endothelial cells, dendritic cells, and structural cells which can also be referred as fibroblasts. Collagen molecules play a major role in this ECM, mostly contributing to the structural integrity. On the other hand, modulating cell differentiation, cell growth, and adhesion are also important functions of collagen. In the kidney, the most abundant collagens are type I and III collagen. (Alexakis et al., 2006). The Figure 1 represents more detailly the rough and finer structure of the complex kidney.

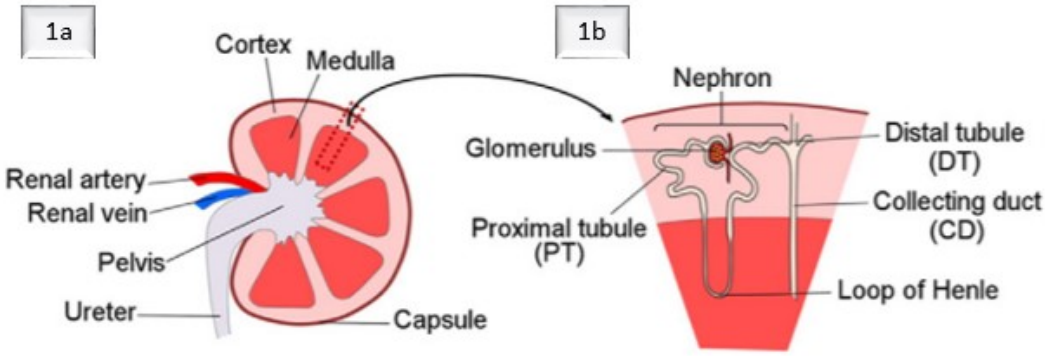

Figure 1. *Structure of the kidney.* **1a.** *The rough structure of kidney consists of the shell of the kidney called capsule, the tougher region below the capsule called cortex, the small assemblies referred to as medullas, in which nephrons are located, and renal arteries and veins which are responsible for the nutrient, oxygen, and carbon dioxide transfer of the nephrons and other cells. The structure of the kidney ends with pelvis, in which the urea is collected through the CD, and the ureter.* **1b.** *Finer structure of the kidneys inside the medulla is constructed of nephron (glomerulus, PT, and DT), and CD. Nephrons are the essential functional units of the kidneys responsible for many kidney functions. (Adapted from Chuah & Zink (2017)).*

Kidneys or, most importantly, proximal tubule cells (PTC) have manifold functions. For instance, they control the pH of blood and urine and reabsorb most of the water, glucose, peptides and proteins from the glomerular filtrate, are important for electrolyte and mineral homeostasis, produce the active form of vitamin D and erythropoietin (EPO), clear metabolic wastes, toxicants and xenobiotics by active

transport and secretion of these compounds from the bloodstream into the glomerular filtrate, and express a large variety of phase I and phase II enzymes for the metabolism of toxicants, organic compounds and drugs, such as cytochrome P450 enzymes (Chuah & Zink, 2017; Moon et al., 2016).

However, when the kidney is injured, the damaged renal tissue will undergo several disease states and stages, including acute and chronic kidney symptoms (Moon et al., 2016). Acute renal injury (AKI) is generally defined as a sudden increase in the serum creatinine concentration, accompanied by decreased urine output (Moon et al., 2016). In pathological aspects, AKI shows for example tubular necrosis and apoptosis, changes of the filtration barrier, glomerular misfiltration, vasoconstriction and tubular obstruction, interstitial swelling, and activation of proteolytic enzymes (Moon et al., 2016). When this kidney impairment lasts more than three months, the patient has developed a chronic kidney disease (CKD) (Razmaria, 2016). CKD results in decreased urine production and kidney failure (Razmaria, 2016). When AKI and CKD develop into more severe states, end-stage renal disease (ESRD), the conditions affect multiple organs system (Moon et al., 2016).

1.4 *Regeneration of kidneys*

With the ageing population, increasing number of failing organs and organ shortage is going to occur (Radenkovic, Soulouk, & Seifalian, 2016). The current treatments are not sufficient enough to face this challenge due to the paucity of suitable organ donors, the practical hurdles of collecting and storing the organs, the high costs of transplantation (Dzobo et al., 2018; Radenkovic, Soulouk, & Seifalian, 2016), and the immune responses caused by transplants and mortality of lifelong immunosuppression of dialysis (Radenkovic, Soulouk, & Seifalian, 2016). Even if dialysis is capable of replacing renal filtration function by removing certain toxins from the blood, it is unable to restore for example the production of EPO and activation of vitamin D (Moon et al., 2016). This decreases the quality of life and long-term survival (Moon et al., 2016). Current treatment of AKI and CKD is limited to this life-long dialysis (Moon et al., 2016).

Better options for the treatment of for example AKI and CKD is cell-based approach in which the damaged regions are regenerated with functional renal specific cells (Moon et al., 2016). Some of the cell-based therapies using transplantation of autologous, primary renal cells and stem cells are now clinically applicable, whereas the pre-clicinal and clinical applications of the fully functional, engineered renal constructs stay challenging (Moon et al., 2016). On the other hand, the only definitive treatment for ESRD is kidney transplantation (Moon et al., 2016). It is dramatically limited by an inadequate supply of transplantable grafts and by the heavy toxicity related to lifelong immunosuppression due to the inadequate etiology and pathophysiology (Peloso et al., 2016).

However, tissue engineering and regenerative medicine are developing multiple approaches and strategies to enhance the treatments for AKI, CKD, and ESRD (Moon et al., 2016; Peloso et al., 2016). These strategies for the treatments include aforementioned cell therapies and tissue engineered 3D renal constructs for AKI and CKD, and whole kidney engineering for ESRD (Moon et al., 2016). For example, several types of mesenchymal stem cells (MSCs) have shown promising results in kidney repair, and skeletal muscle-derived stem/progenitor cells (MDSPCs) have been considered as a potential strategy for the treatment of AKI (Pavyde, Usas, & Maciulaitis, 2016). Decellularization of organs has shown promise in whole kidney engineering, but many challenges should be addressed before the clinical applications (Moon et al., 2016). Bioreactors, mimicking the *in vivo* environment, delivering nutrients within perfused medium, and monitoring physiological parameters of tissue development, could be used to develop a reproducible recellularization strategy for the requirements of clinical applications (Lin et al., 2016).

Other strategies are developmental biology in the form of miniature human organoids, 3D bioprinting, and a kidney-on-a-chip technology (Peloso et al., 2016). Kidney organoids have been studied lately (Takasato et al., 2015; Takasato & Little, 2016), many kidney-on-a-chip researches have been conducted based on, e.g., renal tubule epithelial cells, and 3D bioprinting can already be used in teaching models of

renal tumor localization or kidney surgigal models for planning and training purposes (Lin et al., 2016). Ultimately, four-dimensional (4D) printing is the latest, emerging strategy of regenerative medicine in kidney bioengineering, producing products capable of adjusting themselves according to their surroundings (Lin et al., 2016). In the Figure 2, the different regenerative solutions for the kidney bioengineering can be seen in more detail.

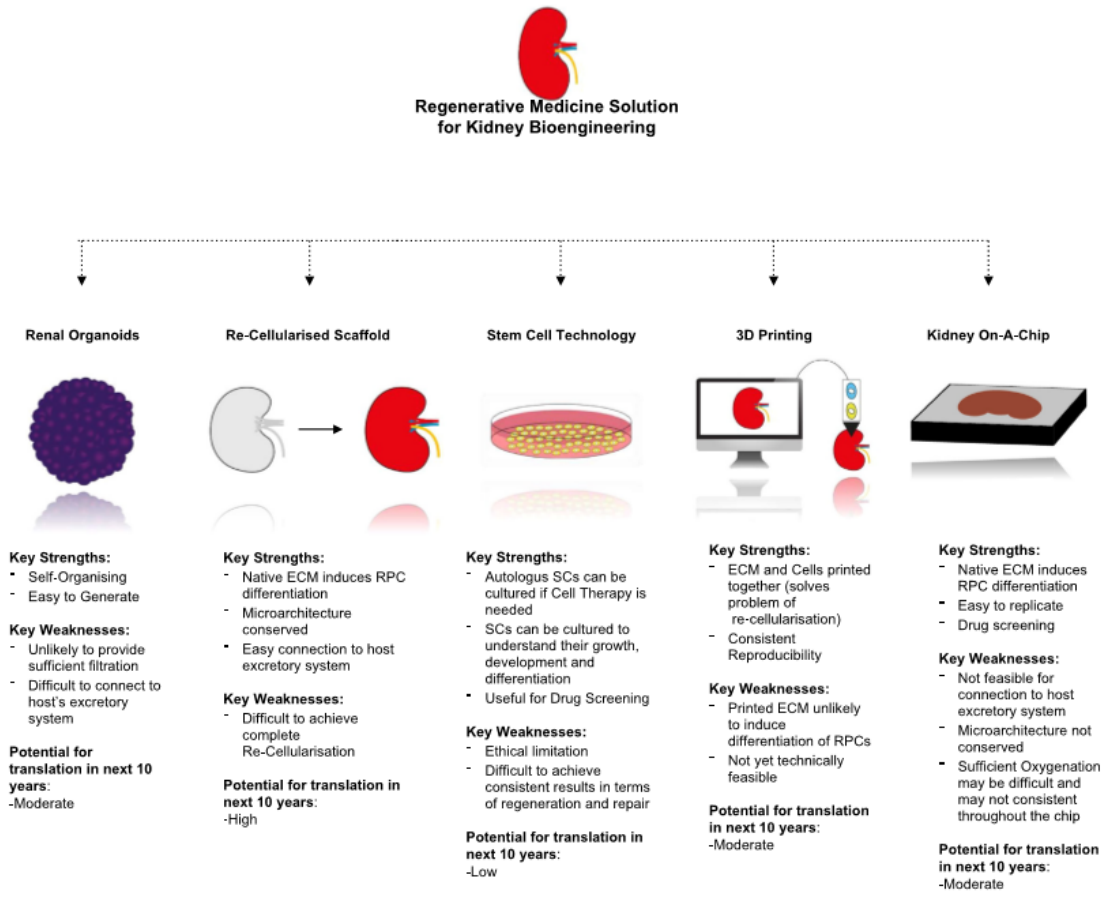

Figure 2. *Five regenerative medicine technologies applied for the treatment of kidney diseases. As it can be seen, all the technologies have weaknesses that hinder their potential. Mostly the weaknesses consider the ability of the constructs to mimick the ones in the human body, e.g., filtration, re-cellularization, microarchitecture and oxygenation, or technical development. However, re-cellularised scaffolds or cell-on-scaffold technology has the biggest potential for the fast translation. (Peloso et al., 2016).*

2. Three-dimensional bioprinting

2.1. *The basics*

Three-dimensional (3D) bioprinting, also known as 3D bioprinting, biofabrication, additive fabrication, rapid prototyping, and solid-free form technology, was first developed in the early 1990s (Francis & Bulletin, 2015; Sultan & Mathew, 2018). It was derived from 3D printing which was described in the 1980s by Charles Hull from the University of Colorado, under the name stereolithograpgy (Dai et al., 2019; Gao & Cui, 2016; Radenkovic, Soulouk, & Seifalian, 2016; Sultan & Mathew, 2018). In general, 3D bioprinting is a multidisciplinary technology that combines the knowledge from different discplines, including energy, engineering, biology, biotechnology, material, information, as well as medicine, and mainly focuses on the life sciences and medicine (Zhang et al., 2018; Dai et al., 2019). The major difference of 3D bioprinting compared to 3D printing are the utilized materials, which are mainly biomaterials, cells, and growth factors (Zhang et al., 2018). The current progress of 3D bioprinting is still at an early stage, and more research and understanding considering this field is needed before the industrial applications (Gao & Cui, 2016).

However, as a technology, 3D bioprinting has showed many advantages (Leppiniemi et al., 2017; Piras et al., 2017; Savage, 2016). When compared to the more conventional technologies, 3D bioprinters can build complex objects that were not possible earlier, e.g., internal contours where no tool could reach (Piras et al., 2017; Savage, 2016). In addition, 3D bioprinting offers lighter structures, better product performance, and lower production costs due to the missing of moulds and other manufacturing tools, high reproducibility, fine control of the process, and up-scalability (Leppiniemi et al., 2017; Piras et al., 2017). It also allows the distribution of different cell types, biochemical factors, proteins, and drugs at the desired locations, i.e., biomaterials and ECM components (Francis & Bulletin, 2015; Piras et al., 2017), which has typically been one of the major problems associated with populating scaffolds with cells (Dzobo et al., 2018). The revolutionary advantages of 3D

bioprinting are personalized products and mass customization (Leppiniemi et al., 2017; Sultan & Mathew, 2018).

Due to these many advantages, 3D bioprinting has gained a lot of attention in the biomedical applications in which it has a more and more important role (Zhang et al., 2018). 3D bioprinting has been used in customized models to allow preoperative surgigal planning of high risk operations, medical education, and guiding the construction of medical implants (Zhang et al., 2018; Radenkovic, Soulouk, & Seifalian, 2016). It has also been used in human permanent implants, biomimetic scaffolds, drug testing models, controlled drug releasing, surgigal cutting and drill guides, and tissue engineering and wound-healing applications (Zhang et al., 2018; Leppiniemi et al., 2017). Considering the scaffolds and implants, numerous applications of 3D bioprinting have been reported in literature from bone and cartilage scaffolds, skin and prevascularised tissues fabrication, cardiac constructs to neuronal tissue and muscle–tendon units (Piras et al., 2017; Radenkovic, Soulouk, & Seifalian, 2016; Vijayavenkataraman, et al., 2018). To mention a few, a bioresorbable tracheal splint was fabricated using 3D bioprinting and succesfully implanted in a child (Radenkovic, Soulouk, & Seifalian, 2016).

2.2. *Technologies*

The main technologies suitable for 3D bioprinting of biomaterials in regenerative medicine include inkjet (DBB), microextrusion (MBB), and laser-assisted bioprinting (LBB) (Dzobo et al., 2018; Li et al., 2016; Mandrycky et al., 2016; Murphy & Atala, 2014). Recently, also stereolithograpgy (SLA) bioprinting, traditionally used in the basic 3D printing, has been modified to fabricate cell-laden scaffolds (Lee et al., 2017; Neiman et al., 2015; Owen et al., 2016; Wang et al., 2015; Zhu et al., 2018). All these technologies have their distinct advantages, disadvantages, and limitations (Lou et al., 2014; Mandrycky et al., 2016). Thus, different features of these technologies should be considered in light of the most important factors in 3D bioprinting, such as surface resolution, cell viability, and the properties of the biomaterials used for the

3D bioprinting (Murphy & Atala, 2014). No single 3D bioprinting technology is able to produce all scales and complexities of the tissues (Mandrycky et al., 2016).

Inkjet bioprinters use thermal or acoustic forces to eject drops of liquid onto a substrate in 3D bioprinting (Dzobo et al., 2018; Murphy & Atala, 2014). Thermal inkjet bioprinters function by electrically heating the printhead to produce pulses of pressure that force droplets from the nozzle, whereas acoustic inkjet bioprinters use an acoustic radiation force associated with an ultrasound field to eject liquid droplets from an air-liquid interface (Dzobo et al., 2018; Murphy & Atala, 2014). Microextrusion bioprinting is a modification of DBB, in which uninterrupted cylindrical lines rather than a liquid bioink droplets are printed (Mandrycky et al., 2016). MBB uses an air-force pump, a mechanical screw, or a plunger (Dzobo et al., 2018; Mandrycky et al., 2016; Tappa & Jammalamadaka, 2018). In the laser-assisted bioprinting, a laser pulse vaporizes a portion of the donor layer, creating a high-pressure bubble at the interface of the bioink layer, which in turn moves the suspended bioink (Mandrycky et al., 2016; Murphy & Atala, 2014). In the end, the falling bioink droplet is collected on the receiving substrate and cross-linked (Mandrycky et al., 2016; Murphy & Atala, 2014). On the other hand, the SLA bioprinting polymerizes light-sensitive polymer materials layer-by-layer by the light, additively building up 3D structures, using digital micromirror arrays which control the light intensity of the printing area (Lim et al., 2018; Wang et al., 2015; Wang et al., 2018). The schematic representation of the current main bioprinting technologies can be seen in the Figure 3 below.

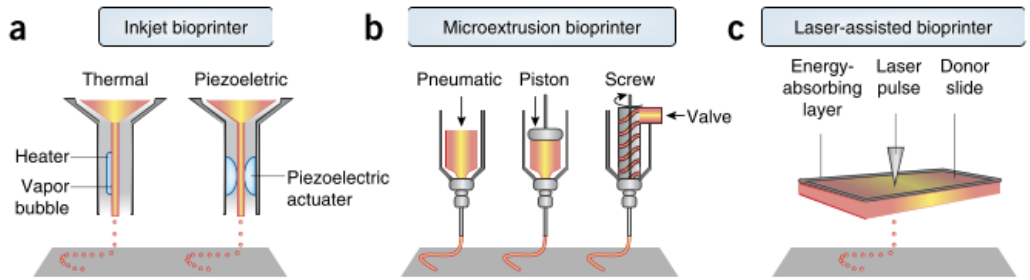

Figure 3. *The different 3D bioprinting technologies. DBB is based on thermal or acoustic operation and MBB on the air-force pump, mechanical screw, or plunger, whereas LBB is based on the laser pulse. (Mandrycky et al., 2016; Murphy & Atala, 2014).* **A.** *Inkjet bioprinting.* **B.** *Microextrusion bioprinting.* **C.** *Laser-assisted bioprinting. (Murphy & Atala, 2014).*

Each current 3D bioprinting technology requires bioinks with the specific rheological properties and has a different effect on the cell viability. Microextrusion bioprinting supports a wide range of viscosities, ranging between 30 mPa·s and $6*10^7$ mPa·s (Axpe & Oyen, 2016; Mandrycky et al., 2016; Murphy & Atala, 2014; Ozbolat et al., 2017). Nevertheless, the cell density within the bioinks can be very high, and the shear stress during the extrusion process decreases the cell viability, resulting in the cell viability of 80% - 90% (Axpe & Oyen, 2016). Thus, MBB has the lowest cell viability. In inkjet-based bioprinting, the viscosity level is supported between 3.5 mPa·s and 12 mPa·s, which depends on the bioink concentration (Mandrycky et al., 2016; Ozbolat et al., 2017). In general, bioinks in DBB are less viscous (<10 mPa·s), have lower cell densities (<16*106 cells/mL) compared to microextrusion, and offers cell viabilities of around 90% (Axpe & Oyen, 2016). On the other hand, the viscosity for laser-assisted bioprinting ranges between 1 and 300 mPa·s (Axpe & Oyen, 2016; Mandrycky et al., 2016; Murphy & Atala, 2014; Ozbolat, 2017). In addition, the medium cell densities in LBB are around 108 cells/mL and the cell viability is the highest from the methods, (>95%) (Axpe & Oyen, 2016). The overall differences between these three major 3D bioprinting technologies are listed in short in the Table 1 below.

Table 1. *The differences between the major 3D bioprinting technologies. (Adapted from Mandrycky et al. (2016) and Murphy & Atala (2014)).*

Parameters	Inkjet (DBB)	Microextrusion (MBB)	Laser assisted (LBB)
Supported viscosities	3.5 - 12 mPa·s	39 mPa·s to >$6*10^7$ mPa·s	1 - 300 mPa·s
Print speed	Fast (1 - 10.000 droplets per second)	Slow (10 - 50 µm/s)	From medium to fast (200 - 1.600 mm/s)
Resolution	High	Moderate	High
Quality of vertical structure	Poor	Good	Fair
Gelation methods	Chemical and photo-cross-linking	Chemical and photo-cross-linking, shear thinning, and temperature	Chemical and photo-cross-linking
Cell densities	Low, <10^6 cells/ml	High (cell spheroids)	Medium, 10^8 cells/ml
Cell viability	>85%	40-80%	>95%
Printer cost	Low	Moderate	High

Based on the earlier descriptions and the Table 1, each of the 3D bioprinting technologies has their advantages and limitations. With MBB, highly viscous bioinks, such as cellular spheroids, complex polymers, and almost all types of hydrogel pre-

polymer solutions with high cell densities for tissue formation, can be printed (Bishop et al., 2017; Dzobo et al., 2018; Mandrycky et al., 2016). This is also the case with the laser-assisted bioprinting, in which the nozzle-free technology does not cause mechanical stress on the cells or clogging of the nozzle (Mandrycky et al., 2016; Murphy & Atala, 2014). This results in, e.g., the possibility to use a broader range of the biomaterials in 3D bioprinting (Mandrycky et al., 2016). The bioinks with the lowest viscosity and the narrowest viscosity range can be used in the case of the inkjet bioprinting. This is due to the excessive force required to eject drops with solutions of higher viscosities and the requirement of the biomaterials to be in a liquid form (Murphy & Atala, 2014). To maintain biological materials in the liquid form, also the number of cells within the bioink is lowered (Dzobo et al., 2018). Furthermore, clogging can occur in the DBB (Mandrycky et al., 2016), which is increased with the high cell concentrations (Dzobo et al., 2018).

In addition to the viscosity range, the easiness of operation and handling of the cells is another difference between these technologies. According to the Table 1, DBB and LBB have a higher printing speed and resolution when compared to the MBB, enhancing the operation easiness, but microextrusion printing have more cross-linking methods. When it comes to the cells, MBB and LBB can be used to achieve cell densities similar to those found under physiological conditions (Dzobo et al., 2018), with minimum effect on cellular viability and function in the case of LBB due to the lack of directly applied force to the cells (Dzobo et al., 2018; Wang et al., 2015). In the case of MBB, the high extrusion pressures result in the distortion of cellular structure and loss of cellular viability (Bishop et al., 2017), which can also be seen from the Table 1. Nevertheless, the disadvantages of the LBB are the possible side effects of the laser exposure on the cells and an inaccurate targeting and positioning of these cells (Mandrycky et al., 2016), together with the metallic residues in the bioprinted materials (Dzobo et al., 2018). On the other hand, the advantage of the inkjet bioprinting is the possibility to produce droplets with uniform cellular density and the potential to introduce concentration gradients of cells, materials, or growth factors by altering the drop densities or sizes (Murphy & Atala, 2014).

The cost and availability have their own effect on the use of the 3D bioprinting technologies. Inkjet and microextrusion bioprinting are both low cost and common technologies, from which the DBB is the first bioprinting technology and a modified version of the 2D ink-printing (Mandrycky et al., 2016; Murphy & Atala, 2014). Thus, the availability of 2D printers in the research laboratories make it possible to widely use this 3D bioprinting technology (Murphy & Atala, 2014). On the other hand, laser-assisted bioprinters have a high cost, a complex control of the laser printing system, and they are rather rare (Mandrycky et al., 2016; Wang et al., 2015).

Interestingly, the high resolution down to 200 µm, high speed, and cell viability higher than 90%, due to the nozzle-free technology, makes the stereolithograhy-based bioprinting a competitive technology when compared to the other presented technologies, especially in comparison to DBB and MBB (Wang et al., 2015; Wang et al., 2018). Most importantly, SLA allows high spatial resolution, which helps to better mimick the complex architecture and microenvironment of the tissues and organs (Lim et al., 2018). Further, SLA considerably reduces the printing time when compared to the other bioprinting technologies (Wang et al., 2015).

However, SLA is not yet fully customized for 3D bioprinting (Wang et al., 2015), which can be harmful for the bioprinted cells, and the UV light and near-UV blue light (405 nm) mostly utilized in this technology damage the cell DNA, are toxic to mammalian cells, and disrupt the cellular processes (Wang et al., 2015; Wang et al., 2018). Visible-light-sensitive photoinitiators and polymerization are thus recommended (Wang et al., 2018). Therefore, many obstacles must be overcome for the SLA bioprinting to become fully compatible in 3D bioprinting of the cells and biological materials. As mentioned before, a single bioprinter cannot alone to make all the complexities of the tissues, and the proper 3D bioprinting technology needs to be selected according to many factors, such as the cell viability and the properties of the biomaterials.

2.3. *Components and operation*

Commercial 3D bioprinters are available, e.g. from Cellink® and regenHU. In general, as also explained in the Subchapter 2.2, the available printers include cheaper inkjet bioprinters with a small droplet size and viscosity, more expensive but slower microextrusion bioprinters with continuous release of material, and finally the most expensive laser-assisted bioprinters with the highest viscosity, resolution, and cell viability (Axpe & Oyen, 2016; Radenkovic, Soulouk, & Seifalian, 2016). The most existing commercial bioprinters, such as the Bioplotter and NovoGen 3D Bioprinting platform, are based on the extrusion technology (Murphy & Atala, 2014).

However, lately the term customizable which means manufacturing of the consumer-specific products, have became more and more important also in the case of the 3D bioprinters (Mandrycky et al., 2016; Murphy & Atala, 2014). These tailored and thus consumer-specific 3D bioprinters are meant to decrease the possible high prices associated to 3D bioprinters, especially with the laser-assisted ones, to better meet the needs of the consumers and to enhance the 3D bioprinting performance (Campbell et al., 2015; Fitzsimmons et al., 2018).

Due to this trend, researchers worldwide have started to develop different types of 3D bioprinters with slight variations and performance (Campbell et al., 2015; Fitzsimmons et al., 2018). In addition, Mandrycky et al. (2016) reported a few investigations and their attempts to enhance inkjet- and laser-assisted bioprinters. Thus, the amount and placement of the components of the 3D bioprinters seem to vary depending on the manufacturer, the 3D bioprinting technology, and the target application. In this thesis, BioX 3D bioprinter from Cellink® was utilized. The technology used in this biopinter is microextrusion with the pneumatic print heads. The components and the structure of the BioX 3D bioprinter and an example of ongoing bioprinting process can be seen in the Figure 4.

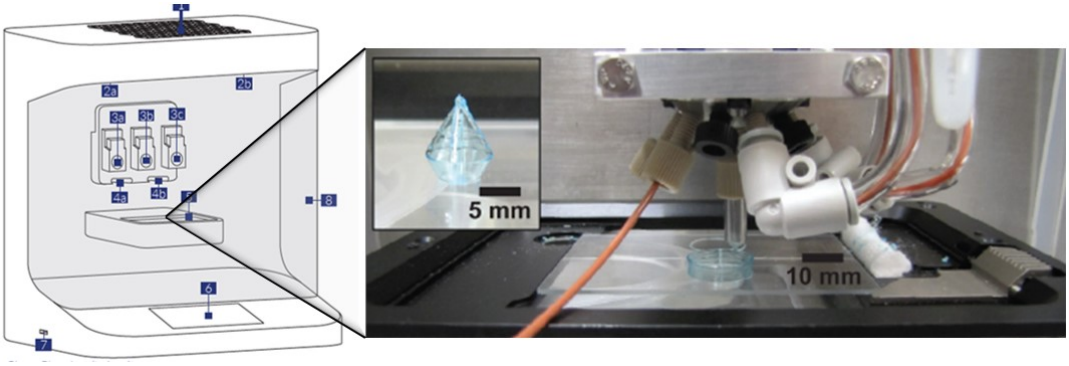

Figure 4. *The different components of the BioX 3D Bioprinter from Cellink® and the operation of the 3D bioprinter. 3D bioprinting can be utilized in manufacturing structures in the micrometer scale with high precision and orientation through layer-by-layer deposition (Zhang et al., 2018).* **1.** *Clean chamber (tm) unit.* **2a.** *UV sterilization LED 1.* **2b.** *UV sterilization LED 2.* **3a.** *Printhead mount 1.* **3b.** *Printhead mount 2.* **3c.** *Printhead mount 3.* **4a.** *Photo curing module mount 1.* **4b.** *Photo curing module mount 2.* **5.** *Printbead.* **6.** *7'' touch screen.* **7.** *USB port.* **8.** *Protective door. (Adapted from BIO X 3D Bioprinter User Manual (2017) and Campbell et al. (2015)).*

In the case of 3D bioprinting as the manufacturing process, the operation of the 3D bioprinter is divided into six different steps. These steps are; imaging of the desired tissue or organ, designing of the 3D model, material selection for the bioink, cell type selection, bioprinting process itself, and the end-use selection for the 3D bioprinted hydrogel (Murphy & Atala, 2014). The different steps are presented in a nutshell in the Figure 5 below, followed by the detail descriptions.

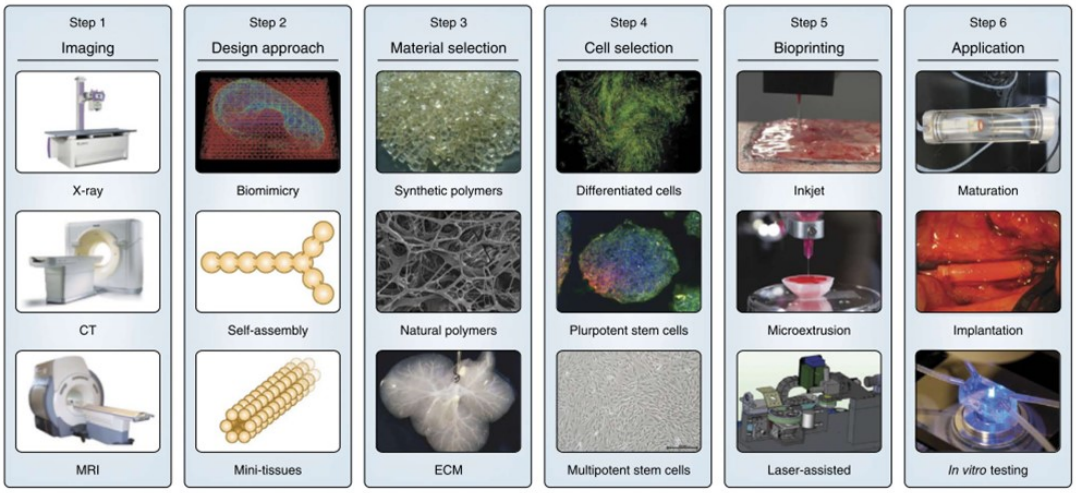

Figure 5. *The steps of 3D bioprinting process. (Murphy & Atala, 2014).*

Computed tomography (CT) and magnetic resonance imaging (MRI) are noninvasive imaging models which are used to provide information on 3D structure and function

at the cellular, tissue, organ, and organism level (Dzobo et al., 2018; Murphy & Atala, 2014). CT images are based on the slices of the tissue or organ architecture, revealing the true volume of these tissues or organs, whereas MRI functions by the nuclear magnetic resonance, showing a powerful contrast resolution in the tissue or organ images (Dzobo et al., 2018). Further, computer-aided design and computer-aided manufacturing (CAD-CAM) tools and software with the mathematical modelling techniques are used to convert this obtained structural and functional data into 3D models (Dzobo et al., 2018), which is also called the design process. This design process in 3D bioprinting is based on three central design strategies, which are biomimicry, autonomous self-assembly, and mini-tissue building blocks (Atala & Murphy, 2015; Murphy & Atala, 2014; Li et al., 2018).

In more detail, biomimicry involves the manufacture of the identical reproductions of the cellular and extracellular components of a tissue or an organ, whereas autonomous self-assembly utilizes the early cellular components, embryonic or stem cells, in producing their own ECM components, appropriate cell signaling, autonomous organization, and patterning to yield a certain biological microarchitecture and function of a tissue or an organ. On the other hand, the concept of mini-tissues is a combination of the earlier methods and is divided into two main strategies. First, self-assembling cell spheres are assembled into a macro-tissue using biologically inspired design and organization. Second, accurate, high-resolution reproductions of a tissue unit are designed and allowed to self-assemble into a functional macro-tissue. In the end, all these strategies are required to print a complex 3D biological structure with multiple functional, structural, and mechanical components and properties. (Murphy & Atala, 2014).

In the end, these created 3D models, utilizing the design strategies described earlier, are exported to the 3D bioprinter in the form of, e.g., .stl files (Li et al., 2018). .Stl (strereolithograpgy) and .vrml (virtual reality modeling language) file formats are the most used ones (Tappa & Jammalamadaka, 2018), however, .obj file format have also lately been gaining popularity due to its ability to add colors and texture information on the manufactured 3D models. Nowadays, a variety of different CAD or CAD-CAM

softwares exists, from free to paid ones. SolidWorks, AutoCAD, and ZBrush are some examples of popular CAD software used commercially in industries, whereas the freeware for making 3D models include Blender, FreeCAD, Meshmixer, OpenSCAD, and SketchUp (Tappa & Jammalamadaka, 2018). After all these steps, the 3D bioprinting process itself is started. This process is explained in more detail in the Chapter 9.

2.4. *Materials in 3D bioprinting*

The basic raw material of 3D bioprinting is called bioink (Ozbolat et al., 2017). In general, bioinks can be cell-suspensions, cell-hydrogel mixtures, or biocompatible materials, from which the cell-hydrogel mixtures and biocompatible materials are the latest approaches (Li et al., 2018). Therefore, in 3D bioprinting, these bioinks are composed of various biopolymers with properties matching the sufficient operation of 3D bioprinter, together with the cell support and growth (Axpe & Oyen, 2016). Important features of an ideal bioink material include, e.g., bioprintability, high mechanical integrity and stability, insolubility in cell culture medium, biodegradability at an appropriate rate, non-toxicity and non-immunogenicity, and the ability to promote cell adhesion (Ozbolat et al., 2017).

Bioink materials should also be easily manufactured and processed, affordable, and commercially available, and bioprinted constructs composed of bioinks are expected to keep their designed shape, structural strength and integrity, easily engraft with the host, and degrade over time *in vivo* (Ozbolat et al., 2017). Currently, there are commercially available bioinks that offer reproducible results, such as Gel4Cell®, CellInk®, BioInk®, OsteoInk®, Bio127®, BioGel® (Tappa & Jammalamadaka, 2018), and GrowDex©. The main requirements for the bioinks and the bioink requirements in different bioprinting technologies are listed in the Figure 6 below.

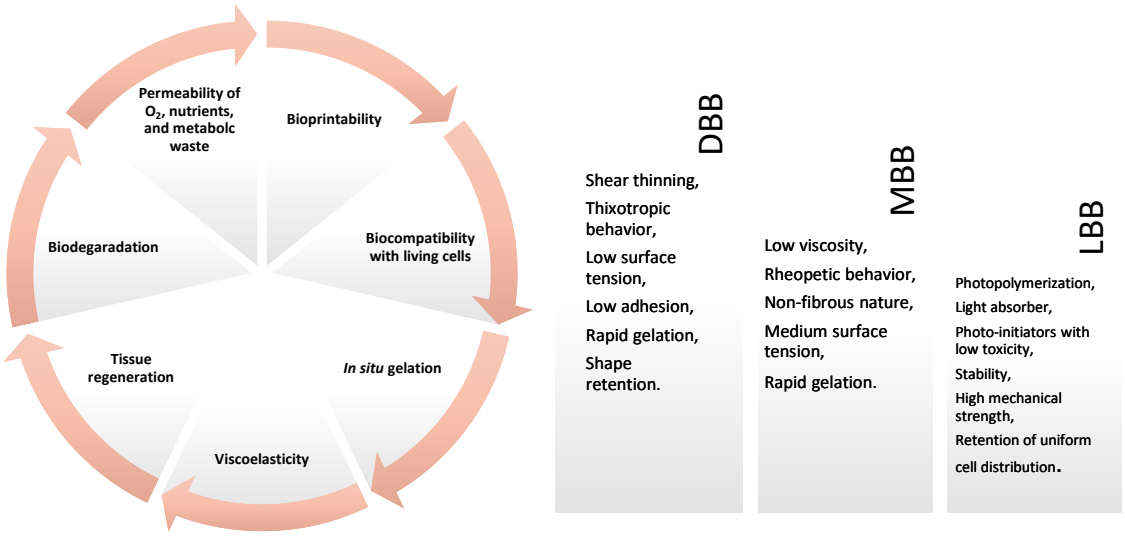

Figure 6. **A.** *The important requirements for the bioink selection for 3D bioprinting.* **B.** *The different bioprinting technologies and their bioink requirements. DBB stands for inkjet bioprinting, MBB mictroextrusion bioprinting, and LBB for laser-assisted bioprinting. (Adapted from Aarstad et al. (2017) and Ozbolat (2017)).*

In general, two major types of bioink materials have been utilized in the bioprinting processes of 3D tissue and organ constructs. These are scaffold-based and scaffold-free materials. Scaffold-based materials are the most common bioinks, and they include hydrogels, microcarriers, and decellularized matrix components, whereas scaffold-free bioink materials are basically cell aggregates. In scaffold-based bioinks, cells are loaded in exogenous materials, such as hydrogels, which is followed by bioprinting into 3D constructs. In scaffold-free bioinks, engineered neo-tissues that contain cells are deposited in specific patterns, which results in fusion and maturation of the cells into more complex tissues. (Ozbolat et al., 2017).

Recently, hydrogels have been extensively used as bioinks for the production of 3D bio-constructs (Park et al., 2017). Hydrogels are gel like, often cross-linked, capable of absorbing and retaining large quantities of water, biocompatible, highly permeable to oxygen, nutrients and other water-soluble compounds, show low cytotoxicity, and have tissue-like stiffness (Axpe & Oyen, 2016; Ozbolat et al., 2017; Markstedt et al., 2015; Park et al., 2017). Thus, hydrogels have structural and physicochemical similarities to ECM (Ozbolat et al., 2017; Park et al., 2017). The water content of the hydrogels is the most essential factor because biocompatibility of hydrogels and their

structural similarity to ECM is influenced by their inherent hydration levels (Ozbolat et al., 2017). In fact, hydrogels are mostly water by weight, but exhibit no flow in the steady-state due to the 3D cross-linked polymer network within the fluid, which gives them unique properties comparable to those of human tissues (Axpe & Oyen, 2016; Ozbolat et al., 2017).

Hydrogel must be viscous enough to retain its shape after printing and must have cross-linking abilities allowing for it to retain the 3D structure after bioprinting (Markstedt et al., 2015). Cross-linking can be achieved by, e.g., temperature change, UV photopolymerization, and ionic cross-linking (Markstedt et al., 2015). Therefore, in general, hydrogel cross-linking methods consist of non-covalent and covalent cross-linking methods, latter synthetized by chemical reactions or enzymatically catalyzed reactions (Ozbolat et al., 2017). Ionic cross-linking minimizes the risk of chemical contamination or chemical-induced toxicity, by involving noncovalent interactions formed when the ions of opposite charges electrostatically attract each other (Ozbolat et al., 2017). On the other hand, chemically cross-linked hydrogel is based on covalent bonding between polymer chains. Chemical cross-linking can provide better mechanical stability, but the use of a cross-linker could result in cytotoxicity. Photo-cross-linking is an example of the used chemical cross-linking methods (Ozbolat et al., 2017). Other interactions that may influence on the hydrogel formation include host-guest interactions, hydrogen bonds, van der Waals forces, hydrophobic interactions, and interlacking of the chains (Nascimento et al., 2018).

To mention a few bioink compositions, composite materials of alginate and CNF have shown promising results for 3D bioprinting and tissue engineering applications (Aarstad et al., 2017). This is based especially on the shear thinning properties of CNF combined with the viscous alginate that forms ionically cross-linked hydrogels with divalent cations at physiological conditions (Aarstad et al., 2017). Particularly, soft tissue cartilage-formation through 3D bioprinting, utilizing alginate-CNF composite hydrogels, have been a popular topic among researchers in the past few years (Nguyen et al., 2017; Markstedt et al., 2015; Sultan et al., 2017). This hydrogel composite maintains the pluripotency of the iPSCs, and is a suitable material for the

proliferation and growth of the cells (Nguyen et al., 2017). Alginate contributes with elastic properties and increases mechanical resistance at large deformations, whereas CNFs reduce the syneresis, the volume reduction upon gel formation, of the alginate gels and contributes to the increased resistance against compression at small deformations. This can be seen by an increase in Young's modulus or the rigidity of the gel. These results, for their part, make the combination of CNF and alginate a multifunctional and promising candidate for various bioink formulations.

Recently, lignin has been introduced into printing inks as a performance enhancer, to take an example, lignin-coated CNC in combination with methacrylate resin (MA) (Feng et al., 2017). The addition of lignin-coated CNCs increased the mechanical strength and thermal stability of the printed matrix (Feng et al., 2017). Elsewhere, increased lignin concentrations in PLA-lignin nanofibres alleviated undesirable inhibition of cell proliferation and provided antioxidant activity (Kai et al., 2016). Other possible uses of lignin could be incorporation into hydrogels to tune the hydrophilicity of the resulting matrix, and the development of lignin-based nanoparticles as nanocarriers for drug delivery. Therefore, in general, scalable lignin-based products obtained by applying 3D printing approaches would be promising in the future (Xu et al., 2018).

2.5. *Tissue and organ regeneration*

Tissue and organ diseases and loss are anticipated to exacerbate due to the aging population, making tissue and organ shortage a severe challenge worldwide (Francis & Bulletin, 2015). Already today, patients on various organ recipient waiting lists pass away before suitable donor organs become available (Francis & Bulletin, 2015). Thus, one of the most promising properties of tissue engineering and regenerative medicine is the possibility to make organ scaffolds that may reduce or eliminate the need for donor organs (Francis & Bulletin, 2015). One possible tool for this could be 3D printing and 3D bioprinting (Zhang et al., 2018; Francis & Bulletin, 2015), from which 3D bioprinting has been considered as one of the most advanced technologies in the field of tissue engineering and regenerative medicine (Sultan et al., 2017).

3D bioprinting has multiple good physical properties which enable its use in tissue engineering. 3D bioprinted scaffolds could mimic the characteristics and anatomical geometry of the desired tissues and organs, abolish the problems with manual cell seeding, and have a reproducible and standardized pore size, facilitating cell proliferation and aggregation. In addition, by combining biological and synthetic bioresorbable materials, 3D printed scaffolds could have enhanced load-bearing properties than original human tissues. (Radenkovic, Soulouk, & Seifalian, 2016).

Furthermore, 3D bioprinting technologies can be easily automated and integrated with imaging techniques to produce anatomically-correct structures, e.g. scaffolds, with customized size and shape for an individual patient (Axpe & Oyen, 2016; Leppiniemi et al., 2017; Lee & Dai, 2017). The uses of these 3D functional scaffolds and living tissues include degradation and remodeling studies, study of the cell-biomaterial interactions at the nanoscale level, drug testing or toxicological studies, and real transplantation in animals (Axpe & Oyen, 2016; Lee & Dai, 2017). In the Figure 7 below, these different uses of 3D bioprinted tissues are listed in more detail.

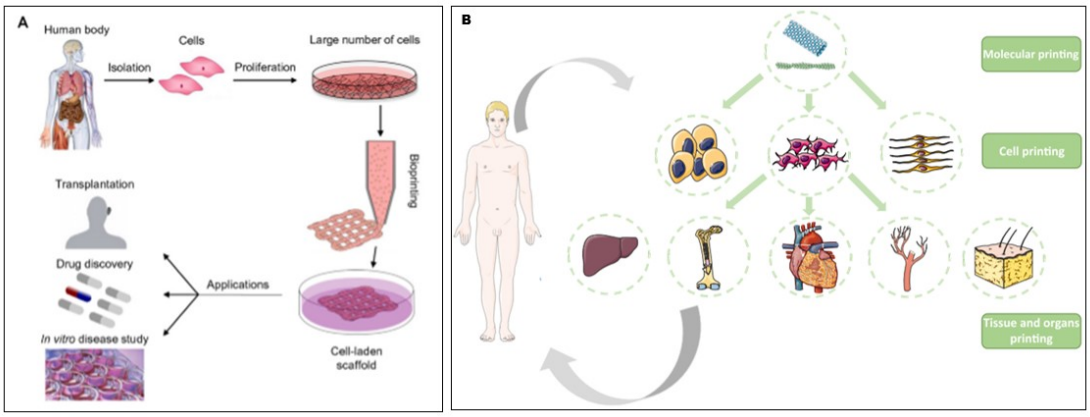

Figure 7. *Different uses of 3D bioprinted structures in regenerative medicine.* **A.** *As it can be seen, the extracted cells, for example stem cells, can be used, e.g., for in vitro disease study, drug discovery, and even transplantation. The extracted stem cells enable the production of patient-specific tissues and organs.* **B.** *3D bioprinting can be used in the multiple stages. It can be used to bioprint structures in the molecule size, certain cell types, and even tissues and organs. However, the size limits of bioprintable structures are dependent on the 3D bioprinter type, and the regeneration of the most complex organs still require more research. (Adapted from Li et al. (2016) and Mandrycky et al. (2016)).*

Thus, the studies of 3D bioprinting considering especially, e.g., toxicity screening, material possibilities for cell culturing and fabrication of tissues, is currently a popular

research area. Zhang et al. (2016) fabricated an endothelialized myocardium on-a-chip for toxicity screening, using the novel hybrid strategy based on 3D bioprinting, whereas Markstedt et al. (2015) printed human chondrocytes in the multiple shapes, e.g., in the shape of an human ear, with a bioink consisting of CNF and alginate. Elsewhere, Kesti et al. (2015) printed nose structures, using the bioink of gellan and alginate mixed with human micronized BioCartilage or hydroxyapatite (HA) particles. On their behalf, Keriquel et al. (2017) 3D bioprinted mesenchymal stromal cells with collagen and nano-HA for the bone regeneration. The Figure 8 below summarizes a few tissues and organ constructs, which have been produced through 3D bioprinting technology.

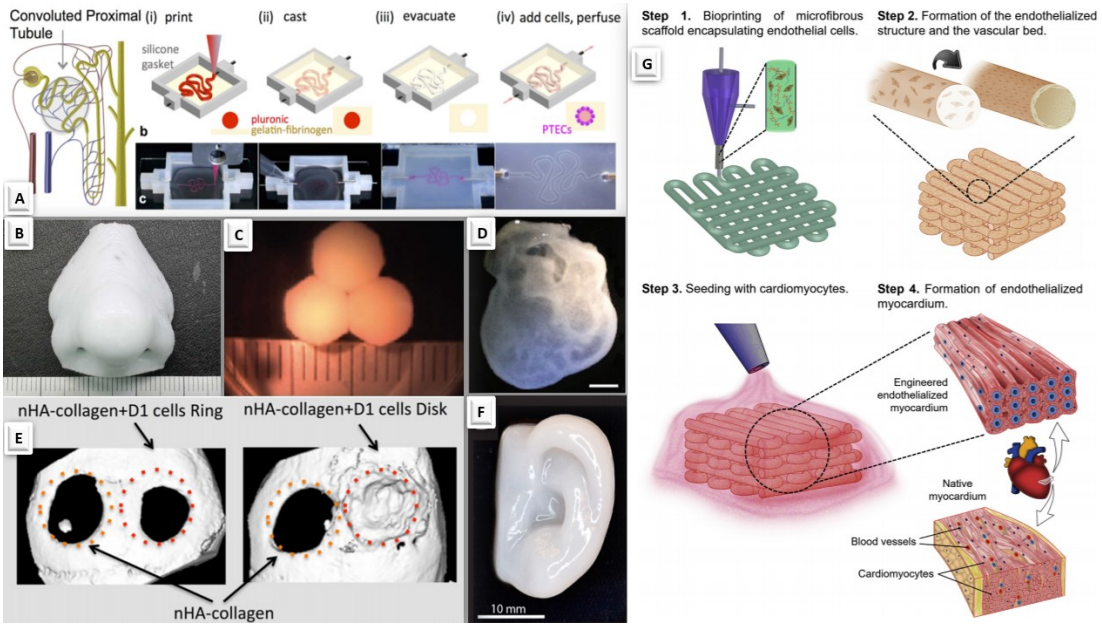

Figure 8. *Different tissue and organ constructs manufactured with 3D bioprinting.* **A.** *Schematics of a nephron and the different steps in the fabrication of 3D convoluted, perfusable proximal tubules, in which a fugitive ink was first printed on a gelatin-fibrinogen ECM (Homan et al., 2016).* **B.** *Gartilaginous nose grafts with the size of the adult nose (Kesti et al., 2015).* **C.** *Bioprinted liver tissue organoids mimicking the hepatic lobules of native liver tissues with tissue-like cellular density and tight intercellular junctions. Human primary hepatocytes, endothelial cells, and hepatic stellate cells were used. (Zhang et al., 2017).* **D.** *3D bioprinted heart with an internal structure (Zhang et al., 2017).* **E.** *NHA-collagen and D1 cells bioprinted in a ring or disk geometry in the bone regeneration (Keriquel et al., 2017).* **F.** *3D bioprinted ear-shaped cartilage (Markstedt et al., 2015). Ear-shaped cartilage could be the first bio-printed tissue in the clinical use (Savage, 2016).* **G.** *Endothelialized myocardium on-a-chip (Zhang et al., 2016).*

As it can be seen also from the Figure 8, 3D bioprinting's ultimate medical application would be in a 3D bioprinting of human organs (Radenkovic, Soulouk, & Seifalian, 2016). However, it is a long way to fabricate this kind of a live organ (Zhang et al., 2018). Nevertheless, there already are a few studies attempting to 3D bioprint smaller parts of the solid organs, their general shapes without inner cell constructs, or 3D constructs containing only few interacting cell types of the specific organ (Figliuzzi et al., 2017; Zhang et al., 2017; Zhong et al., 2016; Wu et al., 2018) These studies are focused especially on the heart and liver (Zhang et al., 2017; Zhong et al., 2016; Wu et al., 2018). An extremely small number of researches considering kidneys can be found, which makes it an important research area for the future. These few researches available are studying, e.g., the decellularization of the kidneys for kidney regeneration, self-assembling of the tissue spheroids to fabricate a kidney mini-tissue, or the utilization of the silicon droplets as physical analogues of tissue spheroids in making the kidney arterial vascular tree (Homan et al., 2016; Figliuzzi et al., 2017; Vijayavenkataraman et al., 2017; Unbekandt & Davies, 2010).

Furthermore, a 3D bioprinting company Organovo has published many studies during 2015 - 2017 describing attempts to bioprint kidney structures that mimick as much as possible the structure of the native human kidney. Organovo has printed, e.g., 3D consoluted renal proximal tubules on perfusable chips, microscopic veins that make up a kidney, mini kidneys, and the base of a human kidney for drug-testing (Jackson, 2016; Jackson, 2017; Jackson, 2018). In general, multiple challenges exist before the whole and functional kidneys can be bioprinted. These challenges include the architectural complexity of kidney, limited availability of primary cells, the formation of nephrons equivalent to that of the native kidney, and the formulation of a bioink that will resemble the complex renal structure and functionality. Bioprinting of tissue spheroids is one potential approach to overcome these challenges. (Vijayavenkataraman et al., 2017).

3. Biopolymers for 3D bioprinting

3.1. *Biopolymers in general*

As we can see from the Figure 9, many materials have been used for the fabrication of bioinks in 3D bioprinting, from synthetic materials to the bio-based ones. Synthetic materials include for example poly(ethylene glycol) (PEG) and Pluronic, together with polycaprolactone (PCL) and poly(l-lactide-co-glycolide) (PLGA) (Gopinathan & Noh, 2018; Ullah et al., 2018). On the other hand, biomaterials are composed of polysaccharides, such as starch, cellulose, chitin, chitosan, and alginate and polysaccharides synthetized from bacterial, fungal, and animal proteins, such as collagen, gelatin, silk, and fibroin (Gunathilake et al., 2017; Kapoor & Kundu, 2016). The advantages of biomaterials are their biocompatibility, biodegradability, non-toxicity, similarity to ECM of the human body, and thus, good acceptance by biological systems, whereas synthetic materials are excellent when it comes to the mechanical properties and customization (Gunathilake et al., 2017; Mogoşanu & Grumezescu, 2014; Naseri-nosar & Maria, 2018). Thus, biomaterials are often reinforced with the synthetic ones (Chinga-Carrasco, 2018). The Figure 9 below reveals the biomaterial distributions of the few common synthetic and bio-based materials in the current bioinks.

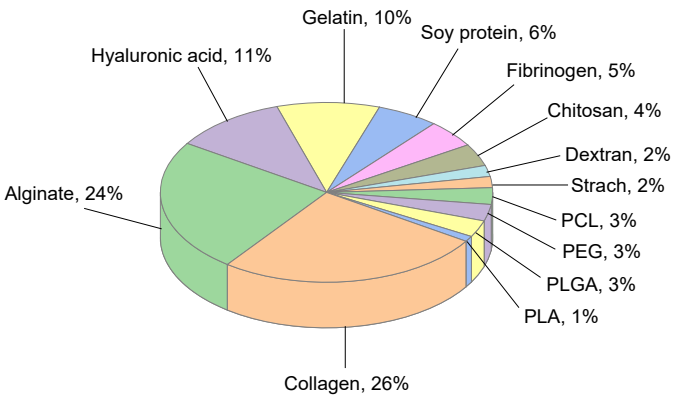

Figure 9. *Synthetic polymer and biopolymer distributions in the used bioinks*

(Adapted from Ullah et al. (2018)).

According to the Figure 9 and recently published articles, the most used biomaterials in 3D bioprinting and regenerative medicine are alginate, hyaluronic acid (HA), collagen, and gelatin (Ullah et al., 2018). CNF and CNCs have become more popular in the recent years due to their good properties in combination with other biomaterials, such as biocompatibility, high strength, high surface area, tuneable surface chemistry, non-cytotoxicity against a series of cell lines, and the lack of disease transmittance due to the plant-based origin (Dai et al., 2019; Xu et al., 2018). On the other hand, only rare biomaterial options include lignin (Larrañeta et al., 2018), silk fibroin (Park et al., 2013), and gellan gum (Yu, Kaonis, & Chen, 2017).

Among these biomaterials, alginate is the most common material in the current bioinks (Axpe & Oyen, 2016). It is Isolated from the cell walls of brown algae, having a structure of a linear polysaccharide, composed of (1–4)-linked β-D-mannuronic and α-L-guluronic acids (Axpe & Oyen, 2016; Markstedt et al., 2015). As a material, alginate supports cell growth, exhibits high biocompatibility, is non-immunogenic, low-cost, and forms hydrogels under mild conditions (Axpe & Oyen, 2016). The applications of alginate include cell encapsulation and cell cultures of, e.g. organoids and embryos (Ozbolat et al., 2017).

When taking an example from the recent materials, CNF is a plant-derived biomaterial, composed of aligned b-D-(1/4)-glucopyranose polysaccharide chains and extracted by mechanical, e.g., grinding, and chemical treatments, e.g., TEMPO-mediated oxidation (Lou et al., 2014; Piras et al., 2017; Sultan et al., 2017). CNF is non-cytotoxic, flexible, has highly entangled networks, a high viscosity, shear-thinning properties, good properties already at concentrations lower than 1 wt%, and hydrogel forming properties (Piras et al., 2017; Xu et al., 2018). As a material, CNF can be used as rheological modifiers, potential carriers for functional components, and components in hydrogels (Leppiniemi et al., 2017; Sultan et al., 2017). CNF could also be an appropriate option for modeling of 3D tumors and therefore, an important material in the cancer research (Chinga-Carrasco, 2018). In the Table 2, a few studies considering CNF-based applications have been summarized.

Table 2. *The latest and interesting material, bioink, and 3D bioprinting studies considering CNF and MCF.*

Materials	Pre-treatments	wt%	Cross-linking method	Rheology	Printability	References
CNF	CNF: TEMPO-mediated and periodate oxidation	CNF: 0.2	$CaCl_2$ before bioprinting	The viscosity of the nanocellulose was reduced	-	Rees et al. 2014
CNF Alginate	CNF: TEMPO-oxidation	CNF: 2.00 Alginate: 0.50	$CaCl_2$ before bioprinting	The G′ and G″ increased for higher proportions of CNF	High shape fidelity and printing resolution	Markstedt et al. 2015
CNF Alginate	CNF: mechanical refinement and enzymatic treatment	CNF: 2.4 Alginate: 0.6	H_2O_2 after bioprinting for 5 minutes	-	Good grid line thickness and homogeneity	Nguyen et al. 2017
CNF Na-alginate (SA)	CNF: TEMPO-oxidation	CNF: 1.0 SA: 4.0 CNF/SA: 90/10	$CaCl_2$ before bioprinting	The bioinks exhibited a yield flow behavior	Excellent printability and dimensional stability at room temperature	Leppiniemi et al. 2017
MCNF and CMCNF Na-alginate	MCNF: morpholine pre-treatment CMCNF: morpholine pre-treatment and carboxymethylation	CNF: 1 SA solution: 2	$CaCl_2$	The addition of 5 wt% MCNF: 27% increase in G′ The addition of 5 wt% CMCNF: 10% increase in G′	-	Onyianta et al. 2018
CNF Xylan-tyramine	CNF: enzymatic pretreatment	CNF: 2.7 Xylan: 10.6	HRP-enzyme and H_2O_2 after bioprinting	All the bioinks had a suitable viscosity for bioprinting	Could be deformed without breaking, and kept their shape when handled and after cross-linking	Markstedt et al. 2017
Microfibrillated cellulose (MCF) Lignosulfonate (LS)	MCF: mechanoenzymatic hydrolysis	CNF: 2 LS: 0-50	-	The viscosity increased with the increased LS concentrations	The object geometry was maintained	Shao et al. 2015

On the other hand, another recently popular material, CNCs, can be obtained from cotton and wood, which yield a narrow distribution of highly crystalline nanorod, and tunicin, bacteria, and algae, which generate crystals with larger polydispersity and dimensions, through the removal of amorphous sections of purified cellulose utilizing acid hydrolysis (Klemm et al., 2011; Piras et al., 2017; Sultan et al., 2017). The obtained CNCs are highly crystalline, rod-like particles with the width of 5 - 70 nm and length between 100 nm and several micrometers (Klemm et al., 2011). CNCs are

anisotropic particles with limited flexibility, high aspect ratio, and outstanding mechanical properties (Klemm et al., 2011; Siqueira et al., 2017). They have been used as a reinforcement in alginate-based composites and as one of the components in 3D printable inks (Leppiniemi et al., 2017).

As a new material source, utilization of industrial lignin is constantly becoming more important (Lievonen et al., 2016; Lintinen et al., 2018; Ashok et al., 2018). Lignin is the complex, hydrophobic biopolymer built of phenylpropanoid units, and it is a main by-product from pulping and biorefineries (Lintinen et al., 2018; Munk et al., 2015). Lignin owns many useful features for the purposes of regenerative medicine (Xu et al., 2018). It is abundant, low-cost, and considered biocompatible, biodegradable, and CO_2 neutral material (Figueiredo et al., 2018; Liu et al., 2019), with good rheological charasteristics, good viscoelastic properties, and film-forming capacity (Figueiredo et al., 2018). It can enhance the cell adhesion in scaffolds, possess high stability, possibly abating the scaffold degradation rates, and has antimicrobial, antifungal, and antioxidant properties (Figueiredo et al., 2018; Quraishi et al., 2015). Primarily, lignin adds strength and rigidity to the cell walls, allows the transport of water and solutes, provides physical barrier against invasion by phytopathogens, and prevents the degradation of the structural polysaccharides in the cell wall (Figueiredo et al., 2018; Lievonen et al., 2016).

The major disadvantages of this material are the possible cytotoxicity for some cell types at high dozes due to the phenolic nature of lignin (Quraishi et al., 2015), the imprecisely defined structure depending on the origin of lignin (Lievonen et al., 2016), together with the infusibility and insolubility of lignin in common solvents (Lievonen et al., 201; Liu et al., 2019). This insolubility has been one factor in hindering the exploration of lignin and lignocellulosic biomass as bioinks for 3D bioprinting (Liu et al., 2019). Other application areas of lignin include drug encapsulation and release (Dai et al., 2018; Figueiredo et al., 2017; Witzler et al., 2018), which has been a popular research area in the recent years, scaffolds (Farhat et al., 2017; Witzler et al., 2018), bioactive coatings for implants (Erakovic et al., 2014; Witzler et al., 2018), and utilization of the antibacterial properties of lignin (Witzler et al., 2018).

Recently, nano- and microscale lignin particles have arisen as promising alternatives to regular lignin (Nypelö, Carrillo, & Rojas, 2015; Sipponen et al., 2017), due to their enhanced properties. Most importantly, the preparation of CLPs through the aqueous lignin nanoparticle dispersions overcomes the problems of poor solubility and miscibility of regular lignin (Lievonen et al., 2016). CLPs can be produced from lignin, e.g., using a straightforward and green production process introduced by Lievonen et al. (2016), resulting in CLPs with the desired spherical particle morphology and colloidal stability (Lievonen et al., 2016). In this process, regular lignin is first dissolved into tetrahydrofuran (THF), which is followed by the filtration of the solution, and dialysis using periodically replaced deionized water (Lievonen et al., 2016). CLPs are formed during the dialysis in minimum 24 hours (Lievonen et al., 2016).

Many process variations considering the CLP production naturally exist due to the urge to establish processes suitable also for the low-cost, efficient, green, and large-scale industrial use. Lignin nanoparticles have been synthesized by thermomechanical treatments, acid and solvent-antisolvent precipitation, emulsification and microemulsification (Nypelö, Carrillo, & Rojas, 2015), as well as CO_2 saturation, continuous solvent exchange, dialysis, and sonication (Richter et al., 2016). Nevertheless, most of the published processes are energy intensive, consume considerable number of reagents, involve the use of hazardous chemicals, or produce too diluted products not suitable for the large-scale production (Ashok et al., 2018). Other drawbacks include the lack of particle integrity and control of size and size distribution (Nypelö, Carrillo, & Rojas, 2015). The latest and most promising up-scaled CLP production methods include the processes of Leskinen et al. (2017) and Lintinen et al. (2018). The process of Leskinen et al. (2017) includes the steps of recovery of the utilized solvent by evaporation, drying of formed CLPs into solid form, and re-dispersing them into an aqueous dispersion (Leskinen et al., 2017), whereas Lintinen et al. (2018) introduce a closed cycle process for the large-scale production of CLPs at low cost. Further, Ashok et al. (2018) have compiled a techno-economic assessment of a large-scale continuous flow process for producing commercially

significant amounts of dry colloidal lignin, based on the previously introduced process developed by Lintinen et al. (2018).

In general, CLPs are interesting components for many biomaterial applications due to their smooth surface structure and stability in physiological conditions (Mattinen et al., 2018). CLPs have been commercially used in, i.e., additives, binders, dispersants, and surfactants (Lievonen et al., 2016). Furthermore, they hold a great potential in bio-based adhesives, crop additives, stabilizers, antimicrobial materials, and wound healing applications (Lievonen et al., 2016), together with nanocomposites (Lievonen et al., 2016; Ashok et al., 2018), controlled drug delivery (Lievonen et al., 2016; Ashok et al., 2018), and functional surface coatings (Ashok et al., 2018). Particularly colloidal cationic lignin particles have been reported to be excellent in stabilizing pickering emulsions (Sipponen et al., 2017). Above all, a new promising application area of CLPs is a component in 3D printable bioinks and hydrogels, as described in more detail in this Master's thesis. Nevertheless, other researches considering the utilization of CLPs as a component in 3D printable bioinks are not yet available.

In the case of the rarely used biomaterials, silk fibroin is a natural fibrous protein originating from silk, spun by silkoworms or insects (Gopinathan & Noh, 2018; Kapoor & Kundu, 2016; Park et al., 2013). The pure fibroin component can be obtained by removing sericin using various degumming conditions (Kapoor & Kundu, 2016; Park et al., 2013). The properties of silk fibroin are biocompatibility, oxygen and water permeability, biodegradability, minimal inflammatory response, and an ability to form hydrogels directly through self-assembly of protein chains into physically cross-linked β-sheet crystals with the rate of sol-gel transition, dependent on protein concentration, temperature, metal ions, and pH (Park et al., 2013; Ming et al., 2016). The applications of silk fibroin are films, sponges, mats, gels, scaffolds, and tubes (Kapoor & Kundu, 2016). For example, Zheng et al. (2018) prepared free-standing silk-PEG bioink with excellent printability, high resolution, and supported mesenchymal stem cell viability for a longer period. In the Table 3, other common biomaterials used in 3D bioprinting together with their characteristics have been listed.

Table 3. *Characteristics of a few common and rare biomaterials used in bioinks for 3D bioprinting.*

Material	Structure	Features	Applications
Agarose	Linear marine polysaccharide, extracted from seaweed, with an agarobiose repeating unit (Gopinathan & Noh, 2018).	Excellent gel formation properties, thermoreversible gelation, biocompatibility, good mechanical properties, limited ability to support cell growth, and resembalance to ECM (Gopinathan & Noh, 2018; Zarrintaj et al., 2018).	Tissue engineering and drug delivery applications, such as tooth loss and cartilage regeneration (Zarrintaj et al., 2018).
Hyaluronic acid	Linear, high-molecular weigh natural polysaccharide, composed of repeating disaccharide units of β-1,4-D-glucuronic acid and β-1,3-N-acetyl-D-glucosamine (Lam et al., 2014; Zhu et al., 2017).	Biocompatibility, biofunctionality, tunable properties, can exist as a highly hydrated molecule, different properties in high and low molecular weight, increased level of HA in ECM causes cancer malignancies, and major component of the ECM in the cartilage (Highley et al., 2016; Lam et al., 2014; Zhu et al., 2017).	Scaffold in tissue engineering, dermal fillers, intra-articular viscosupplements, corneal and dermal wound repair, and post-surgical adhesion prevention (Highley et al., 2016; Lam et al., 2014).
Chitosan	The derivative of chitin, composed of glucosamine and N-acetylglucosamine (Jiang et al., 2014; Zhu et al., 2017).	Antibacterial properties, good processability, structurally similar to glycosaminoglycan, present in ECM of cartilage (Jiang et al., 2014; Zhu et al., 2017).	In tissue engineering as an artificial extracellular matrix material and engineered heart tissue based on chitosan hydrogel (Bush et al., 2016; Jiang et al., 2014).
Collagen	3 helix popypeptidic chains. The polypeptidic fibrils can have a diameter of 10-500 nm, an approximate molecular weight of 285 kDa, and a length of 1400 amino acids (Rodríquez et al., 2018).	Facilitates cell adhesion and growth, slow gelation, major component in connective tissues, the most abundant structural protein in the human body, provides structural stability and strength to numerous tissues, such as skin, bone, cartilage or even teeth (Ng et al., 2018; Ozbolat, 2017; Rodríquez et al., 2018).	Cosmetics, medicine, e.g., collagen cross-linking for the treatment of keratitis in adults (Lim & Lim, 2018; Rodríquez et al., 2018).
Soy protein	A mixture of albumins and globulins, 90% of which are storage proteins with globular structure (Tian et al., 2018).	Thermoplastic nature, inherent biocompatibility and flexibility, mechanical, structural and degradation properties can be altered using appropriate crosslinking and fabrication techniques (Chien et al., 2013; Lin et al., 2016).	Thin films, granules, hydrogels, and scaffolds (Chien et al., 2013).
Gellan gum	Natural polymer with repeating units consisting of α-L-rhamnose, β-D-glucose and β-D-glucoronate (I. Yu et al., 2017).	Different cations, such as Na+, K+, Ca2+ and Mg2+, can influence on the gelation properties, heat, and acid stability (I. Yu et al., 2017).	Ophthalmic formulations, oral drug delivery and scaffolds (I. Yu et al., 2017).

3.2. *Challenges in 3D bioprinting*

3D bioprinting is a relatively new research area and it faces challenges in terms of specific technical, material, cellular, financial, and clinical aspects of the process (Francis & Bulletin, 2015; Radenkovic, Soulouk & Seifalian, 2016; Sadri-Ardekani & Atala, 2016; Sultan et al., 2017; Lee & Dai, 2017). Compared with traditional 3D printing, 3D bioprinting involves complexities, including the choice of materials, cell types, growth and differentiation factors, technical challenges related to the sensitivities of living cells and the construction of tissues**,** biocompatibility requirements with living cells and ECM, and the need to mimic the cell-matrix architectures and mechanical properties of the native tissues. Thus, it is essential to develop new technologies and biomaterials for 3D bioprinting, understand the complex cell-matrix interactions behind certain properties, and establish proper vascular perfusion in bioprinted tissues (Lee & Dai, 2017)**.**

The central technical challenges considering 3D bioprinting include adaptation of technologies designed to print molten plastics and metals in 3D printing to the bioprinting of living biological materials and reproduction of the complex micro-architecture of ECM components and multiple cell types in sufficient resolution to obtain biological functions (Murphy & Atala, 2014). To take an example, 3D bioprinting of organs is challenging due to their complex native structures, which can consist of dozen or more cell types, and a need for a realistic vascular system that carry nutrients to the cells (Zhang et al., 2016; Savage, 2016). Furthermore, cells that are not within 200 µm from a nutrient source, die (Savage, 2016). Other common technical and material related challenges in 3D bioprinting are collapsing, shape fidelity, shrinking and swelling of the hydrogels, clogging of the nozzle-based fabrication methods, and, on the other hand, homogeneity, miscibility, print pattern and charge of the materials of the bioinks, the type of added bioink components, and the viscosity increase of the bioinks due to the CNF already at low concentrations (Derakhshanfar et al., 2018; Leppiniemi et al., 2017; Markstedt et al., 2015; Markstedt et al., 2017; Sultan et al., 2017).

Collapsing is typical for bio-based hydrogels, which is due to a low dry-matter content and low viscosity of the bioinks (Leppiniemi et al., 2017; Markstedt et al., 2015). On the other hand, shape fidelity is related to the viscoelastic properties of the bioinks. This means that the bioink should flow through the nozzle and retain its shape after printing and curing (Leppiniemi et al., 2017). However, it is a very challenging task to develop viscoelastic bioinks that can be readily extruded, and at the same time form self-supporting features after exiting the nozzle (Siqueira et al., 2017). Furthermore, swelling of the hydrogels need to be monitored and controlled to prevent blocking of the hydrogel pores which are important for the adequate transfer of the nutrients to the cells. The usual swelling of the hydrogels is approximately 10%. In addition, bioprinted hydrogels need to be kept in non-moving environment after fabrication, otherwise the position of cells inside the hydrogel can change.

When considering the homogeneity, miscibility and types of used materials for the bioinks, the successful printability requires homogeneous bioinks to enable a consistent flow without clogging while printing, which can be achieved using, e.g., speed mixer before 3D bioprinting to remove air bubbles (Markstedt et al., 2015; Markstedt et al., 2017). Miscibility also affects homogeneity of the bioinks, which can be enhanced with proper interactions between the bioink components, for example by proper cross-linking (Markstedt et al., 2017). On the other hand, print pattern may have a significant effect on the shape fidelity and stability, and strong charge can cause ionic repulsion which can later lead to a phase separation (Leppiniemi et al., 2017). In addition, adding components to ink can dilute the ink, possibly changing the rheological properties and influencing on cross-linking and printability (Markstedt et al., 2017).

The cellular challenges, in turn, include the cell-damaging steps of production processes, e.g., exposure to chemical cross-linkers during storaging, mechanical stress, toxic solvents, high temperatures and strong UV laser during 3D bioprinting process, limitations of each 3D bioprinting technologies in terms of resolution, speed and biocompatibility, challenges in analyzing cell behaviors *in situ* in hydrogel systems, limited supply of nutrients in the printed 3D constructs, and poor availability

of suitable biomaterials (Axpe & Oyen, 2016; Liu et al., 2017; Short et al., 2017; Lee & Dai, 2017). In more detail, current choice of materials for soft tissue bioprinting in comparison to hard materials without cell embedment is very limited and already existing materials cannot fully mimick the composition of native ECM. This increases the need to find and adapt new materials to improve the cell survival rate. (Liu et al., 2017; Lee & Dai, 2017).

On the other hand, the cost associated to 3D bioprinting as well as the design induced limitations also form their own challenges (Radenkovic, Soulouk, & Seifalian, 2016). 3D bioprinting of live cells using biological materials is significantly more expensive compared to the conventional 3D printing (Radenkovic, Soulouk, & Seifalian, 2016). However, these high values are reasonable if the scaffods can be used to cut the costs of organ transplantations (Radenkovic, Soulouk, & Seifalian, 2016). On the other hand, the poor transformation of the complex CAD design into machine instructions can result in the differences between the 3D model and the bioprinted object (Tappa & Jammalamadaka, 2018).

When considering clinical challenges in contrast to rapid development of 3D bioprinting technologies, the translation of 3D printing into clinical therapies has been very slow. Only few studies have utilized 3D printed scaffolds in preclinical models, not to mention in patients or in-patient clinical trials**.** However, the potential of 3D bioprinting to reduce the organ shortage, acts as the main driving force in translation of 3D bioprinting technologies and scaffolds into clinical medicine. (Francis & Bulletin, 2015).

In general, translational medicine studies have taken place in bone, cartilage, teeth, and skin regeneration (Francis & Bulletin, 2015). However, current preclinical and clinical studies have mainly focused on simple and hard tissues, such as bone and tooth regeneration and implantation, whereas soft tissue regeneration using 3D bioprinting simultaneously with living cells and its translation into medicine is still at very early stage (Lee & Dai, 2017). Only a few preclinical studies have been conducted for the regeneration of more complex, internal organs, e.g., lungs, kidneys, liver, and

heart (Francis & Bulletin, 2015). This is due to the many problems associated with the safe and sufficient clinical use of the 3D printed scaffolds, including the technical difficulties of scaffold production in mimicking complex structures, development and behavior of cells in terms of rate of vascularization, innervation and diffusion of metabolies, cell survival, safety of biomaterials, financial costs, abundant cell sources, and ethical aspects (Francis & Bulletin, 2015; Radenkovic, Soulouk, & Seifalian, 2016; Sadri-Ardekani & Atala, 2016; Lee & Dai, 2017). In addition, finding the optimal scaffold manufacturer protocol is a difficult task which also hinders the translation process of 3D bioprinting into applications of clinical medicine (Radenkovic, Soulouk, & Seifalian, 2016).

3.3. *Solutions and the future*

In the recent years, many exciting research attempts have been made considering 3D bioprinting technology and materials, from which personalized 3D bioprinting is becoming more and more popular in the future (Radenkovic, Soulouk, & Seifalian, 2016), and several companies are working with the applications of 3D bioprinting for the needs of regenerative medicine (Derakhshanfar et al., 2018). To take and example, Organov has recently introduced a bioprinted human liver for the commercial use (Derakhshanfar et al., 2018). In gerenal, 3D bioprinting industry is growing and is expected to grow even more in near future. According to Derakhshanfar et al. (2018), 3D printing market size is predicted to reach $10.8 billion in 2021 from $2.2 billion in 2012.

Nevertheless, as described in the previous Subchapter 3.2, there are many problems associated with 3D bioprinting. To overcome these problems, hydrogels can be printed in combination with other biomaterials, or using a combination of different hydrogel fabrication and cross-linking methods (Axpe & Oyen, 2016; Markstedt et al., 2015; Markstedt et al., 2017; Ullah et al., 2018). As an example, inkjet bioprinting technology can be used for fast printing in centimeter- and millimeter scale of certain tissue constructs, and microextrusion for the constructs in the microscale (Lee & Dai, 2017). This technology, also called multimaterial bioprinting, provides the ability to

adjust factors, such as concentration of growth factors, cell adhesion and degradation rate in the different regions of the bioprinted object, and enables to load different types of cells in different zones, allowing for closely mimicking of natural cellular diversity and acitivity (Derakhshanfar et al., 2018). Mixing of different technologies and materials, and the future progresses in it, can enable the fabrication of new tissues and organs with challenging structures and adequate cell viability and function.

The development of new printers and printing technologies will have an important role in this attempt. With a novel Kenzan bioprinter, cell spheroids are able to be bioprinted in a pre-designed manner to mimick the shape of the blood vessels (Itoh et al., 2015), whereas digital micro-mirror device-based projection printing (DMD-PP) could be used to fabricate user-designed vascular channels with the channel widths of 25-120 µm in a highly short time (Datta et al., 2017). On the other hand, bioplotting, in which air pressure is used to extrude the bioink, is appropriate to extrude low viscosity liquids, such as polymer melts, biopolymers, and nanocellulose gels, and to produce complex shapes that would be unfeasible through traditional manufacturing technologies (Rees et al., 2014). Elsewhere, gradual cross-linking of sodium alginate with calcium ions before, during, and after printing increases the printability of the alginate material and mechanical rigidity, layer adhesion capability, and overall structure stability of the 3D bioprinted hydrogels (Tabriz et al., 2015). A living body could also serve as a bioreactor for *in vivo* growth of scaffolds seeded with viable cells after 3D bioprinting (Ullah et al., 2018).

On the other hand, the tissue repair and drug delivery performance could be improved by using novel biorobots. There is an increasing demand for small, biocompatible robotic devices that can perform tissue repair, cargo transport, drug delivery, and to help to understand the locomotive mechanism of small-scale micro-organisms (Nagarajan et al., 2018). Williams et al. (2014) prepared a biorobot based on cardiomyocyte and polymethylsiloxane (PDMS) to model spermatozoa, whereas Park et al. (2017) developed a biorobot based on cardiac cells and PDMS body and modeled on an electric sting ray. In general, 3D bioprinting in the fabrication of

biorobots would decrease the manufacturing costs and enable an easy design and finetuning of these devices with improved motility for various biomedical applications (Nagarajan et al., 2018).

In relation to the new findings considering bioinks, the use of high concentration bioinks of CNF are expected in the near future, helping to develop materials with new mechanical, structural, and functional performance (Sultan et al., 2017), whereas the preparation of dynamic, switchable, and oxygen producing hydrogels could provide the base for establishing strategies to control cell microenvironment (Ullah et al., 2018), and possibly enhance cell survival. Another extremely interesting research area, which may have a big potential in the future, is the fabrication of patient-specific bioinks based on the platelet-rich plasma (PRP) as a source of the patient-specific growth and biological factors with enhanced stem cell migration and vascularization (Faramarzi et al. 2018).

One increasing future approach in the case of 3D bioprintable inks may also be lignin. Lignin could act as a filler or structure stabilizer in the 3D bioprinted hydrogels and, on the other hand, behave as an active compound in delivering substances to the cells (Dai et al., 2019; Xu et al., 2018). This feature might be extremely good in the accurate delivery of growth factors for cell differentiation, fabrication of many proliferated cell lines inside the hydrogel, and in creating the suitable and best possible environment for tissue or organ regeneration. In the end, in the Table 4, some more recent and promising researches considering 3D bioprinting and bioinks, to overcome the current problems, has been collected.

Table 4. *A short summary of the recent, interesting 3D bioprinting and bioink studies using different biomaterials, biofabrication technologies, and cell sources.*

Material	wt%	Technology	Cell type	Application	References
Alginate-based	-	Compatible with commercial bioprinters	PRPs containing patient-specific biological factors	New patient-specific bioinks containing PRPs, ultimately enhancing stem cell migration and vascularization	Faramarzi et al. (2018)
Na-alginate, poly(ethyleneglycol)-diacrylate (PEGDA) and calcium sulfate slurry hydrogel	5 Na-alginate 40 PEGDA	Extrusion	Human embryonic kidney (HEK) cells	Tough and 3D-printable hydrogel for long-term cell culture	Hong et al. (2015)
Spider silk proteins eADF4(C16) and eADF4(C16)-RGD hydrogel	3 spider silk protein	Robotic dispensing	BALB/3T3 mouse fibroblasts	The recombinant spider silk hydrogels can be printed without additives or additional crosslinking	Schacht et al. (2015)
Sodium alginate-gelatin (SA/Gel) hydrogel ink reinforced with CNCs	70 CNC 20 SA 10 Gel 0 water	Extrusion	-	Fully bio-based porous scaffolds of a double crosslinked interpenetrating polymer network (IPN). Has a potential in developing bio-based scaffolds with controlled pore sizes, gradient pore structures and alignment of nanocrystals for optimal tissue regeneration	Sultan & Mathew (2018)
Agarose and collagen hydrogel	9:1	Inkjet	HEK cells and ovine mesenchymal stem cells (oMSCs)	Printing of cells using a low-cost, novel droplet-based bioprinter with a resolution better than extrusion- and valve-based printers and better cell density compared to inkjet printers	Graham et al. (2017)
Silk-fibroin (SF) and gelatin hydrogel in combination with BMSC-speficic-affinity peptide	6.9 SF, with mass ratio of 1/2 6.9 Gel	-	Endogenic bone marrow stem cells (BMSCs)	Promising hydrogel for knee joint repair and possibly for the regeneration of other joint cartilages	Shi et al. (2017)
Gellan gum (GG) and PEGDA hydrogel	0.75 GG 15 PEGDA	Extrusion	Bone marrow stromal cells	Due to the biocompatibility and suitable mechanical properties, this hydrogel has a potential to assist intervertebral disc (IVD) regeneration	Hu et al. (2018)
Enzymatically-treated CNF (E-CNF) and HA hydrogel	70 E-CNF 30 HA	-	Mouse mesenchymal stem cells	Using this hydrogel, adipose models could be formed in one-step operation with good reproducibility and cell viability	Henriksson et al. (2017)
Polylactic acid (PLA) and alginate hydrogel	2.5 % alginate 0.5 % PLA	Extrusion	Human adipose-derived stem cells (hASC)	Development in controlling the distribution and alignment of nanofibers in bioprinted constructs, mimicking the native fibrous organization of musculoskeletal soft tissues	Narayanan et al. (2016)
Tissue strand bioink from chondrocytes	-	Extrusion	Chondrocytes	New scaffold-free bioinks utilizing tissue strands for the applications of tissue engineering and regenerative medicine	Yu et al. (2016)
A hydrogel bio-bot based on engineered muscle and PEGDA	3D bioprinted PEGDA hydrogel Skeletal muscle myoblasts ECM proteins	Stereolithography	Skeletal muscle myoblasts from mouse myoblast cell line C2C12	A bio-hybrid robot in developing enhanced drug screening, programmable tissue engineering, drug delivery, and biomimetic machine design	Cvetkovic et al. (2014)

EXPERIMENTAL

4. Objectives of the work

The object of this Master's thesis is to test the hypothesis, according to which the addition of CLPs prevents hydrogel shrinking upon drying. This is done by preparing CLP-CNF-alginate bioinks with varying CLP concentrations and studying their rheology, printability, compression, and in the end, their structural stability in different storage conditions. The ultimate objective is to make lignin in the form of CLPs a multifunctional and promising material option for 3D bioprinting in regenerative medicine.

5. Materials

5.1. *Nanofibrillated cellulose (CNF)*

Bleached birch wood pulp fibres were utilized for the TEMPO-oxidized CNF and unmodified CNF. 1.5 liters of TEMPO-oxidized CNF was prepared according to the instructions in the Subchapters 5.1.1 - 5.1.4, whereas 1 liter of 2.5% unmodified CNF was provided by Aalto University, after prepared according to the articles of Pääkkönen et al. (2016) and Rojo et al. (2015). The preparation of 2.5% unmodified CNF consisted of washing the birch wood pulp fibres to sodium form prior to the disintegration in the fluidizer, dilution of the alkaline treated pulp, disintegration of the pulp suspension with M-110P fluidizer using six passes, and storing the resulted 2.5% unmodified CNF in the fridge at 4 °C.

5.1.1. *Alkaline treatment of cellulose pulp*

Alkaline treatment of cellulose was used as a pre-treatment before TEMPO-oxidation to increase the anionic charge due to the carboxylic acid groups, -COOH, that form during the oxidation. First, cellulose fibres were ripped by hand into smaller pieces of about 1 mm of length. This was followed by weighing, and the weight of the cellulose

pieces obtained was 90.04 g. Next, the cellulose pieces were poured into 1 liter of 1 M sodium hydroxide, NaOH, and stirred to homogeneity.

After 15 minutes, the alkaline cellulose pulp was washed with tap water and finally with deionized water, until the value of pH reached 9.9. The total consumption of water was approximately 20 liters. Next, the washed cellulose was added in small amounts into a mixing machine (Kenwood electronics) and mixed until the texture was the desired one. After the mixing, the cellulose was pressed and added into a plastic bag. The final weight of the moist sodium cellulose was 309.58 g.

Dry weight analysis was conducted for the cellulose. After cellulose had been kept in the oven overnight, the sample was let to cool in the desiccator for 15 minutes before the final measurement. The dry matter content of washed cellulose was 34%, and the amount of moist cellulose required for the TEMPO-oxidation was 205.79 g. The calculations for the dry weight analysis and the amount of moist cellulose can be found in the Appendix 1. The different steps of alkaline pre-treatment of cellulose are also shortly listed in the Figure 10.

Figure 10. *Different steps of alkaline treatment of cellulose.* ***A.*** *Ripped cellulose fibre mats.* ***B.*** *Cellulose mass after 15 minutes of immersion in 1 M NaOH.* ***C.*** *Washed cellulose mass.* ***D.*** *Finished sodium cellulose fibres ready for TEMPO-oxidation.*

5.1.2. TEMPO-oxidation of cellulose

Preparations for TEMPO-mediated oxidation, shortly TEMPO-oxidation, of cellulose consisted of the preparation of TEMPO-catalyst and titration of hypochlorite, ClO^-. TEMPO-catalyst was used in the TEMPO-oxidation of cellulose and titration to

estimate the used thiosulfate, $S_2O_3^{2-}$, consumption in TEMPO-oxidation. In the preparation of TEMPO-catalyst, 0.572 g of TEMPO-catalyst was measured together with 41.574 mol of distilled water, after which the solution was let to react in a container over the weekend. After the reaction, 4 ml of hypochlorite was added, followed by shaking of the container by hand and pipetting of sulfuric acid, H_2SO_4, (1 M) to adjust the pH around 7.

In the titration of hypochlorite, 10 ml of potassium chloride, Kl, (10 %) and 20 ml of sulfuric acid (1 M) was added into the beaker, followed by the addition of 0.5 ml of hypochlorite. The solution was titrated using 19.58 ml of sodium thiosulfate, $Na_2S_2O_3$, (0.101 mol/l), until the color of the solution started to lighten up. Starch was added in the middle of the titration to achieve a blue color and titration was conducted, until the equivalent point was reached. The equivalent point was reached when the color of the solution became transparent. The obtained thiosulfate consumption was 19.755 ml, the average of two separate titrations.

After the preparations, TEMPO-oxidation of cellulose was started. In the beginning, 205.803 g of washed cellulose, that contributed to the dry weight of 50 g of dry cellulose, was poured to the Büchiglasuster bmd 300 reactor apparatus together with 1.5 liters of distilled water. This was followed by the addition of 825 g of distilled water and the previously prepared TEMPO-catalyst. To start the reaction and adjust the pH to the desired level, 125 ml of hypochlorite was measured and added into the reactor small amounts at a time. The reaction started immediately when pH started to decrease due to the addition of hypochlorite. After this, pH was measured continously. When the reaction speed slowed down, and the hypochlorite concentration decreased in the reactor apparatus, small amounts of 4% NaOH (1 M) was added to maintain pH 8 - 9. The overall consumption of 1 M NaOH during the reaction was 114.3 g, until the reaction was stopped after 4 ½ hours.

In the end of TEMPO-oxidation, the reacted cellulose was washed with deionized water for about four times. Alltogether, 320.1 g of moist TEMPO-oxidized cellulose was obtained at dry weight of 13% and 82.11% yield. The calculations of the dry

weight analysis and yield of the TEMPO-oxidized cellulose can be observed in the Appendix 1. The steps of TEMPO-oxidation of cellulose are also summarized in the Figure 11 below.

Figure 11. *The steps of TEMPO-oxidation of cellulose.* **A_1.** *TEMPO-oxidized cellulose was added into the Büchiglasuster bmd 300 reactor.* **A_2.** *The TEMPO-catalyst was added into the reactor together with distilled water.* **B.** *4% NaOH (1 M) was pipetted to keep the pH in the range of 8 - 9. The reaction lasted for 4 ½ hours.* **C.** *In the end of the reaction, the TEMPO-cellulose was poured to the Viira bag for washing.* **D.** *The obtained, weighed, and mashed TEMPO-cellulose ready for the dry weight analysis.*

5.1.3. Acid treatment of TEMPO-oxidized cellulose

The acid treatment of TEMPO-oxidized cellulose was performed to enhance the separation of the fibres in fluidization using the repulsion of the metals in their ion form, such as Na^+. Metals in their ion form also enhanced the non-packing of the cellulose fibres. In the beginning of the treatment, 32.0 g of TEMPO-oxidized cellulose was weighed into the beaker and diluted to 1.5 kg with deionized water. A little amount of 1 M HCL was added into the beaker, and the pH of TEMPO-oxidized cellulose was adjusted to 1.8, so that the protonization of the cellulose occurred. Protonization made the structure of cellulose more fluid-like.

Next, the obtained TEMPO-oxidized cellulose solution was let to mix and react using the magnetic stirrer for about 50 minutes, which was followed by the conductivity measurements. The obtained conductivity of TEMPO-oxidized cellulose was 0.8

microsiemens/cm, and the limit for the conductivity 5. After the conductivity measurement, TEMPO-oxidized cellulose was washed for five times with the beaker and once straight from the tap with Viira bag, ripped by hand into smaller pieces to enhance the dry matter of the cellulose, and moved into the plastic bag. The plastic bag was gently mashed to enhance the dry matter content of the cellulose, followed by the dry weight analysis. The dry weight of the moist cellulose was 25.92% and yield 90.90%. The calculations of the dry weight analysis and yield of the acid-treated TEMPO-oxidized cellulose can be seen in the Appendix 1.

In the next step, conductometric titration was conducted using Methrom's 751 GPD Titrino to obtain the amount of carboxylic acid groups, -COOH, in the TEMPO-oxidized cellulose backbone. In the beginning of this measurement, 1.126 g of the acid treatred TEMPO-cellulose, 1.5 liters of Milli-Q water from which air and acidic CO_2 had been removed in ½ hours, 1 ml of NaCl (0.5 M), and 0.5 ml of HCl (1 M) were weighed into the beaker. TEMPO-oxidized cellulose was let to disperse for approximately 10 - 15 minutes to make the conductometric titration work better, followed by the titration. During the titration, the speed was lowered to 300 rpm soon after the starting, and the titration was let to proceed for a litte bit over 20 hours.

Titration curves were analyzed using Origin 2018b software. The amount of first results was 1.21 mmol COOH/g pulp. After two hours, the second results were obtained, and the measurement was ended. The carboxylic acid group content was 1.26 mmol COOH/g pulp. The average of these two measurements was approximately 1.23 mmol COOH/g pulp. The overall consumption of NaOH was 0.368 mmol at the velocity of 0.1 ml/min.

5.1.4. Fluidization of TEMPO-oxidized cellulose

The fluidization, to obtain the CNF fibres, was started with the dilution of TEMPO-oxidized cellulose. 233.7 g of TEMPO-cellulose was weighed and diluted with deionized water until the overall weigh of 1119.9 g ≈ 1.2 kg was reached. Next, pH

was adjusted to 9 with pipetting 1 M NaOH drop by drop. This dilution and adjusting of pH of TEMPO-cellulose was followed by fluidization. The utilized fluidizer was Microfluidics M-110P produced by Microfluidics™, USA. The fluidization was started with the initial preparations. During the fluidization of over 45 minutes at the pressure of 2000 bars, 2% TEMPO-cellulose was constantly added into the fluidizer, when the tube got empty, at the same time CNF being produced as a long tube, and a bag of ice was kept on the machine during the process to keep the fluidizer cool. The obtained TEMPO-CNF was stored in the fridge at 4 °C. The steps of the fluidization are also shortly summarized in the Figure 12 below.

Figure 12. *The steps of the fluidization process.* **A.** *TEMPO-oxidized cellulose was diluted to the desired weight and concentration by adding deionized water.* **B.** *The deionized water was used for cleaning the fluidizer, followed by the addition of 2.5% and 2% TEMPO-cellulose into the tube located on the left in the Microfluidics M-110P fluidizer.* **C.** *TEMPO-cellulose was prosessed through the tubes of the fluidizer in the pressure of 2000 bars. CNF fibres were produced simultaneously when TEMPO-cellulose was added.* **D.** *2.0% CNF fibres were obtained. The fluidizer was again cleaned by the distilled water.* **E.** *A closer look of the produced CNF fibres. Fibres were long, gel-like tubes which maintained their structure.*

5.2. *Colloidal lignin nanoparticles (CLPs)*

UPM BioPiva^{TM} lignin from softwood kraft pulping was utilized for the preparation of the CLPs. The CLP preparation included five main steps. These were **1)** dissolution of

lignin, **2)** self-assembly/nanoprecipitation of CLPs in water, **3)** dialysis to remove the organic solvent, **4)** concentration by rotary evaporation, and **5)** freeze-drying of the CLP dispersion. These different steps are shortly presented in the Figure 13 below, followed by the detail descriptions.

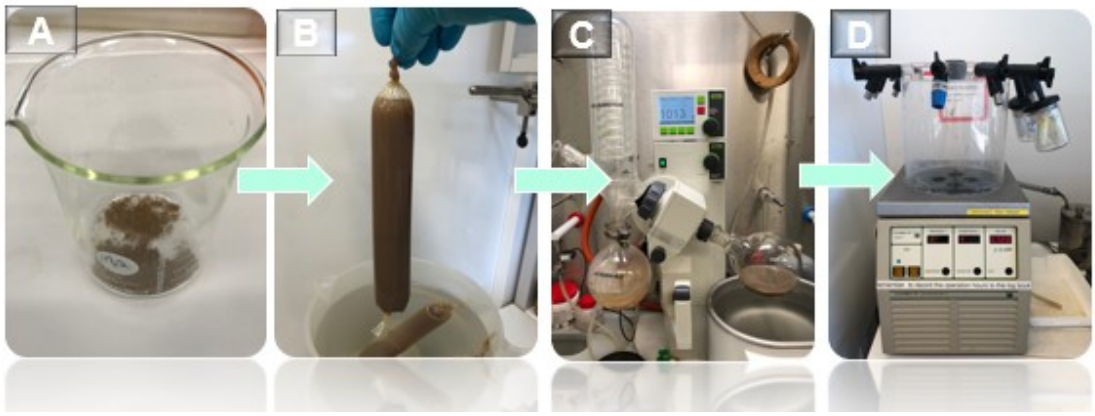

Figure 13. *The different steps of the preparation of colloidal lignin particles (CLPs).* **A**. *The process was started with mxing the different reagents, including water, acetone, and lignin as the form of powder, in a specific order to obtain CLPs with the defined particle size. The particle size of the CLPs was dependent on the pouring speed of the lignin-water-acetone solution into water.* **B.** *The next step was the dialysis of the generated CLP-water-acetone dispersion in the filter paper sausages. During the dialysis, the excess acetone was removed from the sausages into the surrounding water. This step also included the particle size determination of the CLPs.* **C.** *The following step was the rotary evaporation and concentration of the CLP dispersion. In this step, the certain amount of water was evaporated from the dispersion until the overall weight of approximately 150 g was reached.* **D.** *The preparation ended to the freeze-drying process of the CLPs into the solid form for the bioink preparation.*

The preparation of the colloidal lignin particles (CLPs) was started by weighing 2.288 g of 65.6 wt% lignin, 37.49 g of distilled water and 112.5 ml of acetone into the beaker, after which the lignin was dissolved in a capped beaker using a magnetic stirrer at the temperature of 22 °C for three hours. After three hours of stirring, the solution was filtered using a Whatman© glass microfibre filters GF/F to remove the undissolved particles. This was followed by the quick pouring of the solution to the 450.16 g of water in two seconds using a magnetic stirrer, after which the resulted dispersion was let to stir for 15 minutes. The faster the pouring, the bigger the particle size of CLPs.

CLPs were purified by dialysis against deionized water using SpectraPos dialysis membrane with 6 - 8 kD as the pore size. The weight of the CLP dispersion after the

dialysis was 712.68 g, and the dry weight of the CLPs after the dry weight analysis 0.211%. The calculations for the dry weight analysis of the CLP dispersion can be seen in the Appendix 1. This second step also included the particle size determination of the CLPs through the dynamic light scattering (DLS) measurements. Before the DLS measurements, the CLP dispersion was filtered using Whatman© glass microfibre filter GF/F with the pore diameter of 0.7 µm to remove the bigger particles and therefore, to prevent later aggregation. In the DLS measurements, instrument of Malvern and the software of Zetasizer produced by Malvern Panalytical Ltd, UK, was used, and two measurements were conducted.

According to the measurements, the mean particle diameter, Z-average, of the CLPs was 103.0 nm, whereas the width of the particle size distribution, polydispersity index (PDI), was 0.108. According to Shaw (2015), the obtained range is the mid-range value of PDI. These results indicate that the prepared CLPs are not monodisperse but slightly polydisperse with an average distribution of the particle sizes (Shaw, 2015). The results from the particle size determination can be observed in more detail in the Table 5 below.

Table 5. *Particle sizes of the CLPs obtained from the DSL measurements.*

1:2, water to lignin solution		
	Z-average	**PDI**
Mean	103.0	0.108
Standard deviation	1.609	0.003

The fourth step was the rotary evaporation and concentration of the CLP dispersion at the temperature of 50 °C. Rotavapor R-210 apparatus from Büchi was used to evaporate 712.68 g of 0.211 wt% CLPs to a final weight of approximately 150 g. The concentrated CLP dispersion was freeze-dried using the Labconco Freezone Plus 4.5 Litre Benchtop Freeze Dryer. The weight of the generated CLPs was 3.051 g and the yield 75.0%. The calculations considering the yield of the CLPs can be seen in the Appendix 1.

5.3. *Excipients*

The excipients used for the bioink preparation, 3D bioprinting, and storage methods included the alginate solution and gel, cross-linking solution based on 0.09 M calcium chloride, $CaCl_2$, together with salt-water solution. To begin, 0.5% alginate solution was prepared by weighing 1.25 g of alginate powder, product #180947-500G, from Sigma Aldrich into the beaker and adding distilled water, until the overall weight of 50 ml was reached. 10% alginate gel was prepared by weighing 1 g of alginate powder from Sigma Aldrich and 9 g of distilled water into the beaker, by stirring with spatula and later overnight by the magnetic stirrer.

0.09 mol/l of cross-linking solution based on $CaCl_2$ was prepared by weighing 13.232 g of $CaCl_2$ into the flask of 1000 ml, which was followed by the addition of distilled water, until the overall weight of 1 liter was achieved. Furthermore, an aqueous buffer solution was prepared by weighing 0.200 g of $CaCl_2$ (Merck, purity 98%), 0.093 g of magnesium sulfate (anhydrous), $MgSO_4$ (VWR Life Science, purity $\leq$ 99.5%), 3.700 g of sodium bicarbonate, $NaHCO_3$ (VWR BDH Chemicals, purity 100%), 6.400 g of sodium chloride, NaCl (VWR BDH Chemicals, purity 99.9%), 0.100 g of sodium phosphate monobasic (anhydrous), NaH_2PO_4 (Fluka, purity $<$ 99.0%), and 0.400 g of potassium chloride, KCl (Merck, purity 99.5%), into a 1000 ml flask, followed by the addition of distilled water, until the overall weight of 1 liter was reached. The composition of the salt-water solution was adapted from the Dulbecco's Modified Eagle's Medium (DME) from Sigma Aldrich and inspired by the articles of Laurén et al. (2017) and McKee & Komarova (2017).

5.4. *Bioinks*

The materials prepared in the previous Subchapters 5.1 - 5.2 were utilized in preparing the bioinks, according to the recipe of the CNF-alginate bioink adapted from Markstedt et al. (2015). In this bioink preparation process, alginate powder was first dissolved in water, followed by the dissolution of the CLPs with the B. Braun's (HT) shaker for overnight, and the addition of either CNF or T-CNF. This

homogenization of sodium alginate and CLPs in water also diluted the initial CNF concentration from 2.5 wt% to 2 wt%, and the initial T-CNF concentration from 2.0 wt% to 1.9 wt%.

After the addition of the different components, the bioinks were centrifuged to remove all the air bubbles, making them more suitable for 3D bioprinting. The Centrifuge 5804 R from Eppendorf and the fixed-angle rotor FA-45-6-30 with Eppendorf Quicklock© lid was used with the centrifugation radius of 12.3 cm and the relative centrifugal force (RCF) of 220. The evaluation of the proper centrifuging parameters is more thoroughly described in the Chapter 7. The appearance of the different bioinks and their preparation methods are presented in more detail in the Figure 14, and the compositions of the bioinks used in the Table 6 below.

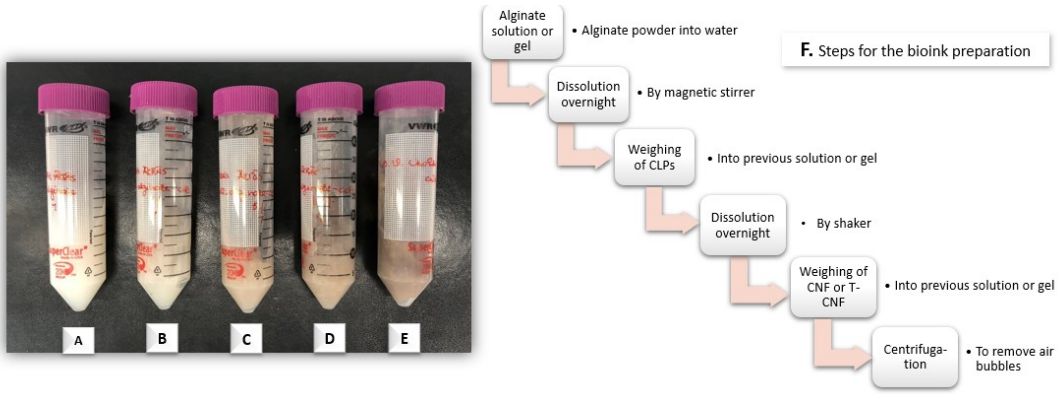

Figure 14. *The appearance and preparation steps of the various bioinks. It is evident that the colour of the bioinks turn into more brownish with the increased CLP concentrations.* **A.** *CNF-alginate bioink.* **B.** *1% CLP-CNF-alginate bioink.* **C.** *5% CLP-CNF-alginate bioink.* **D.** *10% CLP-CNF-alginate bioink.* **E.** *25% CLP-CNF-alginate bioink.* **F.** *Steps for the bioink preparation in short in the form of a scheme.*

Table 6. *The compositions and preparation methods of the different bioinks.*

Bioink composition	Initial CNF (wt%)	CNF: bioink (wt%)	CNF: bioink (g)	Alginate: bioink (wt%)	Alginate: bioink (g)	Water: alginate solution/gel (g)	Alginate solution/gel: bioink (g)	CLPs: bioink (wt%)	CLPs related to CNF (wt%)	CLPs: bioink (g)
CNF-alginate	2.5	**2.0**	16	**0.5**	0.1	4.0	4.0	**0**	**0**	0
T-CNF-alginate	2.0	**1.9**	19	**0.5**	0.1	9.0	1.0	**0**	**0**	0
1% CLP-CNF-alginate	2.5	**2.0**	16	**0.5**	0.1	4.0	4.0	**0.02**	**1**	0.00400
5% CLP-CNF-alginate	2.5	**2.0**	16	**0.5**	0.1	4.0	4.0	**0.10**	**5**	0.02000
10% CLP-CNF-alginate	2.5	**2.0**	16	**0.5**	0.1	4.0	4.0	**0.20**	**10**	0.04000
25% CLP-CNF-alginate	2.5	**2.0**	16	**0.5**	0.1	4.0	4.0	**0.50**	**25**	0.10000

6. Methods

6.1. *Rheology measurements*

Anton Paar MCR302 rheometer with the Anton Paar's RheoCompass software was utilized for the rheology measurements. For these measurements, the parallel-plate geometry with both the serrated and plain bottom and upper plate was selected. The plate type used was PP25 with the diameter of 25 mm, and the gap between the plates was 1 mm. The serrated plates were used for the oscillatory amplitude sweep measurements to prevent the wall slip effect, whereas the dynamic viscosity measurements based on the shear forces were conducted with the plain plates. All the measurements were done in the temperature of 23 ˚C. The objective of these rheology measurements was to study the viscosities, shear-thinning properties, linear viscoelastic region (LVR), strength, and the viscoelastic nature of the bioinks to offer information about the printability of the bioinks and the effect of the different bioink compositions on the bioink characteristics.

As mentioned before, two different measurements were conducted, dynamic viscosity and amplitude sweep measurements. The initial measurement set up and parameters were adjusted according to the article of Pääkkönen et al. (2016), and the measurements were repeated at least twice. In the dynamic viscosity measurement, the change in the dynamic viscosity, (Pa·s), values were recorded with the increased shear strain, γ (1/s), and the data obtained was used for the viscosity and shear-thinning studies of the bioinks. The density of the bioinks was calculated for the measurement, and the applied strain varied between 0.01 1/s and 100 1/s. The density value for all the bioinks was ≈ 1 g/cm^3.

In the amplitude sweep measurement, the changes in the storage modulus, G' (Pa), and loss modulus, G'' (Pa), were recorded with the increased oscillatory strain, γ (1/s), and the data obtained was utilized to study the LVR, strength, and material type of these bioinks. This amplitude sweep measurement consisted of three intervals, which were preshear protocol, resting time, and the amplitude sweep test. The preshear protocol took for 3 minutes with 25 data points, constant measurement duration, at

the angular frequency of ω = 10 rad s^{-1}, and at the strain amplitude of γ = 0.01 %. This was followed by the resting time for 10 minutes by steady state mode with one data point. The 3rd interval was the oscillatory test, in which the measurement was conducted using 25 data points, the steady state measurement duration, the constant frequency of ω = 1 rad s^{-1}, and the varying strain amplitude of γ = 1 – 1000 %. The used instrument and the measurement info are summarized in the Figure 15 below.

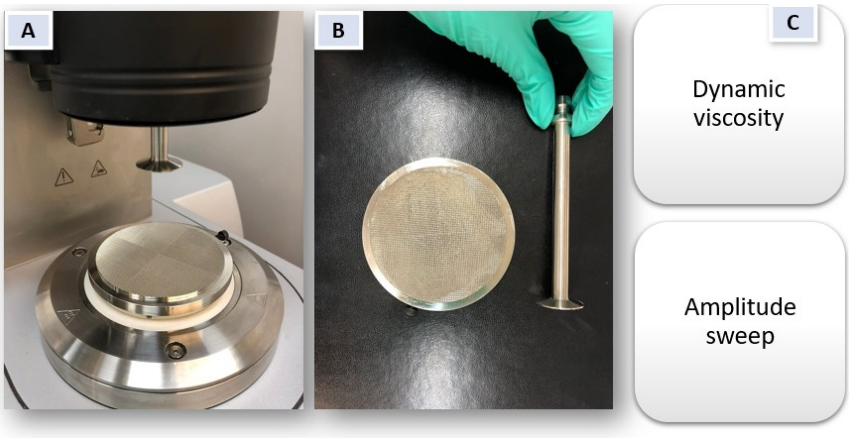

Figure 15. A. *A photo of the Anton Paar MCR302 rheometer. The bioink was placed in the centre of the upper and lower plates, firmly pressed in between them, trimmed, and measured. The measurements were based on either one-way shear or oscillatory operation, from which only the oscillatory amplitude sweep measurements were able to be repeated with the same bioink without the structural destruction.* **B**. T*he serrated plates used for the amplitude sweep measurements to prevent the wall slip effect. The plain plates look similar but have a smooth surface.* **C.** *The measurements conducted for the bioinks. The dynamic viscosity measurement was used for studying the viscoelastic behavior of the bioinks, whereas the amplitude sweep measurement revealed, e.g., the nature and the inherent strength of these bioinks.*

6.2. 3D bioprinting

A 3D model in the shape of cylinder for 3D bioprinting was obtained from the website of Thingiverse (Anon. 2018), and customized using a 3D modelling software called OpenSCAD for the needs of the Master's thesis. The dimensional tests for the hydrogels were conducted with the CNF-alginate and CLP-CNF-alginate bioinks. The final dimensions for the hydrogels were set to be 2.0 cm for the hydrogel height and 1.5 cm for the hydrogel width, because the diameter of 1 cm was too small for

preventing the structure from collapsing with the CNF-alginate bioinks, whereas the maximum height obtained with the CLP-CNF-alginate bioinks was only 2 cm. The number of layers for the cylinder-shaped hydrogels were obtained from the equation (1) below. In these calculations, the tip diameter of 0.41 mm was used. The Figure 16 below shows the appearance and info of the prepared 3D model used in 3D bioprinting, and the Equation (1) the calculations for the hydrogel layers.

$$The\ number\ of\ hydrogel\ layers = \frac{Hydrogel\ height\ (mm)}{Tip\ diameter\ (mm)} = \frac{20\ mm}{0.41} = 48.7805\ \approx 49 \qquad (1)$$

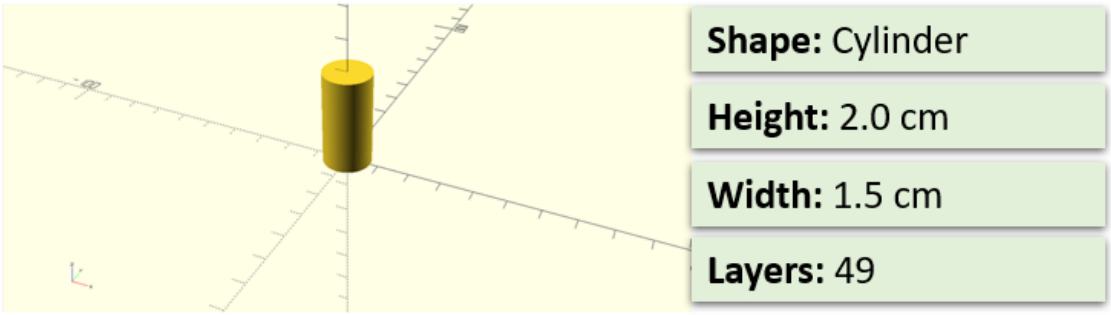

Figure 16. *The 3D model prepared for 3D bioprinting with the OpenSCAD software. The height of the cylinder was 2.0 cm, width 1.5 cm, and the number of layers within the cylinder 49. The structure was simple enough to be printed, but tall enough, so that the possible collapsing and other happenings during the storaging would be easier to detect.*

The bioprinter BioX from Cellink© was used for the 3D bioprinting process. The bioprinter consisted of alltogether 3 printheads. In this Master's thesis, a 3 ml syringe was used. One bioink bottle prepared consisted of 20 ml of the bioink, which was required for the bioprinting of four to five cylinders with the height of 2.0 cm and width of 1.5 cm. In total, five bioprinted hydrogels per one bioink composition were needed for the further measurements. All the bioink compositions were bioprinted according to the same steps described next. The steps are also generally listed in the Figure 17 below.

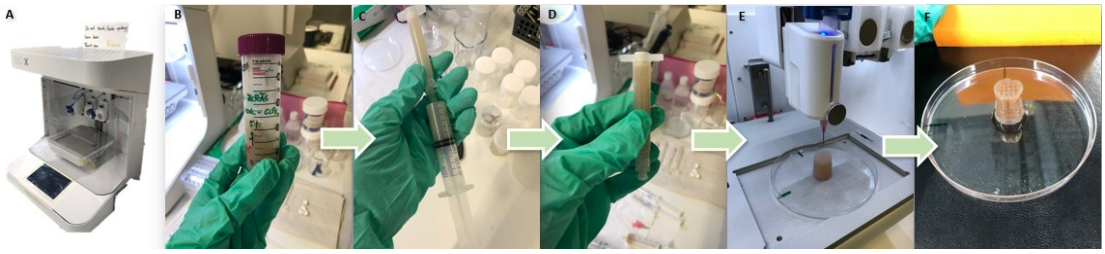

Figure 17. *The steps of 3D bioprinting and a photo about the 3D bioprinter.* **A.** *The BioX 3D bioprinter used in this Master's thesis.* **B.** *The bioink was added into the syringe with a spoon.* **C.** *The bioink was syringed into the 3 ml 3D bioprinting syringe.* **D.** *The syringe was placed into the specific printhead in the 3D bioprinter, followed by the addition of the petri dish and tip.* **E.** *After the required settings, the pressure was adjusted during the 3D bioprinting to ensure the desired hydrogel structure.* **F.** *After the 3D bioprinting, the hydrogels were photographed, crosslinked with 0.09 M $CaCl_2$, and stored.*

The 3D bioprinting was started by gently adding some bioink with a spoon into a syringe, only carefully tapping the bioink to prevent the formation of the air bubbles. Next, the bioink was injected into the 3D bioprinting syringe with the volume of 3 ml and attached into a specific printhead in the 3D bioprinter. Petri dish was moved onto the printbead as a bioprinting platform, the tip of 0.63 mm was placed into the printhead, and the settings were adjusted. The pressure was controlled during the 3D bioprinting according to the viscosity of the hydrogel.

In the end of the 3D bioprinting, the obtained hydrogels for the free-standing measurements were photographed and cross-linked using 0.09 M $CaCl_2$ solution in 5 minutes. The other obtained hydrogels were also photographed and tentatively cross-linked using 0.09 M $CaCl_2$ solution in five minutes, by adding a few drops of the solution on top of the hydrogels, and then pouring the hydrogels into the container containing 0.09 M $CaCl_2$. The pouring cross-linked the whole hydrogel. The fully cross-linked hydrogels immersed in the 0.09 M $CaCl_2$ solution for the DMA were stored in the fridge for the next day, while the rest of the fully cross-linked hydrogels were removed from the 0.09 M $CaCl_2$ solution and moved into the different storage conditions.

6.3. *Storage methods*

The structural stability of the hydrogels after 3D bioprinting was measured using four different storage methods, including **1)** humidity chamber, **2)** freeze-drying and re-wetting, **3)** salt-water solution, and **4)** free-standing. In the humidity chamber method, at least one hydrogel from all the bioink compositions was kept in the humidity chamber of RUMED© Rubarth Apparate GmbH in the temperature of 37 ˚C and in the relative humidity of 95% for seven days. In the freeze-drying method, the hydrogels were freeze-dried in the Freezone©$^{2.5}$ from Labconco© in the vacuum conditions in the pressure of 0.700 mBar and temperature of -46 °C approximately for two days, until the frost and cold spots were completely disappeared from the outer layers of the hydrogels. These storage methods of humidity chamber and freeze-drying were adapted from Leppiniemi et al. (2017). After the freeze-drying, the hydrogels were eventually re-wetted by adding Milli-Q water and left to soak for overnight.

In the case of the salt-water solution, at least one hydrogel from all the bioink compositions was held in the salt-water solution for seven days, whereas in the free-stading method, the free-standing abilities of the hydrogels were measured by leaving them to stand on the table for 1 - 2 hours after the 3D bioprinting and cross-linking with 0.09 M $CaCl_2$. The composition of the salt-water solution has been described in more detail in the Subchapter 2.3. All the hydrogels from different storage methods were photographed and the dimensions were measured with a ruler before and after the storaging. This was followed by the evaluation of the structural changes, which is described in the Chapter 3. The different instruments utilized are also summarized in the Figure 18 below.

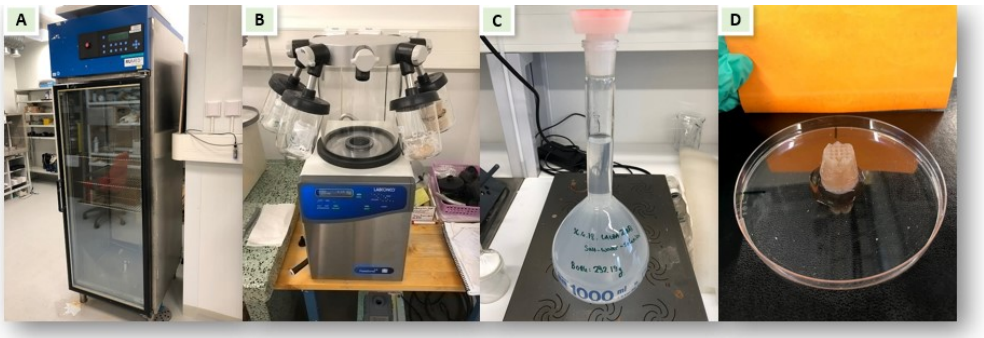

Figure 18. **A.** Humidity chamber of RUMED© Rubarth Apparate GmbH. **B.** Freezone©$^{2.5}$ from Labconco©. **C.** Salt-water solution. **D.** A hydrogel exposed to room air.

6.4. Dynamic mechanical analysis (DMA)

The compression measurements of the 3D bioprinted hydrogels were conducted using the DMA – TA Instrument Q800. The compression measurements were conducted in 1 - 2 days after 3D bioprinting for the fresh, 3D bioprinted hydrogels and for the freeze-dried and re-wetted hydrogels. Before the DMA analysis, the hydrogels were rinsed with water to remove the excess cross-linking solution and cut by knife to reduce the hydrogel height to 1 cm. The maximum sample height in the DMA-TA Instrument was 1 cm.

The DMA was started by calibration, which was followed by setting the parameters. In the TA Instrument Software, the mode was selected to be DMA controlled force, the test form custom, the clamp compression clamp and the sample shape a round disk. Furthermore, the dimensions of 10 mm as the hydrogel height and 15 mm as the hydrogel width were added, and the ramp force used was adjusted between 0.500 N/min and 18 N/min.

Next, the cutted hydrogels were placed into the DMA-TA instrument between the two plates using tweezers, the upper plate was prevented from moving, the furnace was closed, and the measurement was started. One measurement took approximately for 30 min. The described steps were repeated for each hydrogel, one hydrogel at a time. In addition, the parallel measurements were conducted in the

case of all the hydrogel compositions. In the Figure 19, the DMA-TA instrument and the location of the cutted hydrogels in it are presented.

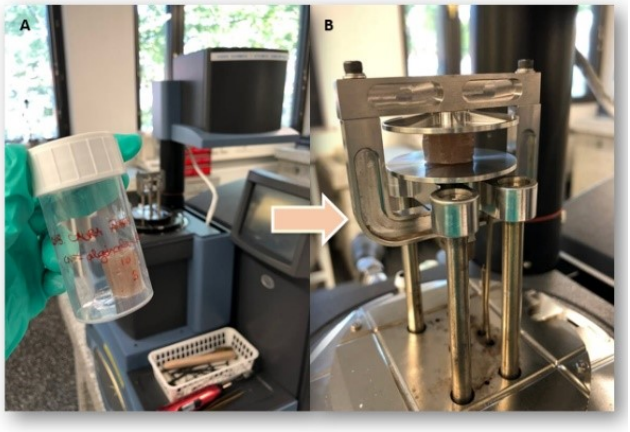

Figure 19. *The photos revealing the DMA-TA Instrument Q800 and its operation principle.* **A.** *The measured hydrogel and an overall look of the DMA-TA instrument.* **B.** *The location of the measured hydrogel (1 cm) between the plates. After the hydrogel was placed between the plates and the furnace was closed, the measurement was started.*

RESULTS AND DISCUSSION

7. Preliminary tests

Before the actual measurements were able to be started, a few preliminary tests had to be conducted. These preliminary tests considered the proper grid structure of the 3D bioprinting hydrogels, and the preparation methods of the bioinks. The used grid structure has a significant effect on the appearance, resolution, and compression strength of the 3D bioprinted hydrogels and thus, the number of pores and the type of the grid structure had to be carefully chosen. On the other hand, the effect of sonication and centrifugation as the hydrogel pretreatment methods on the properties of the bioinks and hydrogels, e.g. stability, homogeneity, viscosity, and free-standing ability, was also important to be assessed.

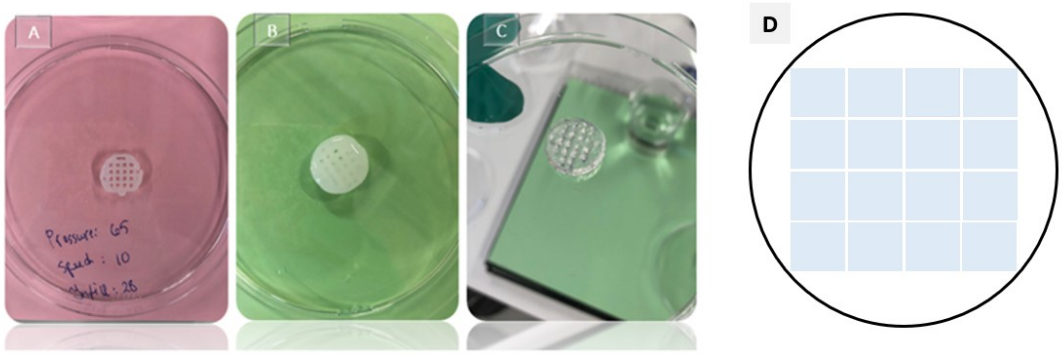

Figure 20. **A.** *Sonicated (30 minutes) CNF-alginate bioink with the Sonorex Digitec ultrasonication bath from Bandelin, and 3D bioprinted with the pressure of 65 Pa, speed 10 mms^{-1}, and infill of 28%. The photo has been taken before cross-linking with 0.09 M $CaCl_2$.* **B.** *Centrifuged CNF-alginate bioink with the speed of 4000 rpm and time of 3 minutes, and 3D bioprinted with the pressure of 50 Pa, speed 8 mms^{-1}, and infill of 28%. The photo has been taken after cross-linking with 0.09 M $CaCl_2$.* **C.** *Centrifuged T-CNF-alginate bioink with the speed of 4000 rpm and time of 3 minutes, and 3D bioprinted with the pressure of 70 Pa, speed 12.8 mms^{-1}, and infill of 28%. The photo has been taken before the cross-linking with 0.09 M $CaCl_2$.* **D.** *The appearance of the grid structure with the infill of 28%.*

To begin, in 3D bioprinting, infill is the percentage parameter that is dependent on the type of the 3D printer device, featuring the type of a grid structure, and the number of the pores in the grid. The values from 0% to 100% were available in the settings of the used BioX 3D bioprinter. In this Master's thesis, three different infill types of 25%, 28%, and 100% were tested and evaluated. Multiple tests were conducted for the sonicated and centrifuged CNF-alginate and centrifuged T-CNF-alginate bioinks.

The grid structure with the infill of 25% resulted only in four pores, whereas the grid structure with the infill of 100% contained too many small pores, which were clogged due to the swelling of the hydrogels. Both these grid structures had a negative effect on the appearance, resolution, and the compression strength of the 3D bioprinted hydrogels. However, the grid structure with the infill of 28% contained an adequate number of pores, which retained their shape well enough also after the swelling. Thus, the grid structure with the infill of 28% was decided to be used in the 3D bioprinting measurements. The participants of the grid structure tests with the best printing parameters and a schematic presentation about the grid structure with the infill of 28% can be seen in more detail in the Figure 20.

When it comes to the hydrogel pretreatment methods, it was clear from the beginning that sonication alone was unable to remove the air bubbles or increase the homogeneity of the bioinks. The sonication times of 15 minutes, 30 minutes, 50 minutes, and 1 hour and 30 minutes were tested. 15 minutes was too short a time, whereas after 50 minutes of continuous sonication, the bioinks easily burned, which also decreased their printability. In the case of the T-CNF, sonication as a pretreatment method was not enough, and resulted in bioinks with poor printability due to abundant air bubbles, inhomogenous bioink texture, and phase separation.

Due to the poor performance of sonication, centrifugation was tested to remove air bubbles and to increase homogeneity of the bioinks. The centrifugation speed of 4000 rpm and 2000 rpm and the centrifugation times of 1, 2, and 3 minutes were tested. Centrifugation clearly improved the homogeneity of the T-CNF- and CNF-based bioinks, also removing the air bubbles, and the best results were obtained when the lower speed of 2000 rpm and time of 2 minutes were used. Nevertheless, the T-CNF-based bioinks could not be used in 3D bioprinting even after centrifugation due to the resulted, undesired bioink texture, unsuitable for 3D bioprinting. Therefore, as a conclusion, the infill of 28%, centrifugation speed of 2000 rpm, and time of 3 minutes, together with regular CNF as a material option were selected for the further measurements.

8. Rheology

8.1. *Dynamic viscosity*

Dynamic viscosity measurements of the bioinks were conducted to assess their suitability to 3D bioprinting. The viscosity of the various bioinks increased as a function of increasing CLP content from 0% to 25% in the CLP-CNF-alginate bioinks (Figure 21 and Table 7). In addition, all the bioinks exhibited a shear-thinning behavior, in which the viscosity decreases with the increased shear rate, $\gamma\ (1/s)$, and shear stress, $\tau\ (Pa)$. Shear-thinning is a typical feature of hydrogels and especially of all the thixotropic CNF-based bioinks (Lê et al., 2018; Metzger, 2015).

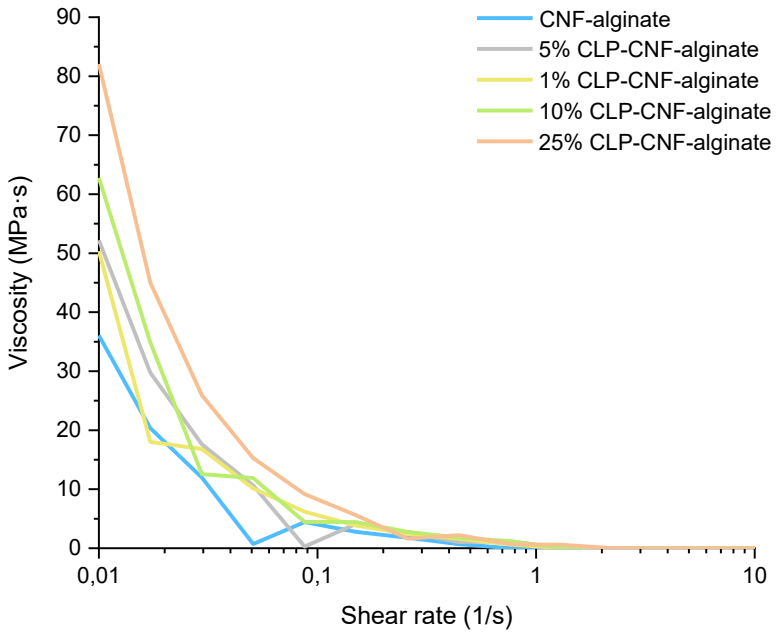

Figure 21. *Effect of CLPs on the dynamic viscosity of the CLP-CNF-alginate hydrogels. The viscosity curves obtained from the dynamic viscosity measurements of the different bioink compositions. The curves have been plotted based on the mean values of two dynamic viscosity measurements.*

Table 7. *The starting viscosities of the viscosity curves in the dynamic viscosity measurements.*

COMPOSITION	STARTING VISCOSITY (MPa·s)
CNF-ALGINATE	36.1
1% CLP-CNF-ALGINATE	52.2
5% CLP-CNF-ALGINATE	50.4
10% CLP-CNF-ALGINATE	62.8
25% CLP-CNF-ALGINATE	82.1

Nevertheless, the viscosity curves of the Figure 21, are not a faultless half parabel, mostly in the case of the bioinks of CNF-alginate, 1% CLP-CNF-alginate, 5% CLP-CNF-alginate, and 10% CLP-CNF-alginate. This can be due to the aggregates and thus inhomogeneity of the bioinks, air bubbles, problems with the bioinks, or errors during the dynamic viscosity measurements. The possible inhomogeneity and aggregation can be detected nearly in the same region with all the bioinks at lower shear rates.

Aggregates and inhomogeneity would also explain the variations in the amount of applied pressure of the same bioinks during 3D bioprinting. However, with the increased CLP concentrations of 5%, 10%, and 25%, the deviations can be detected also at higher shear rates, which can be due to the so-called dilatancy effect.

The results are reasonable, because according to Lê et al. (2018), a strong shear thinning behavior can be detected in the case of all the CNF-lignin samples. On the other hand, the use of the lignocellulosic nanofibrils, LCNF, especially with a high lignin content of 17%, improves the viscosity of the lignin- and borax-containing, CNF-reinforced polyvinyl alcohol hydrogels when compared to the pure CNF/PVA/Borax hydrogels (Bian et al. 2018). The literature findings also support the dilatancy theory. Again, according to Lê et al. (2018), the dilatancy at higher deformation were able to be detected in the case of all the CNF-lignin samples. The increase of this dynamic viscosity at higher deformation can be explained with the deformation-induced aggregation of the lower surface-charged and more flocculated and aggregated CNF suspensions containing lignin particles with glue-like properties. This reduces the freedom of movement. (Lê et al., 2018).

On the other hand, the possible differences between the dynamic viscosity data and pressure changes may also have increased due to the various bioink bottles prepared at different times for the 3D bioprinting and dynamic viscosity measurements. Another explanation is the utilization of the different parts of the bioink, containing various number of CLPs, during 3D bioprinting. According to the Figure 21, the best bioink with the least aggregates is 25% CLP-CNF-alginate bioink which experiences also only a little bit variation when it comes to the 3D bioprinting pressure.

8.2. *Amplitude sweep*

The progress of the amplitude sweep measurement is the similar one in the case of all the bioinks (Figure 22). Linear viscoelastic region (LVR) can be detected, after which the whole bioink structure is eventually destroyed, and the material properties of the bioink are turned into a more fluid-like direction. Before this, the values of G’,

are greater when compared to the values of G''. This indicates that the material measured is in a solid state, in more detail a gel-like mixture of dissolved alginate and dispersed CNF and CLPs, as expected in the case of the bioinks in the form of gel. All these results are in line with the earlier literature (Domínquez-robles et al., 2018; Metzger, 2015; Ribeiro et al., 2018).

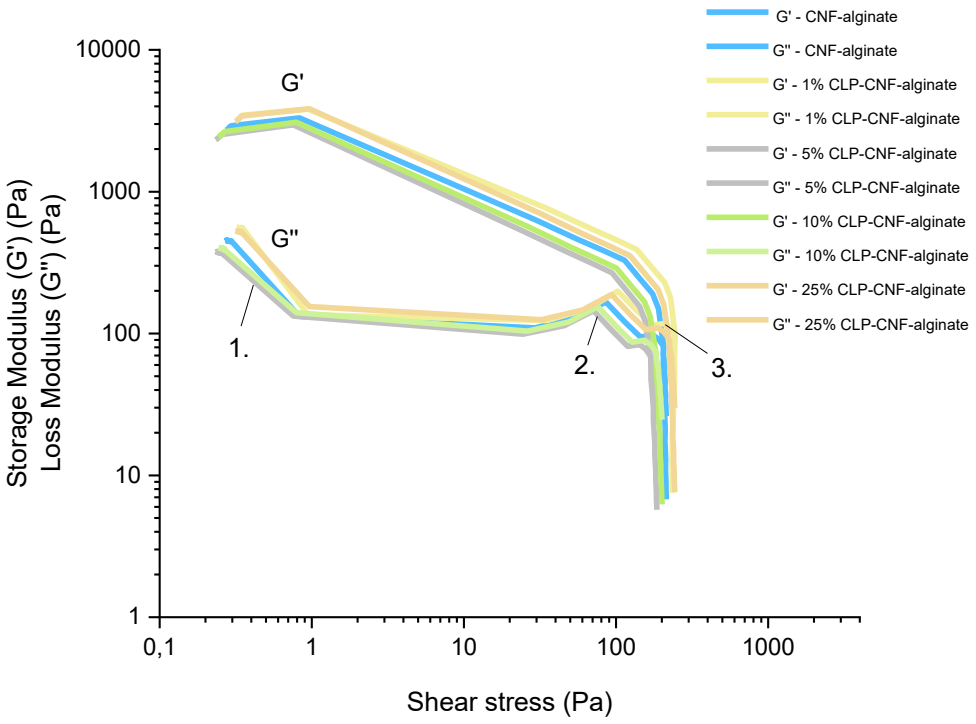

Figure 22. *Amplitude sweep curves with different CLP concentrations. The LVR, solid material type, span of critical strain (γ_c), and crossover point leading to structural destruction can be detected in the case of all the bioink compositions.* ***1.*** *LVR.* ***2.*** *The span of critical strain.* ***3.*** *Crossover point.*

Nevertheless, the unlinearity of the amplitude sweep data after the LVR is a slightly surprising outcome. It can be due to the instabilities (Ewoldt, Johnston, & Caretta, 2015), or the so-called wall slip effect in which the parallel plate cannot be in contact with the bioink in the desirable way during the measurement. Wall slip effect is a typical feature for the complex, thixotropic CNF-based materials (Lê et al., 2018). However, the measurements were repeated with the parallel plates with the rougher surface, which should restrict the wall slip effect (Ewoldt, Johnston, & Caretta, 2015), and the amount of air flow was restricted during the measurement using a plastic shield. In addition, bioinks which were less exposed to air were tested. Another

method would have been to add oil to the surface of the bioink to prevent the evaporation of water during the measurement, but there was not enough time for these tests.

Nevertheless, the results were the same despite the repeated experiments and the varying methods. Thus, the surprising diagonal outcome is mainly not because of drying or wall slip effect. Another reason can be the inhomogeneity and aggregates of the bioinks, which were discussed already in the previous Subchapter of 8.1 in the case of the dynamic viscosity. On the other hand, this does not make sense either, because the aggregates are arbitrary, and the bioink behavior in the amplitude sweep measurement is always similar. Thus, most probably, the diagonal direction of the bioinks is due to the inherent bioink nature.

Another explanation for the unlinear data of the bioinks is yielding and instabilities. Polymer solutions mixed with particles (suspensions) and metastable colloidal systems (e.g. gels) are considered as soft materials or yield stress fluids which face a transition between solid-like and fluid-like mechanical behavior due to the microstructural changes induced by the shear stress. This transition is called yielding. The yield state is directly associated with the existence of the plateau in quasi-steady flow curve. The flow curve is in many cases the consequence of a non-monotonic constitutive relation which can also be behind the unlinear region after the plateau LVR. This constitutive relation is difficult to be distinguished from the real slip of the sample at the wall, is unstable, and normally generates shear bandings or kinks in the data, especially in the case of G''. Furthermore, the existence of material instabilities in shear flows during solid-fluid transition of soft matter systems is still an open subject and also a challenge. (Coblas, Broboana, & Balan, 2016). Thus, yielding, instabilities, and wall slip effect up to some degree may have influenced on the results of the present work.

According to the Figure 22 and Table 11, the bioink of 1% CLP-CNF-alginate seems to resist the applied shear the most and thus, has the highest storage modulus indicating rigidity, before the bioink structure is completely broken up. With the increased CLP

concentrations, the resistance against shear stress first decreases remarkably, followed by the sudden increase in the case of the bioink of 25% CLP-CNF-alginate. The bioink of 5% CLP-CNF-alginate is clearly the weakest bioink. On the other hand, this strength distribution can also be seen from the length of the LVR, as evaluated in the Table 10. Thus, with the longer LVR, the bioink lasts longer before breaking up. This outcome is also in line with the literature findings. Lê et al. (2018) prepared CNF-lignin films using lignin from different sources and various concentrations. They found out that the length of the LVR, or the span of critical strain, was higher for the films with lower residual lignin concentrations (Lê et al., 2018). The Table 15 considering the LVR together with the Table 16 evaluating the crossover points of the different bioinks can be found from the Appendix 2.

When analyzing these strength results, through experience, the hydrogels with the increased CLP concentrations look and feel tougher and are less wobbly and less prone to fall over after 3D bioprinting. Thus, it would be logical that also the bioinks' strength increases in the similar manner. On the other hand, the results are reasonable based on the following evaluation. During 3D bioprinting, the grid structure resolution of CNF-alginate hydrogel was the moderate one and increased considerably in the case of the 1% CLP-CNF-alginate hydrogel. However, when the CLP concentration was increased to 5% and 10%, the grid structure resolution suffered more often, and printing of a proper grid structure became harder and less smooth a process. On the other hand, when the CLP concentration was increased to 25%, the grid structure resolution and printing smoothness were again enhanced, and the grid structure seemed even better than in the case of the regular CNF-alginate hydrogel. Thus, the bioink strength studied in this amplitude sweep measurement is probably responsible for the grid structure resolution and even overall resolution of the 3D bioprinted hydrogels, and the easiness of printing considering resolution.

The findings from the literature support these first slightly surprising results. Lê et al. (2018) realized that the lower surface charge and higher flocculation tendency of the lignin containing samples raise the viscosity and moduli of the suspension, which

results in a stiffer gel. This was proofed by the relation of G'/G'' (Lê et al., 2018). The results of this Master's thesis are approximately in line with this article, considering the 1% CLP-CNF-alginate and 25% CLP-CNF-alginate hydrogels. Therefore, the reliability of these results of the present work need to be considered, and repetition is recommended, because only one reportable measurement data of each bioink composition was obtained despite the repetition. Other possible explanations for the results are the inhomogeneous bioinks and the propensity of CLPs not to absorb as large quantities of water as CNF fibres or alginate.

Elsewhere, Domínguez-robles et al. (2018) showed a clear tendency indicating that hydrogels that absorb a higher amount of water experience a lower storage modulus. According to the re-wetting results, which will be studied more thoroughly in the Subchapter 10.2, 1% CLP-CNF-alginate hydrogel with the highest bioink strength absorbed water the least, whereas 5% CLP-CNF-alginate with the lowest bioink strength and 10% CLP-CNF-alginate hydrogels absorbed water the most. According to this interpretation, the obtained results are reasonable.

9. 3D bioprinting

The earlier confirmed parameters of infill and speed in the Chapter 7 are used in this section. Therefore, these parameters were kept constant during 3D bioprinting, but the pressure needed to be changed to obtain the best structure for the hydrogels. Similar approach of changing pressure while keeping other parameters constant was also used by Shao et al. (2015) who 3D bioprinted MFC and LS containing hydrogels.

When observing the values of pressure, which gave the best results during 3D bioprinting, between different hydrogel compositions, a clear increase in the pressure with increasing CLP content can be seen. This outcome is the expected one, because experience and dynamic viscosity measurements have shown that the addition of CLPs should increase the viscosity and thus also the amount of used pressure. Some variations in the pressure values occurred in the case of the CNF-alginate and 5% CLP-CNF-alginate bioinks, whereas the bioinks containing other CLP

concentrations showed only two pressure values. The reason for this change in pressure can be, e.g., the propensity of the CNF-lignin material combination to cause flocculation and aggregation (Lê et al., 2018), and differences in the CLP distribution in the bioinks, as already evaluated in the Subchapter 8.1. The 3D bioprinting parameters and their studies are summed up in the Table 8.

Table 8. 3D bioprinting parameters in the case of the different bioink compositions.

MATERIALS	INFILL (%)	BEST PRESSURE (Pa)	AVERAGE PRESSURE (Pa)	SPEED (mms^{-1})
CNF-ALGINATE	28	**22**	23	11.5
1% CLP-CNF-ALGINATE	28	**29**	32.5	11.5
5% CLP-CNF-ALGINATE	28	**32**	30.4	11.5
10% CLP-CNF ALGINATE	28	**26**	28	11.5
25% CLP-CNF-ALGINATE	28	**35**	33.5	11.5

When evaluating the visual and experimental observations of the 3D bioprinted hydrogels, the hydrogels seem to become stronger and stiffer with the enhanced resolution, when the CLP concentration increases. Resolution means the high hydrogel surface fidelity, in which the different layers of the hydrogel and the pores of the grid structure can accurately be detected. Furthermore, the colour of the hydrogels change into more brown-like direction. The hydrogels of CNF-alginate and 1% CLP-CNF-alginate are very similar with each other, wobbly, soft, and prone to collapse when touched or moved after 3D bioprinting. The bionks of these hydrogels are harder to handle, and air bubbles exist more easily than in the case of the bioinks with the higher CLP concentrations. However, the grid structure is easier to make with the 1% CLP-CNF-alginate hydrogel than with the 5% CLP-CNF-alginate and 10% CLP-CNF-alginate hydrogels. The best results are obtained with the bioinks with the CLP concentration of 25%. The appearance of the different 3D bioprinted hydrogels and the effect of the increased CLP concentration can be seen more thoroughly in the Figure 23, and photos considering 3D bioprinting repeatability in the Figure 24.

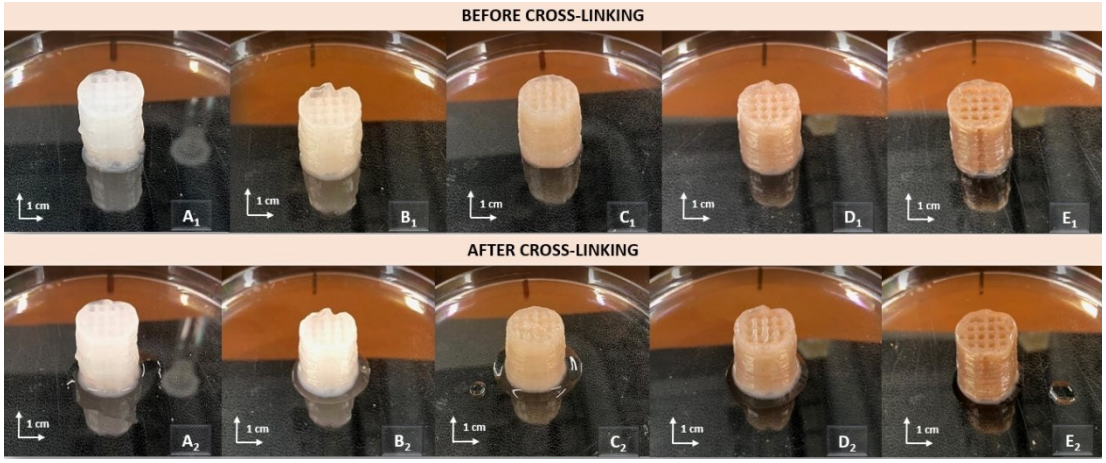

Figure 23. *Photos of printed samples with various hydrogel compositions before and after cross-linking. The scale bar in the lower right corner refers to the marking on the petri dish. The length of that line is 1 cm.* **A_1.** *CNF-alginate before cross-linking.* **A_2.** *CNF-alginate after cross-linking.* **B_1.** *1% CLP-CNF-alginate before cross-linking.* **B_2.** *1% CLP-CNF-alginate after cross-linking.* **C_1.** *5% CLP-CNF-alginate before cross-linking.* **C_2.** *5% CLP-CNF-alginate after cross-linking.* **D_1.** *10% CLP-CNF-alginate before cross-linking.* **D_2**. *10% CLP-CNF-alginate after cross-linking.* **E_1.** *25% CLP-CNF-alginate before cross-linking.* **E_2.** *25% CLP-CNF-alginate after cross-linking.*

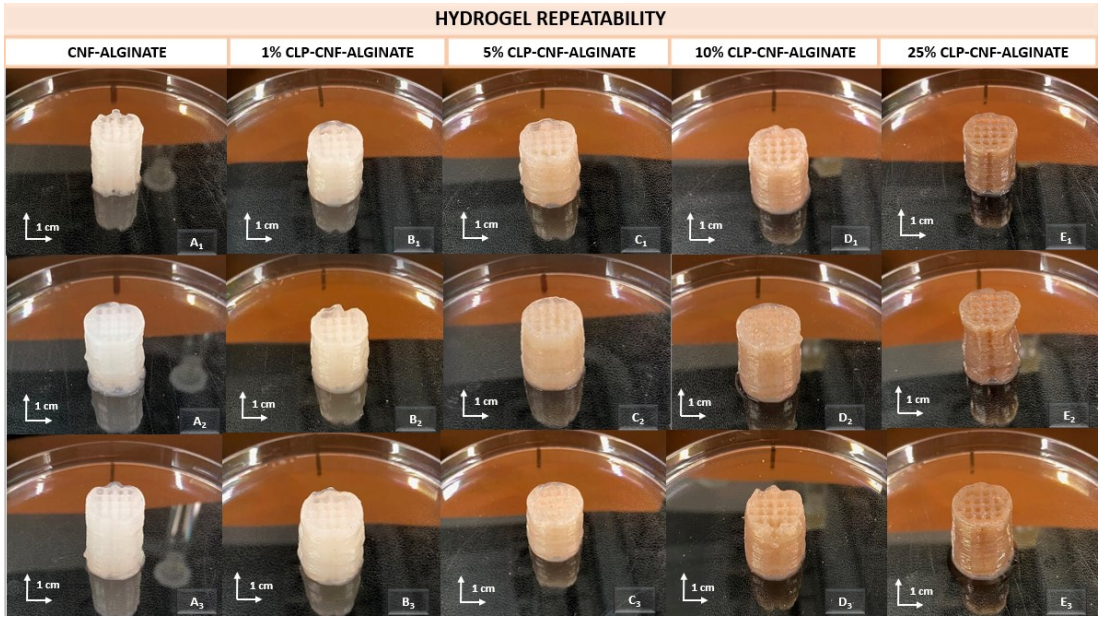

Figure 24. *Photos considering the 3D bioprinting repeatability of the hydrogels with various compositions. The scale bar in the lower right corner refers to the marking on the petri dish. The length of that line is 1 cm.* **A_1.** *CNF-alginate hydrogel number 1.* **A_2.** *CNF-alginate hydrogel number 2.* **A_3.** *CNF-alginate hydrogel number 3.* **B_1.** *1% CLP-CNF-alginate hydrogel number 1.* **B_2.** *1% CLP-CNF-alginate number 2.* **B_3.** *1% CLP-CNF-alginate hydrogel number 3.* **C_1.** *5% CLP-CNF-alginate hydrogel number 1.* **C_2.** *5% CLP-CNF-alginate hydrogel number 2.* **C_3.** *5% CLP-CNF-alginate hydrogel number 3.* **D_1.** *10% CLP-CNF-alginate hydrogel number 1.* **D_2.** *10% CLP-CNF-alginate hydrogel number 2.* **D_3.** *10% CLP-CNF-alginate hydrogel number 3.* **E_1.** *25% CLP-CNF-alginate hydrogel number 1.* **E_2.** *25% CLP-CNF-alginate hydrogel number 2.* **E_3.** *25% CLP-CNF-alginate hydrogel number 3.*

As it can be seen from the Figure 24, the repeatability of the CLP-CNF-alginate hydrogels with different CLP concentrations is very good. The shape is well retained during and after 3D bioprinting, the grid structure is easy to make, and it is possible to 3D bioprint a tall hydrogel structure. The repeatability considering volume is also good, especially with the CLP concentration of 25%. This can be seen in the Figure 25. However, the maximum height of the hydrogels decreases with the increased CLP concentrations. It seems that due to the increased viscosity and thickness of the CLP-CNF-alginate bioinks, probably because of the bioinks' propensity to cause agglomerates, more bioink is needed to bioprint the hydrogel with the same size when compared to the regular CNF-alginate bioink.

In the case of the regular CNF-alginate and 1% CLP-CNF-alginate, the maximum height obtained is 2.5 cm. With the increased CLP concentrations, the maximum height obtained is decreased to 2 cm. Furthermore, the maximum height was not possible to obtain in the case of all the 3D bioprinted hydrogels, due to the variations in the bioinks of the same concentration and technical malfunctions during the 3D bioprinting, such as clogging of the 3D bioprinting needle. The height of the hydrogels varied between 1.2 and 2 cm. However, the height of most of the 3D bioprinted hydrogels is around 2 cm.

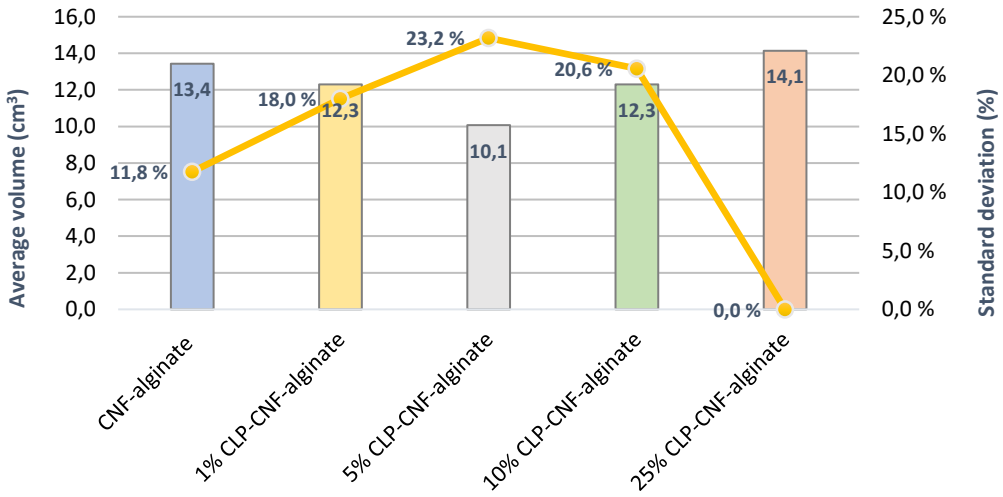

Figure 25. *The average hydrogel volumes (cm³) and standard deviations (%), revealing the hydrogel repeatability in 3D bioprinting. 4 - 5 hydrogels per each hydrogel composition was utilized. The calculations can be seen in the Appendix 4.*

The combination of the CNF-alginate bioink with the increased CLP concentrations systematically improved the printability and shape stability during and after 3D bioprinting. In addition, all the CLP containing hydrogels held their pristine geometry after the bioprinting. This outcome is most probably due to the nanoscale size of the CNF and CLPs and the existence of alginate which increases the viscosity of the bioinks and forms physical cross-links between the CNF fibres. According to Hossen et al. (2018), cross-linking between methacrylate groups provided structural stability for the CNF-MetCMC gels in the aqueous environment. The effect of cross-linking can also be the situation in the case of the CNF fibres and alginate. This effect of cross-linking with $CaCl_2$ can be seen more thoroughly in the Figure 26 below.

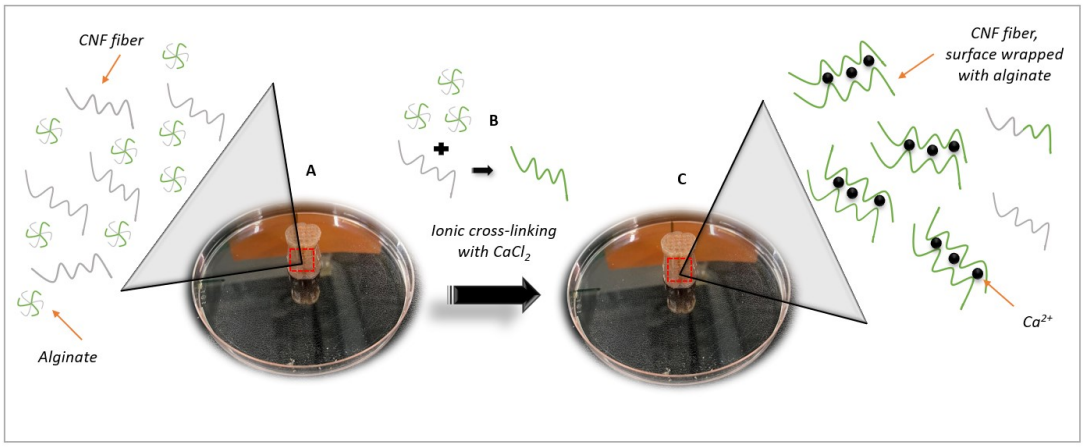

Figure 26. *A schematic presentation (not drawn to scale) about the effect of cross-linking with $CaCl_2$ on the molecular level.* **A.** *Before cross-linking, the dispersion contains separate CNF fibres and soluble alginate.* **B.** *Soluble alginate is wrapped around the surface of the CNF fibres.* **C.** *After cross-linking, Ca^{2+} ions have formed physical cross-links with alginate covering the surface of the CNF fibres.*

The high hydrogel resolution observed is most probably interlocked with the increased CLP concentration and bioink strength. This can especially be seen in the case of the 25% CLP-CNF-alginate and 1% CLP-CNF-alginate hydrogel. As shown in the Figure 24, the grid structure resolution was good in the case of the CNF-alginate hydrogel, improved with the 1% CLP-CNF-alginate hydrogel, and as good or even better in the case of the 25% CLP-CNF-alginate hydrogel. Therefore, the observation of the best resolution in the case of the 25% CLP-CNF-alginate hydrogel is probably due to the high mechanical strength, discussed in more detail in the Chapter 11,

combined with the high bioink strength. Therefore, in general, the results with these 3D bioprinted CNF-alginate and CLP-CNF-alginate hydrogels are reasonable.

On the other hand, according to Vedadghavami et al. (2017), the mechanical properties of the hydrogels have been increased with nanoparticles and the use of nanoparticles has increased for example the compression strength of the hydrogels even to 90%. Elsewhere, Raschip et al. (2013) manufactured xanthan/lignin hydrogels with higher stability due to the incorporation of lignin, using epichlorohydrin as a cross-linking agent in an alkaline medium with different types of lignin. Further, Si et al. (2017) prepared cellular-structured nanofibrous hydrogels (NFHs) by combining alginate and flexible SiO_2 nanofibres, in which the fragile appearance and shrinking during cross-linking due to water absorption of the CNF-alginate hydrogels was avoided by the addition of SiO_2 nanofibres. SiO_2 nanofibres supported the hydrogels and prevented them from collapsing (Si et al., 2017). Last but not least, lignin also makes wood fibres stiff and strong, acting like a glu between the individual fibres (Reeb, 1998). Therefore, in the case of the CLP-CNF-alginate hydrogels, it is reasonable that the addition of lignin increases the stability and the feel of stiffness and toughness and decreases the wobbliness of the hydrogels, preventing them from collapsing when moved. These results are important because the material combination of CLP-CNF-alginate have not been tested before for 3D bioprinting, no earlier studies are available, and a few studies combining different type of lignin with nanocellulose have shown undesired results.

10. Structural rigidity in various environments

10.1. *Structure retention in freeze-drying*

After 3D bioprinting, various bioprinted hydrogels were moved into the different storage conditions. The results from the freeze-drying process are first evaluated. It can be seen from the photos in the Figure 27, that all the hydrogels, from the CNF-alginate to the CLP-CNF-alginate hydrogels with the different CLP concentrations, significantly shrank due to the freeze-drying process. The surface of the freeze-dried

hydrogels appeared very jagged and rough when compared to the hydrogels before the freeze-drying process. The most jagged hydrogel is the CNF-alginate, in which small parts of the surface are even peeling off when touched. The roughness of the surface decreased when the CLP concentration increased. With the CLP concentration of 25%, the surface became more homogenous.

The feel of stiffness and toughness increased with the increased CLP concentrations. For example, the CNF-alginate hydrogel seemed very fragile when handled. On the other hand, the hydrogels with the CLP concentrations of 10% and 25% appeared tougher and even stiffer and did not deteoriate when pressed with fingers. On the other hand, the initial shape of the hydrogels seemed to last differently during freeze-drying with the different hydrogel compositions. The CNF-alginate and 25% CLP-CNF-alginate hydrogels resembled more their initial versions when compared to the other freeze-dried hydrogels. According to the photos, the shape of the hydrogels changed the most at CLP concentrations of 5% and 10%. The appearance, shrinking behavior, and possible dimensional changes of the hydrogels can be seen in more detail in the Figure 27 below.

In the case of the dimensional changes, it can be seen from the percentage data in the Figure 28 that with the smaller CLP concentrations of 1% and 5%, hydrogels shrank the least both in the longitudinal and lateral direction. The smallest changes occured with the hydrogel at 5% concentration of CLPs. On the other hand, hydrogels shrank the most with the higher CLP concentrations of 10% and 25%. The biggest changes in dimensions occurred with 10% CLPs. The shrinking behavior of the CNF-alginate was between the lower CLP concentrations of 1% and 5% and the highest CLP concentrations of 10% and 25%. Thus, it can be said that CLPs have an influence on the shrinking behavior of the hydrogels when it comes to the dimensional stability. The hydrogels with the highest CLP concentrations shrink more when compared to the hydrogels with the lower CLP concentrations.

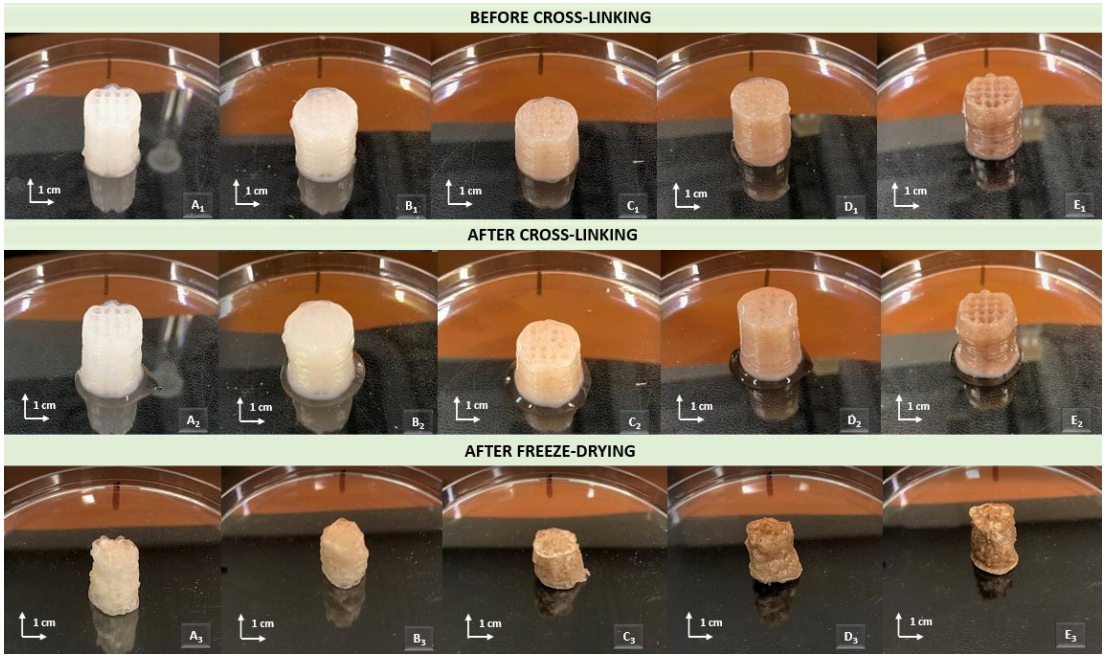

Figure 27. *Photos considering the different hydrogels with various hydrogel compositions before and after freeze-drying. The scale bar in the lower right corner refers to the marking on the petri dish. The length of that line is 1 cm.* **A_1.** *CNF-alginate hydrogel before cross-linking with 0.09 M $CaCl_2$.* **A_2.** *CNF-alginate hydrogel after cross-linking.* **A_3.** *CNF-alginate hydrogel after freeze-drying.* **B_1.** *1% CLP-CNF-alginate hydrogel before cross-linking.* **B_2.** *1% CLP-CNF-alginate hydrogel after cross-linking.* **B_3.** *1% CLP-CNF-alginate hydrogel after freeze-drying.* **C_1.** *5% CLP-CNF-alginate hydrogel before cross-linking.* **C_2.** *5% CLP-CNF-alginate hydrogel after cross-linking.* **C_3.** *5% CLP-CNF-alginate hydrogel after freeze-drying.* **D_1.** *10% CLP-CNF-alginate hydrogel before cross-linking.* **D_2.** *10% CLP-CNF-alginate hydrogel after cross-linking.* **D_3.** *10% CLP-CNF-alginate hydrogel after freeze-drying.* **E_1.** *25% CLP-CNF-alginate hydrogel before cross-linking.* **E_2.** *25% CLP-CNF-alginate hydrogel after cross-linking.* **E_3.** *25% CLP-CNF-alginate hydrogel after freeze-drying.*

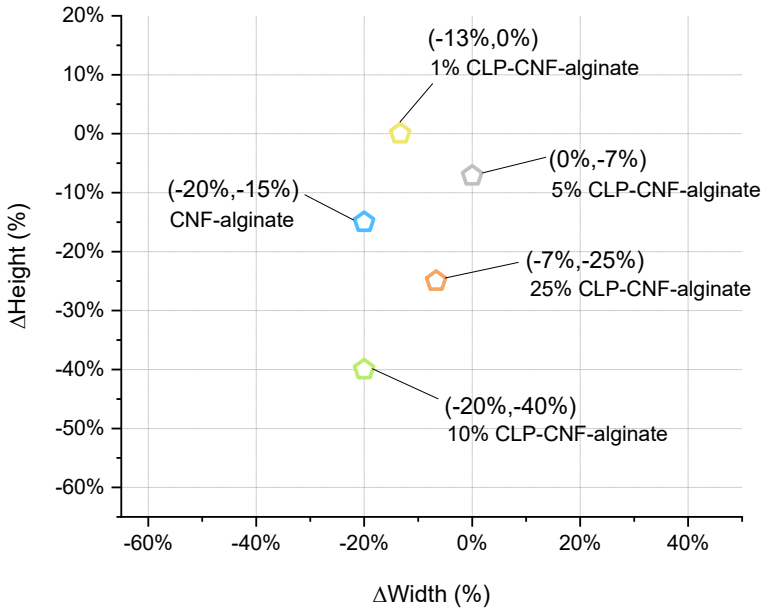

Figure 28. *The overall longitudinal and lateral dimensional changes of the hydrogels in the form of percentages (%), when the freeze-dried hydrogels were compared to the ones directly after 3D bioprinting.*

The shrinking behavior observed in the current work with CLP-CNF-alginate hydrogels is reasonable. Passauer, Fischer, & Liebner (2011) studied lignin hydrogels with moderate shrinking properties, which indicates that one feature of the lignin-based hydrogels is clearly shrinking. Furthermore, lignin naturally regulates shrinking behavior of wood. When shrinking occurs in the natural wood, water escapes between the microfibrils, containing cellulose and hemicellulose molecules (Reeb, 1998). As water leaves, the microfibrils come closer together and thus, shrinking occurs mainly in the lateral direction (Reeb, 1998), in more detail, in the tangential or radial direction (Bonarski, Kifetew, & Olek, 2015). Tangential shrinkage is usually 1.5 – 2.5 times that of the radial shrinkage (Bonarski, Kifetew, & Olek, 2015). Longitudinal shrinkage also occurs, but it is usually very small, only from 0.1 % to 0.2% (Bonarski, Kifetew, & Olek, 2015; Reeb, 1998).

In the basic level, long CNF fibres give strength to the structure, whereas alginate offers, among other things, increased swelling properties and CLPs act, e.g., as solid particles also giving strength to the gel. Nevertheless, the major difference in the shrinking behavior of the CLP-CNF-alginate hydrogels, when compared to the natural wood, is the more pronounced shrinking of these hydrogels also in the longitudinal direction with the increased CLP concentrations. This phenomenon must be related to the nano-size of the CNF and CLPs and the non-organized structure of the hydrogels in comparison to natural wood.

This theory could be reasonable, because according to Stocco et al. (2018), the degree of attachment of modulatory molecules is greater along the surfaces of the nanofibrous substrates than along flat surfaces. Thus, having densely packed specific molecules along the nanofibrous periphery is possible. Furthermore, the nano-size of the CLPs increases the number of attached particles and the influence of them. This theory would also be in line with the increased stiffness of the CLP-CNF-alginate hydrogels with the increased CLP concentrations.

More evidence can also be found from the literature to support these inferences. SEM images of the freeze-dried NFC aerogels revealed that at higher lignin

concentrations, the surface of the fibrils are rougher with the coarse, globular lignin particles (Lê et al., 2018). Lê et al. (2018) also stated that even if the lignin nanoparticles adsorb on the surface, some of the particles can also be found from the surroundings. Evidence can also be found considering the type of interactions between the CNF fibres and CLPs, and, on the other hand, between the individual CLPs. These interactions could be based on the hydrogen bonds between the CNF fibres and phenolic and aliphatic hydroxyl groups of lignin, as suggested by Jayaramudu et al. (2019), who studied the interactions of the CNF films and combined PEO and lignin material (PEO-L), based on the FTIR observations.

On the other hand, according to the ^{13}C and ^{31}P NMR spectroscopy measurements performed by Sipponen et al. (2018), softwood kraft lignin (SKL) contains approximately 0.74 mmol/g conjugated or non-conjugated carboxylic acid groups which most probably interact with CNF fibres. Nevertheless, in SKL, hydroxyl groups are the most predominant ones, with phenolic hydroxyl groups being the most abundant (Sipponen, et al. 2018). This is most probably the case also with the CLPs. In the Figure 29 below, a schema about the possible electrostatic interactions between CNF fibres and CLPs can be seen, whereas in the Figure 30, the interactions between CLPs and alginate after cross-linking with 0.09 M $CaCl_2$ have been presented.

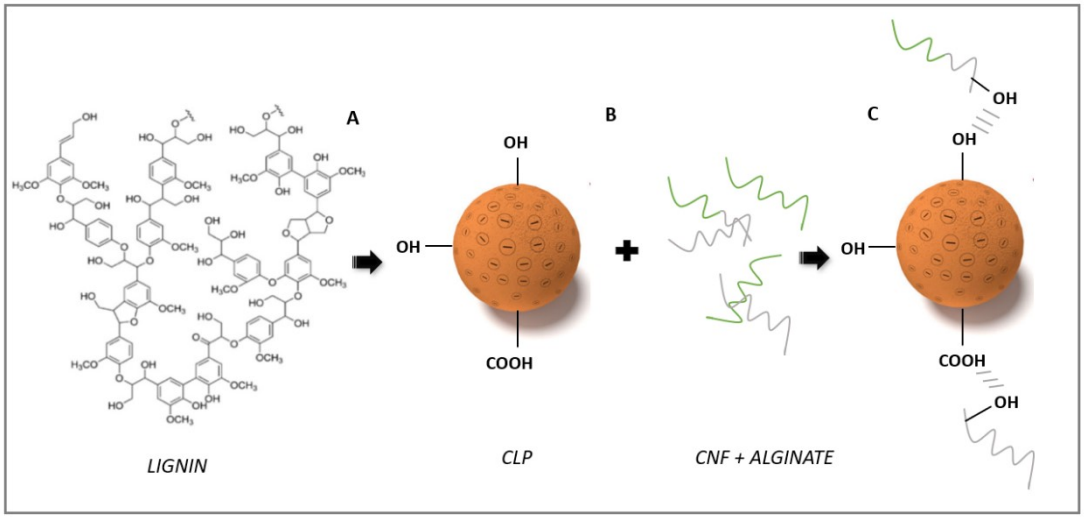

Figure 29. *The scheme (not drawn to scale) about the possible interactions between the CNF fibres and CLPs.* **A.** *The chemical structure of lignin.* **B.** *The chemical structure of CLP, together with the pure CNF fibres and CNF fibres completely or partially surface wrapped with alginate.* ***C.*** *The hydrogen bonds between the hydroxyl and carbxylic*

acid groups of the CLPs and hydroxyl groups of the pure CNF fibres and CNF fibres partially surface wrapped with alginate. (Adapted from Domínguez-robles et al. (2018) and Sipponen et al. (2018)).

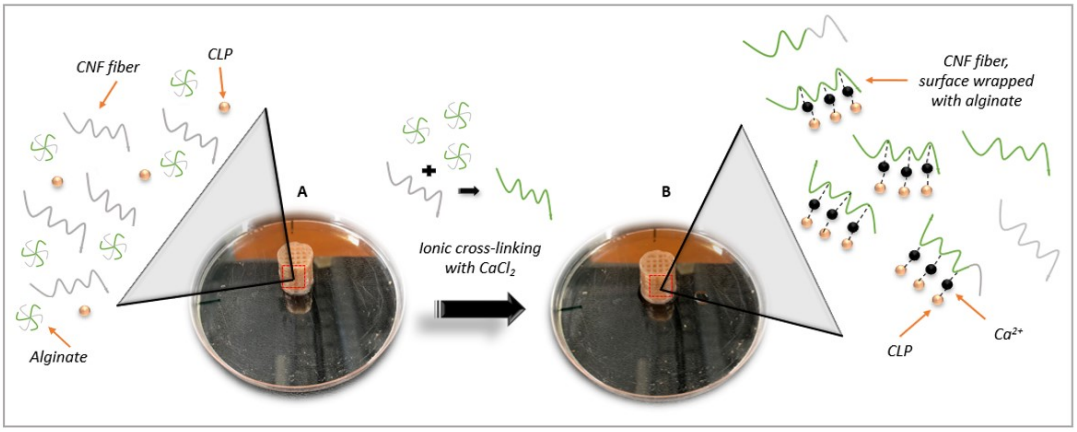

Figure 30. *The scheme (not drawn to scale) about the cross-linking of CNF fibres, completely or partially surface wrapped with alginate, and CLPs with 0.09 M $CaCl_2$.* **A.** *CNF fibres, together with the soluble alginate and CLPs, before cross-linking with 0.09 M $CaCl_2$.* **B.** *CNF fibres, completely or partially surface wrapped with alginate, form physical cross-links with CLPs with the aid of Ca^{2+} ion.*

Therefore, it is prominent that at the lower CLP concentrations, CLPs exist at small amounts both in between and on the surface of the CNF fibres, disturbing the natural, interfibrillar CNF bonds and restricting the fibres getting closer to each other. This, in turn, decreases the shrinking. However, at the higher CLP concentrations, the number of the CLPs on the surface of the CNF fibres increases, covering the surface more thoroughly, and more hydrogen bonds between the CNF fibres and CLPs and cross-links between the CLPs and alginate are formed, balancing the initial, disturbed hydrogen bonds. Furthermore, the non-bound CLPs between the fibres may allow an increase in the water absorption into spaces (pores) between the CNF fibres, giving more space for the hydrogel structure to swell and, oppositely, shrink. Therefore, the increased amount of bound and non-bound CLPs, different bonds, the existence of pores, and the nano-size of the CLPs enhance the shrinking behavior and absorbency of the CLP-CNF-alginate hydrogels.

10.2. *Water absorption in re-wetting*

When looking at the Figure 31 below and analyzing the appearance of the hydrogels based on the photos, it can be stated that the hydrogels of the CNF-alginate, 10%

CLP-CNF-alginate, and 25% CLP-CNF-alginate have retained their initial shape the best. In addition, it seems that they have absorbed water the most, which can be seen from their surface. The surface of the hydrogels does not seem as dry and fragile as in the case of the hydrogels with the CLP concentrations of 1% and 5% when they are compared to their initial, freeze-dried hydrogels.

However, the exact dimensional changes are slighly difficult to interpret only from the photos. The CNF-alginate hydrogel has clearly absorbed water and swollen, the 10% and 25% CLP-CNF-alginate hydrogels have absorbed some amounts of water and faced dimensional changes, whereas the width of the hydrogel of 5% CLP-CNF-alginate has considerable decreased. After the re-wetting, the hydrogels became softer and moist, but still tougher when compared to the initial hydrogels before freeze-drying. The feel of toughness and stiffness increased with the increased CLP concentrations even with the re-wetted hydrogels.

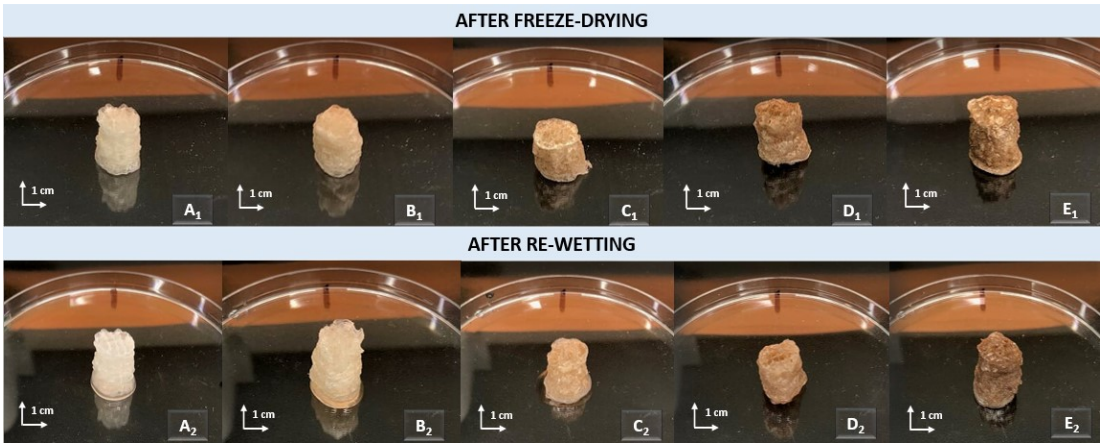

Figure 31. *The photos revealing the different hydrogels with various hydrogel compositions before and after re-wetting. The scale bar in the lower right corner refers to the marking on the petri dish. The length of that line is 1 cm.* **A_1.** *CNF-alginate hydrogel after freeze-drying.* **A_2.** *CNF-alginate hydrogel after re-wetting.* **B_1.** *1% CLP-CNF-alginate hydrogel after freeze-drying.* **B_2.** *1% CLP-CNF-alginate hydrogel after re-wetting.* **C_1.** *5% CLP-CNF-alginate hydrogel after freeze-drying.* **C_2.** *5% CLP-CNF-alginate hydrogel after re-wetting.* **D_1.** *10% CLP-CNF-alginate hydrogel after freeze-drying.* **D_2.** *10% CLP-CNF-alginate hydrogel after re-wetting.* **E_1.** *25% CLP-CNF-alginate hydrogel after freeze-drying.* **E_2.** *25% CLP-CNF-alginate hydrogel after re-wetting.*

The studies considering the dimensional changes are in line with the interpretations made based on the hydrogel photos. The Figure 32 below reveals that the hydrogels with the highest CLP concentrations of 10% and 25% had swollen the most, nearly

reaching the initial dimensions of these hydrogels. In contrast, the length or width of the hydrogels with the lowest CLP concentrations of 1% and 5% had sligthly decreased. In general, the hydrogels with the CLP concentrations of 1% and 5%, which shrank the least, also showed the lowest extent of water uptake, and the hydrogels with the CLP concentrations of 10% and 25%, which shrank the most, absorbed most water and thus swelled the most. The best performance can be seen in the case of the 10% CLP-CNF-alginate hydrogel, which swelled back to its initial dimensions after the freeze-drying and re-wetting. In the Figure 32, the dimensional changes of the various hydrogels can be observed in detail.

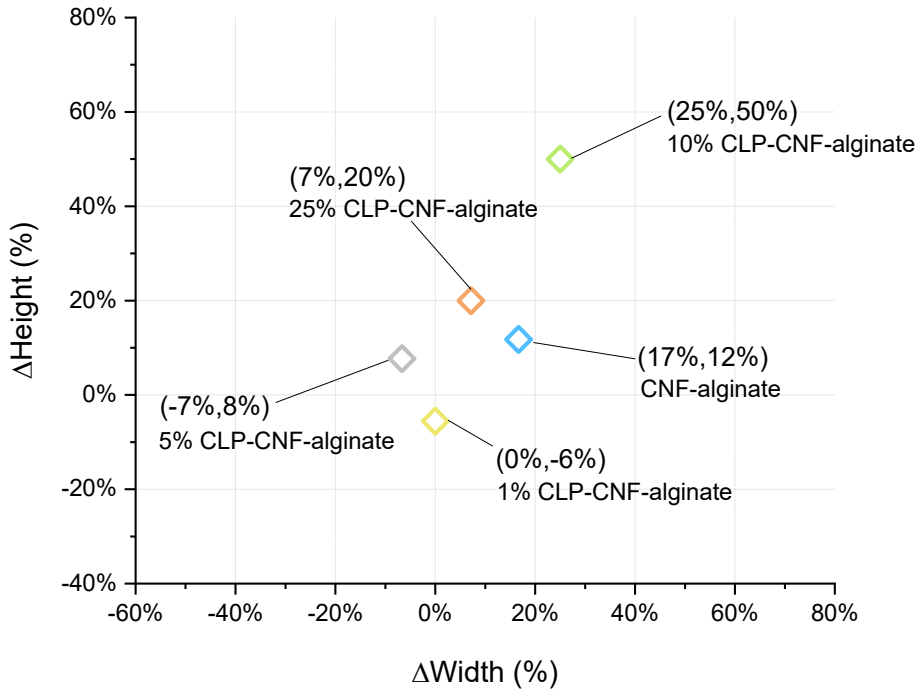

Figure 32. *The overall longitudinal and lateral dimensional changes of the hydrogels in the form of percentages (%), when the re-wetted hydrogels were compared to the ones directly after freeze-drying.*

According to the literature, it is evident that the addition of lignin supports the absorption and swelling capacity of the other hydrogel components, in the case of the CLP-CNF-alginate hydrogels, the capacity of CNF fibres. The addition of lignin improved the swelling behavior of porous lignin-based poly(acrylic acid) hydrogel with higher water retention, fast swelling and deswelling rates (Ma et al., 2016). On the other hand, Larrañeta et al. (2018) prepared lignin hydrogels by combining lignin with poly (ethylene glycol) and poly(methyl vinyl ether-co-maleic acid) through an

esterification reaction. The prepared hydrogels showed swelling capabilities up to 500% (Larrañeta et al., 2018). In another study, Domínguez-robles et al. (2018) prepared hydrogels by cross-linking poly(methyl vinyl ether co-maleic acid) and different technical lignins in ammonium and sodium hydroxide solutions. The resulted hydrogels experienced high water absorption capacities, ranging from 13 to 130 g of water per 1 g of sample (Domínguez-robles et al., 2018). Furthermore, Raschip, Hitruc, & Vasile (2011) prepared biodegradable and superabsorbent xanthan and lignin containing hydrogels based on cross-linking between xanthan gum and lignin, using epichlorhydrin as a cross-linking agent in the alkaline NaOH medium. The produced hydrogels were biodegradable and had, e.g., combined antimicrobial and antioxidative properties with increased biocompatibility (Figueiredo et al. 2018).

However, the process of freeze-drying has its own effect on the absorption and re-wetting capacities of the hydrogels, as described below. According to Hossen et al. (2018), the larger pore volume in the highly porous gels allows hydrogels to hold more fluid. In their article, the amount of water retained inside the 3D structure increased linearly with the increasing porosity (Hossen et al. 2018). Therefore, it is likely that the freeze-drying process and the increased number of pores improves the re-wetting properties of the CLP-CNF-alginate hydrogels, also when compared to the basic drying method through evaporating.

When taking a look at the molecular level, according to Domínguez-robles et al. (2018), the degree of swelling of the hydrogels is inversely related to the cross-linking density. Therefore, the decreased shrinking after freeze-drying and increased swelling after re-wetting with the increased CLP concentrations is not only due to the influence of the CLPs and the process of freeze-drying, but also the decrease of the hydrogen bonds between the individual CNF fibres. It can be that the increased number of CLPs adsorbed on the surface of the CNF fibres block the formation of the hydrogen bonds between the CNF fibres and the cross-links between the CNF fibres and alginate, even replacing some of the prior ones. This, in turn, enhances the absoprtion and re-wetting properties of the hydrogels. The influence of lignin on the

hydrogen bonds are also analyzed in the Chapter 10.1 considering the effect of freeze-drying process, and in the Chapter 11 about DMA of the hydrogels.

10.3. *Hydrogel stability in humidity chamber*

In this storage method, the physiological conditions inside the human body considering humidity were mimicked and their influence on the hydrogel stability were monitored, by placing the studied hydrogels in the relative humidity of 95% and temperature of 37 °C. According to the photos in the Figure 33 below, a clear decrease in the height can be detected in the case of all the hydrogels. The height decreased nearly linearly, starting from the hydrogel of the CNF-alginate, and the hydrogel of the 10% CLP-CNF-alginate shrank also in the lateral direction. On the other hand, toughness and at the same time resolution increased and the hydrogels maintained their initial shape better with the increased CLP concentrations. The shape deformation was at worst in the case of the hydrogels of the CNF-alginate, 1% CLP-CNF-alginate, and 5% CLPs-CNF-alginate. Furthermore, the resolution of the hydrogels after humidity chamber increased in the case of the CLP concentrations of 10% and 25%, when compared to their initial hydrogels, and the water vapor scraped down the rough edges of the hydrogel surfaces.

After the humidity chamber, the hydrogels appeared tougher when compared to their initial hydrogels and were rubber-like when touched. The hydrogel with the highest CLP concentration of 25% already resembled of a hard rubber and deteriorated the least when handled. When compared to the other storage methods, humidity chamber gave the best visual effects on the hydrogels, in more detail, the appearance of the hydrogels suffered the least with the increased CLP concentrations. The appearance of the various hydrogels and the possible dimensional changes can be seen in the Figure 33, and the numerical data considering the dimensional changes of the hydrogels in the Figure 34.

According to the data in the Figure 34, the humidity of 95% and temperature of 37 °C led to shrinkage in all the hydrogels. The longitudinal dimensional changes of the

hydrogels decreased by 5% when 1% of the CLPs was added to the CNF-alginate hydrogel composition. However, when the CLP concentration increased, the longitudinal dimensions of the hydrogels decreased nearly linearly. This decrease in height was also detected from the hydrogel photos. At the same time, the lateral dimensions remained essentially unchanged, except for the 25% CLP-CNF-alginate hydrogel. Despite the changes in height, the dimensional changes were generally smaller with every added CLP concentration when compared to the regular CNF-alginate hydrogel. The best results were obtained with the CLP concentration of 1% in which the dimensional changes were the smallest. In general, the humidity chamber as a storage method increased the resolution, toughness, shape stability, and rubber-like appearance, but decreased the height and, in some cases, also the width of the hydrogels. The addition of CLPs into the CNF-alginate hydrogel composition clearly improved the structure retention under 95% relative humidity conditions.

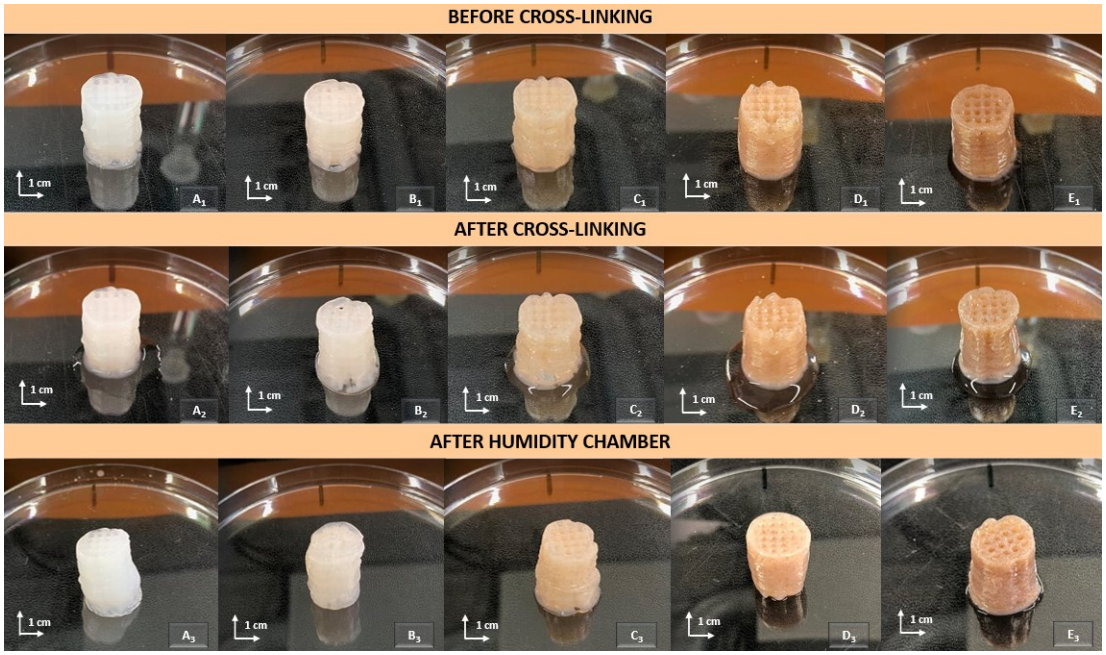

Figure 33. *The photos of hydrogels with various compositions. The scale bar in the lower right corner refers to the marking on the petri dish. The length of that line is 1 cm.* **A_1.** *CNF-alginate hydrogel before cross-linking.* **A_2.** *CNF-alginate hydrogel after cross-linking.* **A_3.** *CNF-alginate hydrogel after humidity chamber.* **B_1.** *1% CLP-CNF-alginate hydrogel before cross-linking.* **B_2.** *1% CLP-CNF-alginate hydrogel after cross-linking.* **B_3.** *1% CLP-CNF-alginate hydrogel after humidity chamber.* **C_1.** *5% CLP-CNF-alginate hydrogel before cross-linking.* **C_2.** *5% CLP-CNF-alginate hydrogel after cross-linking.* **C_3.** *5% CLP-CNF-alginate hydrogel after humidity chamber.* **D_1.** *10% CLP-CNF-alginate hydrogel before cross-linking.* **D_2.** *10% CLP-CNF-alginate hydrogel after cross-linking.* **D_3.** *10% CLP-CNF-*

alginate hydrogel after humidity chamber. **E_1.** *25% CLP-CNF-alginate hydrogel before cross-linking.* **E_2.** *25% CNF-alginate-CLPs hydrogel after cross-linking.* **E_3.** *25% CLP-CNF-alginate hydrogel after humidity chamber.*

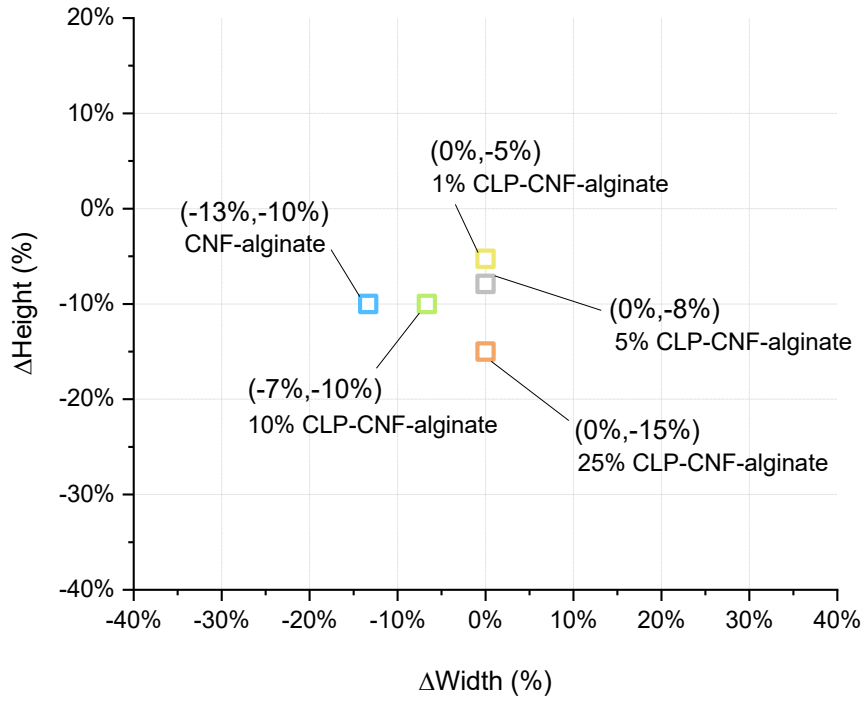

Figure 34. *The overall longitudinal and lateral dimensional changes of the hydrogels in the form of percentages (%), when the hydrogels exposed to the humidity chamber were compared to the ones directly after 3D bioprinting.*

When analyzing the reliability of these results, the following analysis is obtained. In the case of the CNF-alginate hydrogel, the height and width of the hydrogel decreased about 2 mm. It seems that the combination of alginate and CNF restricted the swelling of the hydrogel but was unable to hinder the shrinking effect. These observations are in line with the ones found in the literature. Benselfelt, Engström, & Wagberg (2018) prepared CNF-alginate networks in which alginate was able to suppress the swelling of the CNF over 95%. In addition, according to the results of Leppiniemi et al. (2017), the cross-linked CNF-alginate hydrogels, which were pre-conditioned in the room temperature, exhibited only a low extent of swelling when compared to the similar, freeze-dried hydrogel samples. Thus, the limited swelling is a reasonable effect. However, the hydrogel collapsed and showed 25% lower height compared to its initial height when kept for six days in the relative humidity of 95% and temperature of 37 ˚C (Leppiniemi et al., 2017). In the case of the measurement of this Master's thesis, the height of the CNF-alginate hydrogel decreased

approximately 10% of its initial height. Thus, the obtained results are reasonable and better when compared to the literature findings, because CLPs help to maintain the structure stability of the hydrogels.

Furthermore, Shankar, Reddy, & Rhim (2015) studied agar/lignin composite films, with the lignin concentrations of 1wt%, 3wt%, 5wt%, and 10wt%, in which the swelling ratio and moisture content was decreased with the increased lignin content, whereas Zadeh, Keefe, & Kim (2018) discovered that the addition of alkali lignin and lignosulfonate decreased the water vapor permeability of the soy protein isolate films to 50% of the control film. The strong intermolecular interactions between agar and lignin and therefore, good compatibility, increased the tortuous path for water vapor diffusion, resulting in less permeation of water molecules through the polymer film (Shankar, Reddy, & Rhim, 2015).

10.4. *Hydrogel stability in salt-water solution*

In this storage method, the hydrogels were placed in the salt-water solution, mimicking the salt composition used for the cell culture, and the structure stability of the studied hydrogels was evaluated. When observing the hydrogel photos in the Figure 35, the addition of CLPs clearly improved the shape and dimensional stability of the hydrogels in the salt-water solution. The shape of the CNF-alginate suffered the most with the small dimensional changes, but the shape and dimensions of the CLP containing hydrogels seemed nearly unchanged. In addition, the look and feel of toughness increased with the increased CLP concentrations.

However, the undesired effect of the salt-water solution on the CNF-alginate and CLP-CNF-alginate hydrogels was its disintegrating nature. The worst results were obtained in the case of the CNF-alginate hydrogel, which was close to impossible to handle due to its softness. It had also lost its shape nearly completely. With the lower CLP concentrations of 1% and 5%, the hydrogels remained soft, a small part of the surface had disintegrated, smoothing the surfaces, and the smaller defects in the hydrogel structure had enlargened.

On the other hand, with the increased CLP concentrations, the disintegrating effect of the salt-water solution got even worse. In the case of the 10% CLP-CNF-alginate and 25% CLP-CNF-alginate hydrogels, the grid structure had considerably suffered, and the surface of the hydrogels had dissolved so much that it was difficult to detect single layers. 10% CLP-CNF-alginate hydrogel had dissolved the most, resulting in the softer surface which was prone to break up when handled. In the case of the hydrogels of the 25% CLP-CNF-alginate, the grid structure was nearly impossible to detect. Colour changes was also possible to detect in the case of the hydrogels with the CLP concentrations of 10% and 25%, which is probably due to the dissolution, dispersing, and possible dissolution of CLPs caused by the salt-water solution. The dissolution of CLPs was also able to be seen from the salt-water solution which colour was turned into slightly brown after the measurement. The appearance, effect of dissolution, and possible dimensional changes of the CNF-alginate and CLP-CNF-alginate hydrogels can be observed in the Figure 35.

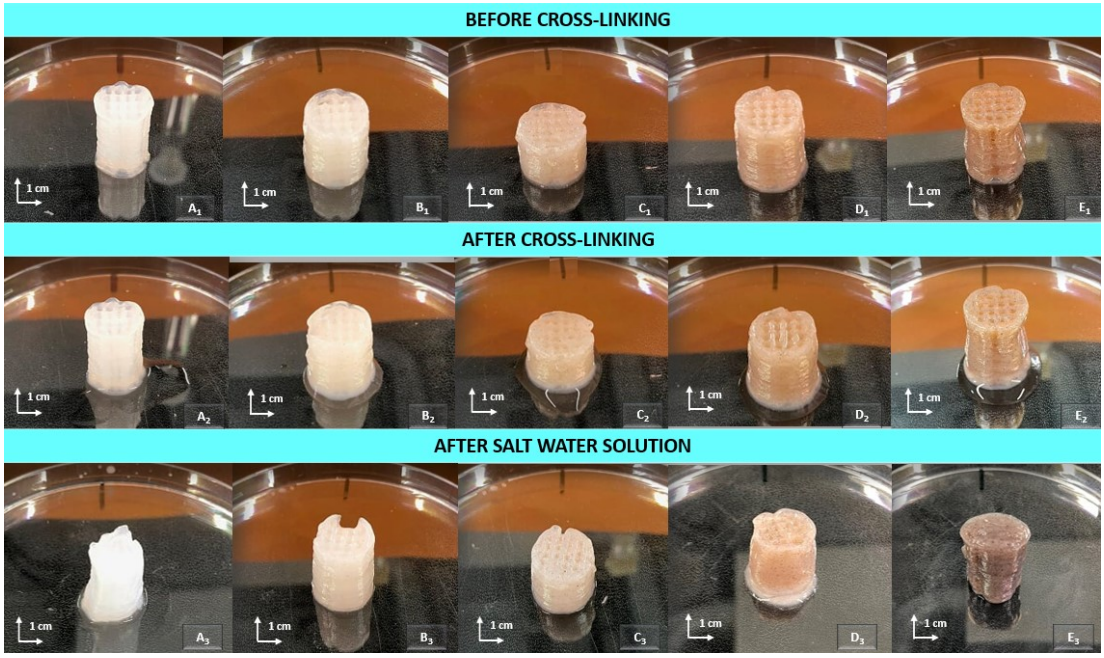

Figure 35. *The photos about the different hydrogels with various hydrogel compositions. The scale bar in the lower right corner refers to the marking on the petri dish. The length of that line is 1 cm.* **A_1.** *CLP-CNF-alginate hydrogel before cross-linking.* **A_2.** *CLP-CNF-alginate hydrogel after cross-linking.* **A_3.** *CLP-CNF-alginate hydrogel after salt-water solution.* **B_1.** *1% CLP-CNF-alginate hydrogel before cross-linking.* **B_2.** *1% CLP-CNF-alginate hydrogel after cross-linking.* **B_3.** *1% CLP-CNF-alginate hydrogel after salt-water solution.* **C_1.** *5% CLP-CNF-alginate hydrogel before cross-linking.* **C_2.** *5% CLP-CNF-alginate hydrogel after cross-linking.* **C_3.** *5% CLP-CNF-alginate hydrogel after salt-water solution.* **D_1.** *10% CLP-CNF-alginate hydrogel before cross-linking.* **D_2.** *10% CLP-CNF-alginate hydrogel*

after cross-linking. **D_3.** *10% CLP-CNF-alginate hydrogel after salt-water solution.* **E_1.** *25% CLP-CNF-alginate hydrogel before cross-linking.* **E_2.** *25% CLP-CNF-alginate hydrogel after cross-linking.* **E_3.** *25% CLP-CNF-alginate hydrogel after salt-water solution.*

When, in turn, analyzing the dimensional changes of the hydrogels, it can be seen from the data in the Figure 36 that the salt-water solution decreased the dimensions of the CNF-alginate hydrogel but did not affect on the dimensions of the hydrogels with the various CLP concentrations. The addition of CLPs clearly prevented the dimensional changes of the hydrogels when exposed to the salt-water solution. In general, these hydrogels faced the least dimensional changes after the salt-water solution storage method when compared to the other storage methods. Therefore, this storage method has the best dimensional results. In the Figure 36 below, the dimensional changes of the hydrogels can be observed in more detail.

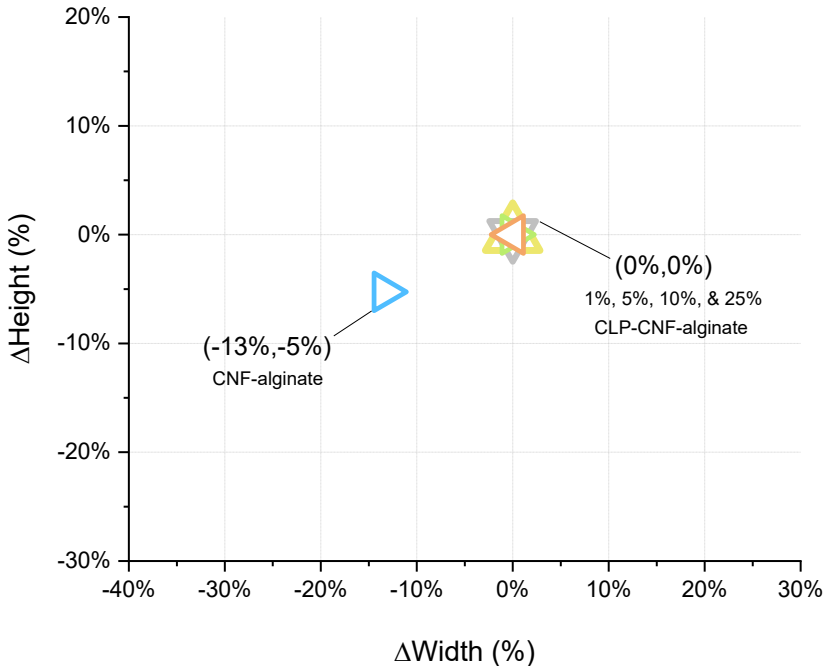

Figure 36. *The overall longitudinal and lateral dimensional changes of the hydrogels in the form of percentages (%), when the hydrogels exposed to the salt-water solution were compared to the ones directly after 3D bioprinting.*

According to Abdelwahed et al. (2006), the major problem of nanoparticle systems is their poor stability in the aqueous medium. This major obstacle restricting the use of nanoparticles is due to the physical and the chemical instability, the chemical instability considering, e.g., hydrolysis of polymer materials forming the nanoparticles, and reactivity of materials during the storage (Abdelwahed et al.,

2006). These instabilities are frequently noticed when the aqueous suspensions of nanoparticles are stored for an extended periods (Abdelwahed et al., 2006). However, at many circuimstances, CLPs are stable colloidal particles and not prone to hydrolysis reactions (Richter et al., 2016). CNF fibres are also reported to stabilise, e.g., diluted and concentrated dispersions, water-in-oil emulsions, and wet foams by forming a firm percolation fibril network (Tenhunen et al., 2018). Therefore, hydrolysis of the CLPs or CNF fibres alone should not be the case with the hydrogels of this Master's thesis.

On the other hand, other hydrogel properties and the composition of an aqueous medium has an influence on the hydrogel behavior. Kuo & Ma (2007) mentioned that instability of the ionically cross-linked hydrogels in an aqueous medium is a challenge. They found out that the hydrogel composition, when it comes to the dimensions of the Ca-alginate hydrogels, is dependent on the Ca^{+} ion concentration of the medium, cross-linking density, and polymer concentration of the gel. Shrinking or swelling occurs with too low or high Ca^{+} ion concentrations. On the other hand, also the hydrophilicity of Ca-alginate hydrogel increases the swelling behavior of this hydrogel in an aqueous medium in higher hydrogel concentrations (Kuo & Ma, 2007). Furthermore, according to Rol et al. (2018), also CNF fibres are highly hydrophilic.

Thus, it is prominent that the combination of CNF-alginate in a hydrogel react when exposed to the salt-water solution, in a way described next. In the case of the hydrogel of CNF-alginate of this present work, it can be detected, that the hydrogel height and width decreased when the hydrogel was exposed to the salt-water solution. This can be seen in the Figure 36. However, when CLPs was added to the hydrogels, the dimensional changes stopped immediately. Only some small holes in the hydrogel structure deteoriated in the salt-water solution, until the deteoriation was stopped at higher CLP concentrations. This is reasonable, because the addition of lignin decreases the swelling ratio and moisture content of the material composites and hampers the diffusion rates (Shankar, Reddy, & Rhim, 2015), therefore, increasing the shape stability, as described in the previous Subchapter 10.3. The increased shape stability is due to the increased attachment of the CLPs

onto the surface of the CNF fibres and the formation of hydrogen bonds, restricting the natural behavior of the CNF-alginate hydrogel, shrinking and swelling in the salt-water solution.

With the increased CLP concentrations, the hydrogel surface, in more detail the CLPs, started to dissolve due to the salt-water solution. This same phenomenon was faced by Lievonen et al. (2016), who utilized lignin extracted from the kraft pulping as in this Master's thesis. In their work, the CLPs started to dissolve at pH 13, resulting as a yellowish colour of the CLP dispersion (Lievonen et al., 2016). Furthermore, the CLP dispersion became unstable at 1 M NaCl, which was due to the accumulation of Na^+ counter ions around the CLPs and the consequent reduction of the thickness of the stabilising, electrical double layer, formed by CLPs (Lievonen et al., 2016). Elsewhere, also Richter et al. (2016) experienced the dissolution of CLPs and limited dispersion stability at increased pH and aqueous NaCl concentrations, when high-purity CLPs were used. Therefore, in the case of this Master's thesis, the dissolution of CLPs is not due to too high pH of the used salt-water solution, mimicking the physiological conditions inside the human body. However, the ionic concentration of, e.g., cationic sodium ions in the salt-water solution has most probably been too high for the stable CLPs. In general, according to the obtained results, CLPs are stable, colloidal particles up to certain limits in the CLP-CNF-alginate hydrogels, considering the number of CLPs in the hydrogels and the concentration of ions and the pH in the aqueous medium.

10.5. *Structure retention and drying in free-standing*

In this storage method, the hydrogels were kept on the table in the room air for the certain time, after 3D bioprinting and cross-linking with 0.09 M $CaCl_2$, to evaluate the free-standing stability of the hydrogels. When looking at the hydrogels in the Figure 37, the following observations based on these hydrogel photos and experimental observations can be made. It is rather evident that the smallest changes have occurred with the CNF-alginate hydrogel. The shape of the hydrogel and the length remained unchanged, only some slight collapsing was seen in the longitudinal

direction. In addition, drying could not be detected in the case of this reference hydrogel. Nevertheless, the addition of CLPs resulted in an increased swelling in the case of the hydrogel with the CLP concentration of 1%. This hydrogel had slightly swollen in the lateral direction.

In the case of the hydrogels with the CLP concentrations of 5% and 10%, some major drying effects could be detected, especially in the upper parts of the hydrogels and around the grid structure. Drying can be seen for example as the colour changes. These hydrogels were also crumbled up in the longitudinal direction, which was resulted in an increased width in the central area of the hydrogels. However, the overall width of the hydrogels had not increased. In the case of the hydrogel with the CLPs concentration of 25%, the hydrogel had clearly started to crumble up and even to lose its shape, but no drying could be observed yet at this point. In addition, the resolution of this hydrogel seemed better when compared to the hydrogel of the CNF alginate or 1% CLP-CNF-alginate.

The different time scale made it harder to interpret the differences between the various hydrogels. The free-standing times of the hydrogels were 1 hour and 5 minutes for the CNF-alginate hydrogel, 1 hour and 15 minutes for the 1% CLP-CNF-alginate hydrogel, 2 hours for the 5% CLP-CNF-alginate hydrogel, 1 hour and 50 minutes for the 10% CLP-CNF-alginate hydrogel, and 1 hour for the 25% CLP-CNF-alginate hydrogel. However, the hydrogels of the CNF-alginate, 1% CLP-CNF-alginate, and 25% CLP-CNF-alginate were photographed after approximately the same durations of free-standing. Thus, it can be stated that the CNF-alginate hydrogel changed the least, 1% CLP-CNF-alginate hydrogel faced increased swelling, and 25% CLP-CNF-alginate hydrogel started to lose its shape and height after approximately 1 hour of free-standing in the air. In addition, with the increased free-standing times, the hydrogels with the increased CLP concentrations dried considerably. The appearance of the hydrogels, possible dimensional changes, and effect of drying can be seen more thoroughly in the Figure 37 below, together with the dimensional changes of the hydrogels in the Figure 38.

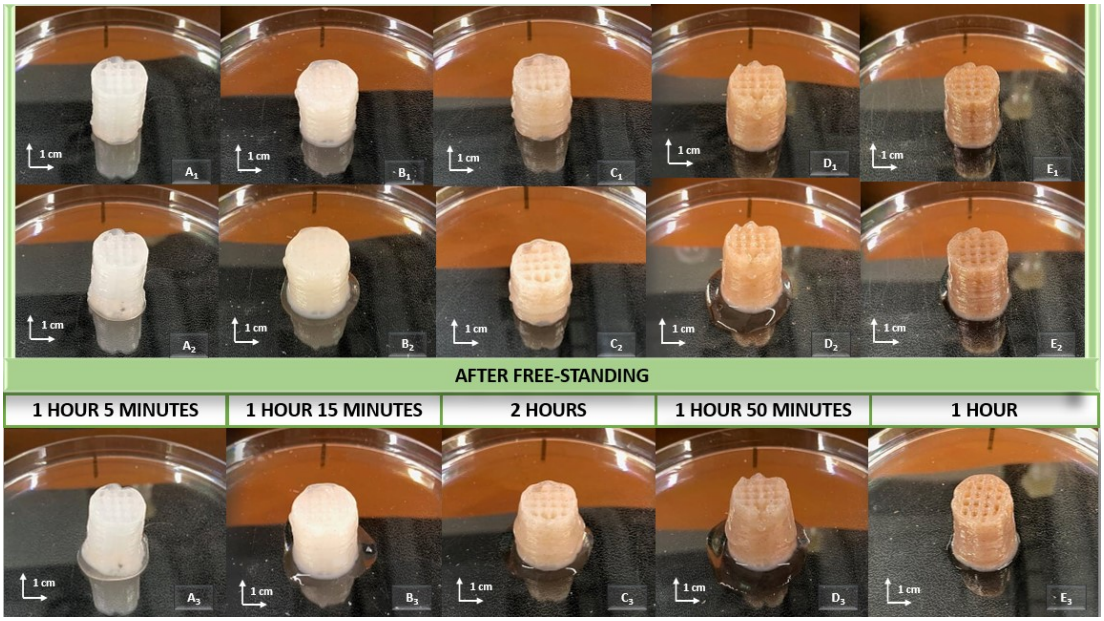

Figure 37. *The photos about free-standing measurements of different hydrogels based on various bioink compositions. The scale bar in the lower right corner refers to the marking on the petri dish. The length of that line is 1 cm.* ***A₁.*** *CNF-alginate hydrogel before cross-linking.* **A₂.** *CNF-alginate hydrogel after cross-linking.* **A₃.** *CNF-alginate hydrogel after free-standing measurement.* **B₁.** *1% CLP-CNF-alginate hydrogel before cross-linking.* **B₂.** *1% CLP-CNF-alginate hydrogel after cross-linking.* **B₃.** *1% CLP-CNF-alginate hydrogel after free-standing measurement.* **C₁.** *5% CLP-CNF-alginate hydrogel before cross-linking.* **C₂.** *5% CLP-CNF-alginate hydrogel after cross-linking.* **C₃.** *5% CLP-CNF-alginate hydrogel after free-standing measurement.* **D₁.** *10% CLP-CNF-alginate hydrogel before cross-linking.* **D₂.** *10% CLP-CNF-alginate hydrogel after cross-linking.* **D₃.** *10% CNF-alginate-CLP hydrogel after free-standing measurement.* **E₁.** *25% CLP-CNF-alginate hydrogel before cross-linking.* **E₂.** *25% CLP-CNF-alginate hydrogel after cross-linking.* **E₃.** *25% CLP-CNF-alginate hydrogel after free-standing measurement.*

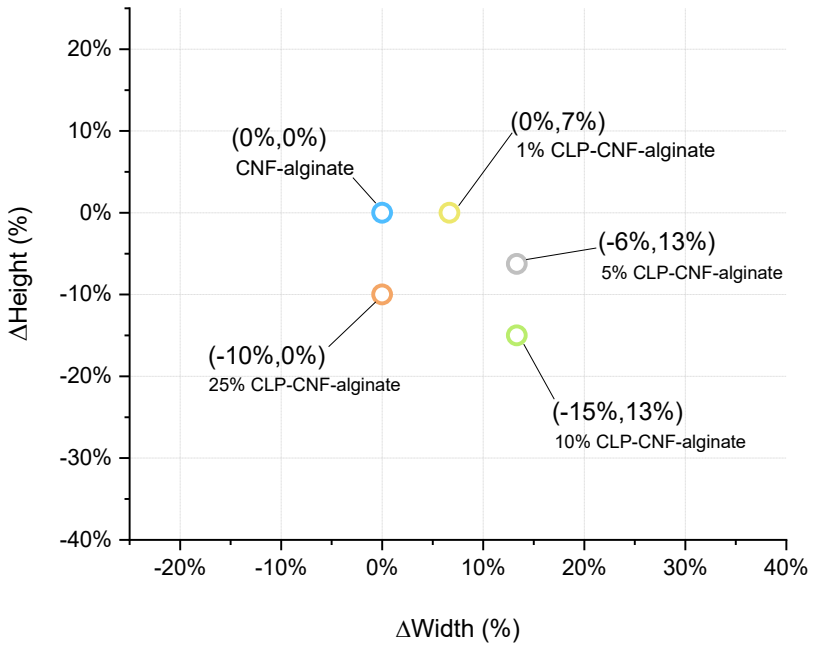

Figure 38. *The overall longitudinal and lateral dimensional changes of the hydrogels in the form of percentages (%), when the hydrogels exposed to the room air were compared to the ones directly after 3D bioprinting.*

The dimensional changes were also in line with the earlier observations based on the photos and experimental perceptions. According to the Figure 38 above, the most prominent dimensional changes occured with the hydrogels with the CLP concentrations of 5% and 10%, 10% CLP-CNF-alginate hydrogel having the biggest dimensional changes. On the other hand, the smallest dimensional changes occured in the case of the CNF-alginate hydrogel. Therefore, with the increased CLP concentrations and extended free-standing times, the hydrogel height decreased, and width increased due to the collapsing and drying of the CLP-CNF-alginate hydrogels.

Generally, the CNF-alginate and 1% CLP-CNF-alginate hydrogels were more durable in comparison to the CLP-CNF-alginate hydrogel with the higher CLP concentrations after cross-linking with 0.09 M $CaCl_2$ and left to stand freely on the table for 1 - 2 hours. During this time, the CNF-alginate hydrogel slightly collapsed, and 1% CLP-CNF-alginate hydrogel swelled more and more homogenously, both maintaining their moisture content. However, the dimensions did not considerably change. In contrast, the latter hydrogels with the increased CLP concentrations dried and slightly collapsed, especially from the upper parts of the hydrogels. At the same time, the bottom and central parts of the hydrogels slightly swelled, and the dimensions changed considerably. The hydrogels with the CLPs maintained their longitudinal dimensions worse than the CNF-alginate hydrogel when let to stand for 1 - 2 hours under ambient conditions (room temperature) after 3D bioprinting. The addition of CLPs clearly decreased the free-standing abilities of the hydrogels. Thus, when it comes to the overall appearance and drying of the hydrogels, CNF-alginate had the best properties when let to stand for 1 - 2 hours in the room air.

These results are reasonable. Shao et al. (2015) prepared microfibrillated MFC and LS blend hydrogels which were air dried in the room temperature for five days, followed by the drying in the 110 °C oven for 48 h. The hydrogels with the LS concentrations of 0 wt%, 10 wt%, and 30 wt% faced extensive shrinking during the air drying, from which the 30 wt% MFC-LS hydrogel shrank the least, sligthly in the vertical direction with the rounded edges (Shao et al., 2015). Up to certain high lignin concentration,

in their article 50 wt%, the addition of lignin increased the effect of air drying, causing major shrinking (Shao et al., 2015). Furthermore, Hossen et al. (2018) found out that the presence of the CNF fibres in the hydrogels led to the increased shrinking during air drying, when the dried hydrogels of pure CNF, pure methylcellulose (MetCMC), and CNF-MetCMC were compared. According to the authors, this was probably due to the inadequate hydrophilicity of the CNF fibres (Hossen et al., 2018). Due to this poor hydrophilicity, the CNF containing hydrogels could not retain as much moisture inside them as, for example, CNF-MetCMC hydrogel. Therefore, in the case of this Master's thesis, it is likely that the presence of CLPs in the CLP-CNF-alginate hydrogels increases the effect of drying and shrinking up to a certain limit.

11. Dynamic mechanical analysis (DMA)

The DMA was conducted for the CLP-CNF-alginate hydrogels with varying CLP content according to the instructions described earlier in the Subchapter 6.4. Nevertheless, the structural differences and density divergences in the hydrogels due to the varied 3D bioprinting conditions to ensure the adequate hydrogel structure, influenced negatively on the DMA results. The obtained DMA results are unreliable because of this structural variation even between the hydrogels of the same bioink composition. Therefore, the results are not presented here, but attached in the Appendix 6.

12. Conclusions

According to the hypothesis, the addition of CLPs was expected to prevent the hydrogel shrinking upon drying. This was a partially correct assumption. The level of hydrogel shrinking upon drying was decreased with the lower CLP concentrations, after which the shrinking increased, reaching the maximum at 10% concentration of CLPs. The higher level of shrinking was also associated with the higher degree of re-wetting. The benefits of these results, among others, are explained more thoroughly below.

The best hydrogels seem to be the 10% CLP-CNF-alginate and the 25% CLP-CNF-alginate. The evaluation process can be seen in the Appendix 7. In this evaluation process, the hydrogels were ranked according to their performance in the different measurements described in the Chapters 8 - 11, and the hydrogels which faced the best performance most frequently were selected. The hydrogel with the CLP concentration of 10% possess a high viscosity, good repeatability and re-wetting properties, ability to keep its shape when exposed to the high moisture and salt-water solutions, and good mechanical properties straight after 3D bioprinting and freeze-drying and re-wetting. The hydrogel of 25% CLP-CNF-alginate is very similar with the previous one, however, it has significantly better bioink strength. This improves the resolution of the 25% CLP-CNF-alginate hydrogel. Due to the better bioink strength and higher overall resistance of applied stress when it comes to stiffness, the 25% CLP-CNF-alginate hydrogel is also the toughest one when touched and the easiest to handle straight after 3D bioprinting. Unfortunately, in the case of these hydrogels, salt-water solution easily dissolves the hydrogel surface, in more detail the CLPs, and the hydrogels dry rather fast with considerable shrinking when let to stand in the room air.

In the future, safety and functionality of these hydrogels with cells need to be researched together with the new material combinations to ensure the material safety and degradation rates inside the body. The problems of aggregation of the CLPs containing bioinks, salt-water deteoriation, and fast drying also need more research, considering, e.g., new biomaterials and the optimal ion concentration and pH in salt-water solution. Interesting would also be to test how the increase in the CLP concentration changes the hydrogel properties even more. On the other hand, the interactions of CNF, alginate, and CLPs on the molecular level would be good to ensure for example with the FTIR, and the effect of cross-linking between alginate and CNF fibres on the mechanical properties of the hydrogels, together with the possible non-monotonic constitutive relation in the CLP-CNF-alginate bioinks, require further research. Improvements for the future could also include the different and

better mixing techniques for the bioink preparation to ensure better CLPs spreadability and bioink homogeneity.

Despite these drawbacks and requirements for the future research, 10% CLP-CNF-alginate and 25% CLP-CNF-alginate hydrogels have a big potential to respond to the challenges of the biomaterials, e.g., lack of mechanical properties, and they could offer a promising, strong, and natural material option in the combination with other materials for the regeneration of hard tissues. These hydrogels are easy to process also with the fine details and are safe to handle during transportation and surgery. They maintain their shape more likely inside the body and can better tolerate the deteoriating body conditions, such as humidity and body fluids. On the other hand, the beneficial water uptake, swelling, and water retention properties of the light and porous freeze-dried CLP-CNF-alginate hydrogels make these hydrogels a reckoned candidate in the regeneration and mimicking of soft tissues with the requirement for good water uptake properties. CLP-CNF-alginate hydrogels could be an up-and-coming alternative for the regeneration of kidneys in which the function of the kidneys is mainly focused on the water uptake and filtration abilities. In general, the many benefits of the CNF-alginate hydrogels with the higher CLP concentrations of 10% and 25% make them a potential alternative as a new material combination for tissue engineering and regenerative medicine.

REFERENCES

Aarstad, O., Heggset, E. B., Pedersen, I. S., Bjørnøy, S. H., Syverud, K., & Strand, B. L. (2017). Mechanical properties of composite hydrogels of alginate and cellulose nanofibrils. *Polymers*, *9*(8), 1-19. https://doi.org/10.3390/polym9080378

Abdelwahed, W., Degobert, G., Stainmesse, S., & Fessi, H. (2006). Freeze-drying of nanoparticles : Formulation, process and storage considerations. *Advanced Drug Delivery Reviews*, *58*, 1688–1713. https://doi.org/10.1016/j.addr.2006.09.017

Alexakis, C., Maxwell, P., & Bou-Gharios, G. (2006). Organ-specific collagen expression: Implications for renal disease. *Nephron - Experimental Nephrology*, *102*(3–4), 71–75. https://doi.org/10.1159/000089684

Anonymous, Thingiverse, Customizable cylinder, https://www.thingiverse.com/, 5 June 2018.

Ashok, R. P. B., Oinas, P., Lintinen, K., Sarwar, G., Kostiainen, M. A., & Österberg, M. (2018). Techno-economic assessment for the large-scale production of colloidal lignin particles, *Green Chemistry, 20*(21), 4911–4919. https://doi.org/10.1039/c8gc02805b

Atala, A., Lanza, R., Thomson, J., & Nerem, R. (2008). Principles of Regenerative Medicine. *Elsevier Science & Technology,* 2nd edition, 1-1448. ISBN: 978-0-12-369410-2

Atkinson, S. P., Lako, M., & Armstrong, L. (2013). Potential for pharmacological manipulation of human embryonic stem cells. *British Journal of Pharmacology, 169*(2), 269-289. DOI: 10.1111/j.1476-5381.2012.01978.x

Axpe, E., & Oyen, M. L. (2016). Applications of Alginate-Based Bioinks in 3D Bioprinting. *International Journal of Molecular Sciences, 17*(12), 1-11. https://doi.org/10.3390/ijms17121976

Benselfelt, T., Engström, J., & Wagberg, L. (2018). Supramolecular Double Networks of Cellulose Nanofibrils and Algae Polysaccharides with Excellent Wet Mechanical Properties. *Green Chemistry*, *20*(11), 2558–2570. https://doi.org/10.1039/C8GC00590G

Bian, H., Gao, Y., Wang, R., Liu, Z., & Wu, W. (2018). Contribution of lignin to the surface structure and physical performance of cellulose nanofibrils film. *Cellulose*, *25*(2), 1309–1318. https://doi.org/10.1007/s10570-018-1658-x

Bian, H., Jiao, L., Wang, R., Wang, X. Zhu, W., & Dai, H. (2018). Lignin nanoparticles as nano-spacers for tuning the viscoelasticity of cellulose nanofibril reinforced polyvinyl alcohol-borax hydrogel. *European Polymer Journal, 107,* 267-274*. https://doi.org/10.1016/j.eurpolymj.2018.08.028*

BIO X 3D Bioprinter User Manual. (2017). *Cellink©,* 6-48*.*

Bishop, E. S., Mostafa, S., Pakvasa, M., Luu, H. H., Lee, M. J., Wolf, J. M., Ameer, G. A., He, T.-C., & Reid, R. R. (2017). 3-D bioprinting technologies in tissue engineering and regenerative medicine: Current and future trends. *Genes & Diseases, 4*(4), 185–195. https://doi.org/10.1016/j.gendis.2017.10.002

Bonarski, J. T., Kifetew, G., & Olek, W. (2015). Effects of cell wall ultrastructure on the transverse shrinkage anisotropy of Scots pinewood. *Holzforschung, 69*(4), 501-507. DOI 10.1515/hf-2014-0075

Bush, J. R., Liang, H., Dickinson, M., & Botchwey, E. A. (2016). Xylan hemicellulose improves chitosan hydrogel for bone tissue regeneration. *Polymers for Advanced Technologies, 27*(8), 1050-1055. DOI: 10.1002/pat.3767

Campbell, J., McGuinness, I., Wirz, H., Sharon, A., & Sauer-Budge, A. F. (2015). Multimaterial and Multiscale Three-Dimensional Bioprinter. *Journal of Nanotechnology in Engineering and Medicine*, *6*(2), 021001. https://doi.org/10.1115/1.4031230

Chien, K. B., Makridakis, E., & Shah, R. N. (2013). Three-Dimensional Printing of Soy Protein Scaffolds for Tissue Regeneration. *Tissue Engineering Part C: Methods, 19*(6), 417-426. DOI: 10.1089/ten.tec.2012.0383

Chinga-Carrasco, G. (2018). Potential and Limitations of Nanocelluloses as Components in Biocomposite Inks for Three-Dimensional Bioprinting and for Biomedical Devices. *Biomacromolecules*, *19*(3), 701–711. https://doi.org/10.1021/acs.biomac.8b00053

Chuah, J. K. C., & Zink, D. (2017). Stem cell-derived cells and organoids: Recent breakthroughs and emerging applications. *Biotechnology Advances,* 35, 150-167. *http://dx.doi.org/10.1016/j.biotechadv.2016.21.001*

Coblas, D., Broboana, D., & Balan, C. (2016). Correlation between large amplitude oscillatory shear (LAOS) and steady shear of soft solids at the onset of the fluid rheological behavior. *Polymer,* 104, 215-226. https://doi.org/10.1016/j.polymer.2016.06.003

Cvetkovic, C., Raman, R., Chan, V., Williams, B. J., Tolish, M., Bajaj, P., Sakar, M. S., Asada, H. A., Saif, M. T. A., & Bashir, R. (2014). Three-dimensionally printed biological machines powered by skeletal muscle. *Proceedings of the National Academy of Sciences, 11*(28), 10125-10130. https://doi.org/10.1073/pnas.1401577111

Dai, L., Cheng, T., Duan, C., Zhao, W., Zhang, W., Zou, X., Aspler, J. & Ni, Y. (2019). 3D printing using plant-derived cellulose and its derivatives: A review. *Carbohydrate Polymers,* 203, 71-86. *https://doi.org/10.1016/j.carbpol.2018.09.027*

Dai, L., Liu, R., Hu, L.-Q., Zou, Z.-F., & Si, C.-L. (2017). Lignin Nanoparticle as a Novel Green Carrier for the Efficient Delivery of Resveratrol. *Acs Sustainable Chemistry & Engineering, 5*(9), 8241-8249. https://doi.org/10.1021/acssuschemeng.7b01903

Datta, P., Ayan, B., & Ozbolat, I. T. (2017). Bioprinting for vascular and vascularized tissue biofabrication. *Acta Biomaterialia,* 51*,* 1-20. https://doi.org/10.1016/j.actbio.2017.01.035

Derakhshanfar, S., Mibeleck, R., Xu, K., Zhang, X., Zhong, W., & Xing, M. (2017). 3D bioprinting for biomedical devices and tissue engineering: A review of recent trends and advances. *Bioactive Materials,* 3, 144-156*. https://doi.org/10.1016/j.bioactmat.2017.11.008*

Domínguez-robles, J., Soledad, M., Tamminen, T., Rodríguez, A., Larrañeta, E., & Jääskeläinen, A. (2018). International Journal of Biological Macromolecules Lignin-based hydrogels with " super-swelling " capacities for dye removal. *International Journal of Biological Macromolecules*, 115, 1249–1259. https://doi.org/10.1016/j.ijbiomac.2018.04.044

Dzobo, K., Thomford, N. E., Senthebane, D. A., Shipanga, H., Rowe, A., Dandara, C., Pillay, M., & Motaung, K. S. C. M. (2018). Advances in Regenerative Medicine and Tissue Engineering: Innovation and Transformation of Medicine. *Stem Cells International,* 2018, 1-24. https://doi.org/10.1155/2018/2495848

Erakovic, S., Jankovic, A., Tsui, G. C. P., Tang, C.-Y., Miskovic-Stankovic, V., & Stevanovic, T. (2014). Novel Bioactive Antimicrobial Lignin Containing Coatings on Titanium Obtained by Electrophoretic Deposition. *International Journal of Molecular Sciences,* 15, 12294–12322. https://doi.org/10.3390/ijms150712294

Ewoldt, R. H., Johnston, M. T., & Caretta, L. M. (2015). Experimental challenges of shear rheology: how to avoid bad data. *Complex Fluids and Biological Systems*, *Springer*, 1-36. http://dx.doi.org/10.1007/978-1-4939-2065-5_6

Farhat, W., Venditti, R., Mignard, N., Taha, M., Becquart, F., & Ayoub, A. (2017). Polysaccharides and lignin based hydrogels with potential pharmaceutical use as a drug delivery system produced by a reactive extrusion process. *International Journal of Biological Macromolecules*, 104, 564–575. https://doi.org/10.1016/j.ijbiomac.2017.06.037

Feng, X., Yang, Z., Chmely, S., Wang, Q., Wang, S., & Xie, Y. (2017). Lignin-coated cellulose nanocrystal filled methacrylate composites prepared via 3D stereolithography printing : Mechanical reinforcement and thermal stabilization. *Carbohydrate Polymers*, 169, 272–281. https://doi.org/10.1016/j.carbpol.2017.04.001

Figliuzzi, M., Bonandrini, B., & Remuzzi, A. (2017). Decellularized kidney matrix as functional material for whole organ tissue engineering. *Journal of Applied Biomaterials & Functional Materials*, *15*(4), 1-8. https://doi.org/10.5301/jabfm.5000393

Figueiredo, P., Lintinen, K., Hirvonen, J. T., Kostiainen, M. A., & Santos, H. A. (2018). Progress in Materials Science Properties and chemical modifications of lignin : Towards lignin-based nanomaterials for biomedical applications. *Progress in Materials Science,* 93, 233–269. https://doi.org/10.1016/j.pmatsci.2017.12.001

Figueiredo, P., Lintinen, K., Kiriazis, A., Hynninen, V., Liu, Z., Bauleth-Ramos, T., Rahikkala, A., Correia, A., Kohout, T., Sarmento, B., Yli-Kauhaluoma, J., Hirvonen, J., Ikkala, O., Kostiainen, M. A., & Santos, H. A. (2017). In vitro evaluation of biodegradable lignin-based nanoparticles for drug delivery and enhanced antiproliferation effect in cancer cells, *Biomaterials,* 121, 97–108. https://doi.org/10.1016/j.biomaterials.2016.12.034

Fitzsimmons, R. E., Aquilino, M. S., Quigley, J., Chebotarev, O., Tarlan, F., & Simmons, C. A. (2018). Generating vascular channels within hydrogel constructs using an economical open-source 3D bioprinter and thermoreversible gels. *Bioprinting*, 9, 7–18. https://doi.org/10.1016/j.bprint.2018.02.001

Francis, Y., & Bulletin, J. J. (2015). 3D printing for regenerative medicine : From bench to bedside. *MRS Bulletin, 40*(2), 145–154. DOI:10.1557/mrs.2015.5

Gao, G., & Cui, X. (2016). Three-dimensional bioprinting in tissue engineering and regenerative medicine. *Biotechnology Letters*, *38*(2), 203–211. https://doi.org/10.1007/s10529-015-1975-1

Gopinathan, J., & Noh, I. (2018). Recent trends in bioinks for 3D printing. *Biomaterials Research*, *22*(1), 1–15. https://doi.org/10.1186/s40824-018-0122-1

Graham, A. D., Olof, S. N., Burke, M. J., Armstrong, J. P. K., Mikhailova, E. A., Nicholson, J. G., Box, S. J., Szele, F. G., Perriman, A. W., & Bayley, H. (2017). High-Resolution Patterned Cellular Constructs by Droplet-Based 3D Printing. *Scientific Reports, 7*(1), 7004-7015. https://doi.org/10.1038/s41598-017-06358-x

Gunathilake, T. M. S. U., Ching, Y. C., Ching, K. Y., Chuah, C. H., & Abdullah, L. C. (2017). Biomedical and Microbiological Applications of Bio-Based Porous Materials : A Review. *Polymers, 9*(5), 1-16. https://doi.org/10.3390/polym9050160

Henriksson, I., Gatenholm, P., & Hägg, D. A. (2017). Increased lipid accumulation and adipogenic gene expression of adipocytes in 3D bioprinted nanocellulose scaffolds. *Biofabrication, 9*(1). https://doi.org/10.1088/1758-5090/aa5c1c

Highley, C. B., Prestwich, G. D., & Burdick, J. A. (2016). Recent advances in hyaluronic acid hydrogels for biomedical applications. *Current Opinion in Biotechnology,* 40, 34-40. https://doi.org/10.1016/j.copbio.2016.02.008

Homan, K. A., Kolesky, D. B., Skylar-scott, M. A., Herrmann, J., Obuobi, H., Moisan, A., & Lewis, J. A. (2016). Bioprinting of 3D Convoluted Renal Proximal Tubules on Perfusable Chips. *Scientific Reports*, *6*(1), 1–13. https://doi.org/10.1038/srep34845

Hong, S., Sycks, D., Chan, H. F., Lin, S., Lopez, G. P., Guilak, F., Leong, K. W., & Zhao, X. (2015). 3D Printing: 3D Printing of Highly Stretchable and Tough Hydrogels into Complex, Cellularized Structures. *Advanced Materials*, *27*(27), 4034-4040. https://doi.org/10.1002/adma.201570182

Hossen, M. R., Dadoo, N., Holomakoff, D. G., Co, A., Gramlich, W. M., & Mason, M. D. (2018). Wet stable and mechanically robust cellulose nanofibrils (CNF) based hydrogel. *Polymer,* 151, 231-241. *https://doi.org/10.1016/j.polymer.2018.07.016*

Hu, D., Wu, D., Huang, L., Jiao, Y., Li, L., Lu, L., & Zhou, C. (2018). 3D bioprinting of cell-laden scaffolds for intervertebral disc regeneration. *Materials Letters*, 223, 219–222. https://doi.org/10.1016/j.matlet.2018.03.204

Itoh, M., Nakayama, K., Noguchi, R., Kamohara, K., Furukawa, K., Uchihashi, K., Toda, S., Oyama, J.-I., Node, K., & Morita, S. (2015). Scaffold-Free Tubular Tissues Created by a Bio-3D Printer Undergo Remodeling and Endothelialization when Implanted in Rat Aortae. *PLoS ONE, 10*(9), 1-15. *DOI:10.1371/journal.pone.0136681*

Jackson, B. (2017). Organovo 3D prints the base structure of a human kidney for drug-testing. *3D printing industry, the authority on 3D printing. https://3dprintingindustry.com/news/organovo-3d-prints-base-structure-human-kidney-drug-testing-106341/*

Jackson, B. (2018). Prellis biologics aims to 3D print kidney vessels in 12 hours or less. *3D printing industry, the authority on 3D printing. https://3dprintingindustry.com/news/prellis-biologics-aims-to-3d-print-kidney-vessels-in-12-hours-or-less-134947/*

Jackson, B. (2016). Small steps, big impact - 3D bioprinting kidneys at Harvard. *3D printing industry, the authority on 3D printing. https://3dprintingindustry.com/news/small-steps-big-impact-3d-bioprinting-kidneys-harvard-96792/*

Jammalamadaka, U., & Tappa, K. (2018). Recent Advances in Biomaterials for 3D Printing and Tissue Engineering. *Journal of Functional Biomaterials*, *9*(1), 1-22. https://doi.org/10.3390/jfb9010022

Jayaramudu, T., Ko, H.-U., Kim, J. W., Choi, E. S., & Kim, J. (2019). Adhesion properties of poly(ethylene oxide)-lignin blend for nanocellulose composites. *Composites Part B,* 156, 43-50*. https://doi.org/10.1016/j.compositesb.2018.08.063*

Jiang, T., Deng, M., James, R., Nair, L. S., & Laurencin, C. T. (2014). Micro- and nanofabrication of chitosan structures for regenerative engineering. *Acta Biomaterialia, 10*(4), 1632-1645. http://dx.doi.org/10.1016/j.actbio.2013.07.003

Kai, D., Ren, W., Tian, L., Chee, P. L., Liu, Y., Ramakrishna, S., & Loh, X. J. (2016). Engineering Poly(lactide) − Lignin Nanofibers with Antioxidant Activity for Biomedical Application. *Acs Sustainable Chemistry & Engineering, 4*(10), 5268-5276*.* https://doi.org/10.1021/acssuschemeng.6b00478

Kapoor, S., & Kundu, S. C. (2016). Silk protein-based hydrogels: Promising advanced materials for biomedical applications. *Acta Biomaterialia*, 31, 17–32. https://doi.org/10.1016/j.actbio.2015.11.034

Keriquel, V., Oliveira, H., Rémy, M., Ziane, S., Delmond, S., Rousseau, B., Rey, S., Catros, S., Amédée, J., Guillemot, F., & Fricain, J.-C. (2017). *In situ* printing of mesenchymal stromal cells, by laser-assisted bioprinting, for *in vivo* bone regeneration applications. *Scientific Reports, 7*(1), 1–10. https://doi.org/10.1038/s41598-017-01914-x

Kesti, M., Eberhardt, C., Pagliccia, G., Kenkel, D., Grande, D., Boss, A., & Zenobi-wong, M. (2015). Bioprinting Complex Cartilaginous Structures with Clinically Compliant Biomaterials. *Advanced Functional Materials, 25*(48), 7406–7417. https://doi.org/10.1002/adfm.201503423

Kimura, H., Sakai, Y., & Fujii, T. (2018). Organ/body-on-a-chip based microfluidic technology for drug discovery. *Drug Metabolism and Pharmacokinetics, 33*(1), 43-48. https://doi.org/10.1016/j.dmpk.2017.11.003 13

Klemm, D., Kramer, F., Moritz, S., Lindström, T., Ankerfors, M., Gray, D., & Dorris, A. (2011). Nanocelluloses : A New Family of Nature-Based Materials. *Angewandte Chemie International Edition,* 5438–5466. https://doi.org/10.1002/anie.201001273

Kuo, C. K., & Ma, P. X. (2007). Maintaining dimensions and mechanical properties of ionically crosslinked alginate hydrogel scaffolds *in vitro*. *Journal of Biomedical Materials Research Part A, 84*(4), 899-907. https://doi.org/10.1002/jbm.a.31375

Lam, J., Truong, N. F., & Segura, T. (2014). Design of cell-matrix interactions in hyaluronic acid hydrogel scaffolds. *Acta Biomaterialia, 10*(4), 1571-1580. http://dx.doi.org/10.1016/j.actbio.2013.07.025

Larrañeta, E., Imícoz, M., Toh, J. X., Irwin, N. J., Ripolin, A., Perminova, A., Domínguez-Robles, J., Rodríguez, A., & Donnelly, R. F. (2018). Synthesis and Characterization of Lignin Hydrogels for Potential Applications as Drug Eluting Antimicrobial Coatings for Medical Materials. *ACS sustainable chemistry & engineering, 6*(7), 9037-9046. https://doi.org/10.1021/acssuschemeng.8b01371

Laurén, P., Somersalo, P., Pitkänen, I., Lou, Y.-R., Urtti, A., Partanen, J., Seppälä, J., Madetoja, M., Laaksonen, T., Mäkitie, A., & Yliperttula, M. (2017). Nanofibrillar cellulose-alginate hydrogel coated surgical sutures as cell-carrier systems. *PLoS ONE*, *12*(8), 1–17. https://doi.org/10.1371/journal.pone.0183487

Lawrence, E. A., Doherty, D., & Dhanda, R. (2018). Function of the nephron and the formation of urine. *Anaesthesia and Intensive Care Medicine*, *19*(5), 249–253. https://doi.org/10.1016/j.mpaic.2018.03.001

Lee, S.-J., Nowicki, M., Harris, B., & Zhang, L. G. (2017). Fabrication of a Higly Aligned Neural Scaffold via a Table Top Stereolithography 3D Printing and Electrospinning. *Tissue Engineering Part A, 23*(11-12), 491-502. DOI: 10.1089/ten.tea.2016.0353

Lee, V. K., & Dai, G. (2017). Printing of Three-Dimensional Tissue Analogs for Regenerative Medicine. *Annals of Biomedical Engineering, 45*(1), 115-131.

Leppiniemi, J., Lahtinen, P., Paajanen, A., Mahlberg, R., Metsä-Kortelainen, S., Pinomaa, T., Pajari, H., Vikholm-Lundin, I., Pursula, P., & Hytönen, V. P. (2017). 3D-Printable Bioactivated Nanocellulose-Alginate Hydrogels. *ACS Applied Materials and Interfaces*, *9*(26), 21959–21970. https://doi.org/10.1021/acsami.7b02756

Lê, H. Q., Dimic-Misic, K., Johansson, L.-S., Maloney, T., & Sixta, H. (2018). Effect of lignin on the morphology and rheological properties of nanofibrillated cellulose produced from c - valerolactone / water fractionation process. Cellulose, 25(1), 179–194. https://doi.org/10.1007/s10570-017-1602-5

Li, J., Chen, M., Fan, X., & Zhou, H. (2016). Recent advances in bioprinting techniques: Approaches, applications and future prospects. *Journal of Translational Medicine*, *14*(1), 1–15. https://doi.org/10.1186/s12967-016-1028-0

Li, K., Kong, Y., Zhang, M., Xie, F., Liu, P., & Xu, S. Differentiation of pluripotent stem cells for regenerative medicine. *Biochemical and Biophysical Research Communications, 471*(1), 1-4. http://dx.doi.org/10.1016/j.bbrc.2016.01.182

Li, X., Liu, L., Zhang, X., & Xu, T. (2018). Research and development of 3D printed vasculature constructs. *Biofabrication,* 10, 1-12.

Lievonen, M., Valle-delgado, J. J., Mattinen, M.-L., Hult, E.-L., Lintinen, K., Kostiainen, M. A., Paananen, A., Szilvay, G. R., Setl, H., & Österberg, M. (2016). A simple process for lignin nanoparticle preparation, *Green Chemistry, 18*(5), 1416–1422. https://doi.org/10.1039/c5gc01436k

Lim, K. S., Levato, R., Costa, P. F., Castilho, M. D., Alcala-Orozco, C. R., van Dorenmalen, K. M. A., Melchels, F. P. W., Gawlitta, D., Hooper, G. J., Malda, J., & Woofield, T. B. F. (2018). Bio-resin for high resolution lithography-based biofabrication of complex cell-laden constructs. *Biofabrication, 10*(3)*,* 1-14. https://doi.org/10.1088/1758-5090/aac00c

Lim, L., & Lim, E. W. L. (2018). A Review of Corneal Collagen Cross-linking - Current Trends in Practice Applications. *The Open Ophthalmology Journal,* 12, 181-213. DOI: 10.2174/1874364101812010181

Lin, H.-H., Hsieh, F.-Y., Tseng, C.-S., & Hsu, S.-H. (2016). Preparation and characterization of a biodegradable polyurethane hydrogel and the hybrid gel with soy protein for 3D cell-laden bioprinting. *Journal of Materials Chemistry, 4*(41), 6694-6705. DOI: 10.1039/c6tb01501h

Lin, Y.-Q., Wang, L.-R., Pan, L.-L., Wang, H., Zhu, G.-Q., Liu, W.-Y., Wang, J.-T., Braddock, M., & Zheng, M.-H. (2016). Kidney bioengineering in regenerative medicine: An emerging therapy for kidney disease. *Cytotherapy, 18*(2), 186-197. http://dx.doi.org/10.1016/j.jcyt.2015.10.004

Lintinen, K., Xiao, Y., Bangalore Ashok, R., Leskinen, T., Sakarinen, E., Sipponen, M., Muhammad, F., Oinas, P., Österberg, M., & Kostiainen, M. (2018). Closed Cycle Production of Concentrated and Dry Redispersible Colloidal Lignin Particles with a Three Solvent Polarity Exchange Method. *Green Chemistry*, 20, 843–850. https://doi.org/10.1039/C7GC03465B

Liu, J., Sun, L., Xu, W., Wang, Q., Yu, S., & Sun, J. (2019). Current advances and future perspectives of 3D printing natural-derived biopolymers. *Carbohydrate polymers,* 207, 297-316. https://doi.org/10.1016/j.carbpol.2018.11.077

Liu, H., Zhou, H., Lan, H., & Liu, T. (2017). Organ regeneration : integration application of cell encapsulation and 3D bioprinting. *Virtual and Physical Prototyping, 12*(4), 279-289. https://doi.org/10.1080/17452759.2017.1338065

Lou, Y.-R., Kanninen, L., Kuisma, T., Niklander, J., Noon, L. A., Burks, D., Urtti, A., & Yliperttula, M. (2014). The Use of Nanofibrillar Cellulose Hydrogel As a Flexible Three-Dimensional Model to Culture Human Pluripotent Stem Cells. *Stem Cells and Development*, *23*(4), 380–392. https://doi.org/10.1089/scd.2013.0314

Ma, Y., Sun, Y., Fu, Y., Fang, G., Yan, X., & Guo, Z. (2016). Chemosphere Swelling behaviors of porous lignin based poly (acrylic acid). *Chemosphere*, 163, 610–619. https://doi.org/10.1016/j.chemosphere.2016.08.035

Mandrycky, C., Wang, Z., Kim, K., & Kim, D. H. (2016). 3D bioprinting for engineering complex tissues. *Biotechnology Advances*, *34*(4), 422–434. https://doi.org/10.1016/j.biotechadv.2015.12.011

Markstedt, K., Escalante, A., Toriz, G., & Gatenholm, P. (2017). Biomimetic Inks Based on Cellulose Nanofibrils and Cross-Linkable Xylans for 3D Printing. *ACS Applied Materials and Interfaces*, *9*(46), 40878–40886. https://doi.org/10.1021/acsami.7b13400

Markstedt, K., Mantas, A., Tournier, I., Ávila, H. M., Hägg, D., & Gatenholm, P. (2015). 3D Bioprinting Human Chondrocytes with Nanocellulose − Alginate Bioink for Cartilage Tissue Engineering Applications. *Biomacromolecules,* 16, 1489-1496. https://doi.org/10.1021/acs.biomac.5b00188

Mattinen, M. L., Valle-Delgado, J. J., Leskinen, T., Anttila, T., Riviere, G., Sipponen, M., Paananen, A., Lintinen, K., Kostiainen, M., & Österberg, M. (2018). Enzymatically and chemically oxidized lignin nanoparticles for biomaterial applications. *Enzyme and Microbial Technology*, 111, 48–56. https://doi.org/10.1016/j.enzmictec.2018.01.005

McKee, T. J., & Komarova, S. V. (2017). Is it time to reinvent basic cell culture medium? *American Journal of Physiology - Cell Physiology*, *312*(5), C624–C626. https://doi.org/10.1152/ajpcell.00336.2016

Ming, J., Li, M., Han, Y., Chen, Y., Li, H., Zuo, B., & Pan, F. (2016). Novel two-step method to form silk fibroin fibrous hydrogel. *Materials Science and Engineering C*, 59, 185–192. https://doi.org/10.1016/j.msec.2015.10.013

Mogoşanu, G. D., & Grumezescu, A. M. (2014). Natural and synthetic polymers for wounds and burns dressing. *International Journal of Pharmaceutics*, *463*(2), 127–136. https://doi.org/10.1016/j.ijpharm.2013.12.015

Moon, K. H., Ko, I. K., Yoo, J. J., & Atala, A. (2016). Kidney diseases and tissue engineering. *Methods*, 99, 112–119. https://doi.org/10.1016/j.ymeth.2015.06.020

Munk, L., Sitarz, A. K., Kalyani, D. C., Mikkelsen, J. D., & Meyer, A. S. (2015). Can laccases catalyze bond cleavage in lignin? *Biotechnology Advances*, *33*(1), 13–24. https://doi.org/10.1016/j.biotechadv.2014.12.008

Murphy, S. V., & Atala, A. (2013). Organ engineering - combining stem cells, biomaterials, and bioreactors to produce bioengineered organs for transplantation. *BioEssays,* 35, 163-172. DOI 10.1002/bies.201200062

Murphy, S. V., & Atala, A. (2014). 3D bioprinting of tissues and organs. *Nature Biotechnology*, *32*(8), 773–785. https://doi.org/10.1038/nbt.2958

Murphy, S. V. & Atala, A. (2015). Regenerative Medicine. *Jama*, *313*(14), 1413–1414. https://doi.org/10.1038/nbt.2958.5

Nagarajan, N., Dupret-bories, A., Karabulut, E., & Zorlutuna, P. (2018). Enabling personalized implant and controllable biosystem development through 3D printing. *Biotechnology Advances*, *36*(2), 521–533. https://doi.org/10.1016/j.biotechadv.2018.02.004

Nascimento, D. M., Nunes, Y. L., Figueirêdo, M. C. B., de Azeredo, H. M. C., Aouada, F. A., Feitosa, J. P. A., Rosa, M. F., & Dufresne, A. (2018). Nanocellulose nanocomposite hydrogels: technological and environmental issues. *Green Chemistry, 20*(11), 2428–2448. https://doi.org/10.1039/c8gc00205c

Naseri-nosar, M., & Maria, Z. (2018). Wound dressings from naturally-occurring polymers : A review on homopolysaccharide-based composites. *Carbohydrate Polymers*, 189, 379–398. https://doi.org/10.1016/j.carbpol.2018.02.003

Neiman, J. A. S., Raman, R., Chan, V., Rhoads, M. G., Raredon, M. S. B., Velasquez, J. J., Dyer, R. I., Bashir, R., Hammond, P. T., & Griffith, L. G. (2015). Photopatterning of Hydrogel Scaffolds Coupled to Filter Materials Using Stereolithography for Perfused 3D Culture of Hepatocytes. *Biotechnology and Bioengineering, 112*(4), 777-787. https://doi.org/10.1002/bit.25494

Ng, W. L., Goh, M. H., Yeong, W. L., & Naing, M. W. (2018). Applying macromolecular crowding to 3D bioprinting: fabrication of 3D hierarchical porous collagen-based hydrogel constructs. *Biomaterials Science, 6*(3), 562-574. DOI: 10.1039/c7bm01015j

Nguyen, D., Hägg, D. A., Forsman, A., Ekholm, J., Nimkingratana, P., Brantsing, C., Kalogeropoulos, T., Zaunz, S., Concaro, S., Brittberg, M., Lindahl, A., Gatenholm, P., Enejder, A., & Simonsson, S. (2017). Cartilage Tissue Engineering by the 3D Bioprinting of iPS Cells in a Nanocellulose/Alginate Bioink. *Scientific Reports*, *7*(1), 1–1*0*. https://doi.org/10.1038/s41598-017-00690-y

Nypelö, T. E., Carrillo, C. A., & Rojas, O. J. (2015). Lignin supracolloids synthesized from (W/O) microemulsions: use in the interfacial stabilization of Pickering systems and organic carriers for silver metal. *Soft Matter, 11*(10), 2046–2054. https://doi.org/10.1039/c4sm02851a

Onyianta, A. J., Castellano, M., Dorris, M., Williams, R. L., & Vicini, S. (2018). The effects of morpholine pre-treated and carboxymethylated cellulose nanofibrils n the properties of alginate-based hydrogels. *Carbohydrate Polymers, 198, 320-327. https://doi.org/10.1016/j.carbpol.2018.06.084*

Owen, R., Sherborne, C., Paterson, T., Green, N. H., Reilly, G. C., & Glaeyssens, F. (2016). Emulsion templated scaffolds with tunable mechanical properties for bone tissue engineering. *Journal of the Mechanical Behavior of Biomedical Materials,* 54, 159-172. http://dx.doi.org/10.1016/j.jmbbm.2015.09.019

Ozbolat, I. T., Hospodiuk, M., Dey, M., & Sosnoski, D. (2017). The Bioink: a comprehensive review on bioprintable materials. *Biotechnology Advances, 35*(2), 217-239. https://doi.org/10.1016/B978-0-12-803010-3.00003-2

Park, C. H., Jeong, L., Cho, D., Kwon, O. H., & Park, W. H. (2013). Effect of methylcellulose on the formation and drug release behavior of silk fibroin hydrogel. *Carbohydrate Polymers*, *98*(1), 1179–1185. https://doi.org/10.1016/j.carbpol.2013.07.028

Park, J., Lee, S. J., Chung, S., Lee, J. H., Kim, W. D., Lee, J. Y., & Park, S. A. (2017). Cell-laden 3D bioprinting hydrogel matrix depending on different compositions for soft tissue engineering: Characterization and evaluation. *Materials Science & Engineering C,* 71, 678-684. https://doi.org/10.1016/j.msec.2016.10.069

Park, S.-J., Gazzola, M., Park, K. S., Park, S., Di Santo, V., Blevins, E. L., Lind, J. U., Campbell, P. H., Dauth, S., Capulli, A., Pasqualini, F. S., Ahn, S., Cho, A., Yuan, H., Maoz, B. M., Vijaykumar, R., Cho, J.-W., Deisseroth, K., Lauder, G. V., Mahadevan, L., & Parker, K. K. (2017). Phototactic guidance of a tissue-engineered soft-robotic ray. *Science (New York, N. Y.)*, *353*(6295), 158–162. https://doi.org/10.1126/science.aaf4292

Passauer, L., Fischer, K., & Liebner, F. (2011). Preparation and physical characterization of strongly swellable oligo(oxyethylene) lignin hydrogels. *Holzforschung, 65*(3), 309–317. https://doi.org/10.1515/HF.2011.044

Pavyde, E., Usas, A., & Maciulaitis, R. (2016). Regenerative pharmacology for the treatment of acute kidney injury: Skeletal muscle stem/progenitor cells for renal regeneration? *Pharmacological Research,* 113, 802-807. http://dx.doi.org/10.1016/j.phrs.2016.03.014

Peloso, A., Tamburrini, R., Edgar, L., Wilm, B., Katari, R., Perin, L., Patricia, M., & Orlando, G. (2016). Extracellular matrix scaffolds as a platform for kidney regeneration. *European Journal of Pharmacology*, 790, 21–27. https://doi.org/10.1016/j.ejphar.2016.07.038

Piras, C. C., Fernández-Prieto, S., & De Borggraeve, W. M. (2017). Nanocellulosic materials as bioinks for 3D bioprinting. *Biomaterials Science*, *5*(10), 1988–1992. https://doi.org/10.1039/C7BM00510E

Pääkkönen, T., Dimic-misic, K., Orelma, H., Pönni, R., Vuorinen, T., & Maloney, T. (2016). Effect of xylan in hardwood pulp on the reaction rate of TEMPO-mediated oxidation and the rheology of the final nanofibrillated cellulose gel. *Cellulose, 23*(1), 277–293. https://doi.org/10.1007/s10570-015-0824-7

Quraishi, S., Martins, M., Barros, A. A., Gurikov, P., Raman, S. P., Smirnova, I., Duarte, A. R. C., & Reis, R. L. (2015). Novel non-cytotoxic alginate–lignin hybrid aerogels as scaffolds for tissue engineering, *The Journal of Supercritical Fluids,* 105, 1-8. https://doi.org/10.1016/j.supflu.2014.12.026

Radenkovic, D., Solouk, A., & Seifalian, A. (2016). Personalized development of human organs using 3D printing technology. *Medical Hypotheses*, 87, 30–33. https://doi.org/10.1016/j.mehy.2015.12.017

Raschip, I. E., Hitruc, E. G., & Vasile, C. (2011). Semi-interpenetrating polymer networks containing polysaccharides. II .Xanthan / lignin networks: a spectral and thermal characterization. *High Performance Polymers, 23*(3), 219–229. https://doi.org/10.1177/0954008311399112

Razmaria, A. A. (2016). Chronic Kidney Disease. *JAMA Patient Page*, *315*(20), 2248. doi:10.1001/jama.2016.1426

Reeb, J. (1998). WHY DOES MY WOOD SHRINK LIKE THIS ?, *Oregon State University*, 8–11

Rees, A., Powell, L. C., Chinga Carrasco, G., Gethin, D. T., Syverud, K., Hill, K. E., & Thomas, D. W. (2014). 3D Bioprinting of Carboxymethylated-Periodate Oxidized Nanocellulose Constructs for Wound Dressing Applications. *BioMed Research International,* 2015, 1-7. http://dx.doi.org/10.1155/2015/925757

Ribeiro, A., Blokzijl, M. M., Levato, R., Visser, C. W., Castilho, M., Hennink, W. E., Vermonden, T., & Malda, J. (2018). Assessing bioink shape fidelity to aid material development in 3D bioprinting. *Biofabrication*, *10*(1), 1-9. https://doi.org/10.1088/1758-5090/aa90e2

Richter, A. P., Bharti, B., Armstrong, H. B., Brown, J. S., Plemmons, D., Paunov, V. N., Stoyanov, S. D., & Velev, O. D. (2016). Synthesis and Characterization of Biodegradable Lignin Nanoparticles with Tunable Surface Properties. *Langmuir: the ACS journal of surfaces and colloids, 32*(25), 6468-6477.

Rodríguez, M. I. A., Rodríguez Barroso, L. G., & Sánchez, M. L. (2018). Collagen: A review on its sources and potential applications. *Journal of Cosmetic Dermatology, 17*(1), 20-26. DOI: 10.1111/jocd.12450

Rojo, E., Peresin, M. S., Sampson, W. W., Hoeger, I. C., Vartiainen, J., Laine, J., & Rojas, O. J. (2015). Comprehensive elucidation of the effect of residual lignin on the physical, barrier, mechanical and surface properties of nanocellulose films. *Green Chemistry, 17*(3), 1853–1866. https://doi.org/10.1039/c4gc02398f

Rol, F., Belgacem, M. N., Gandini, A., & Bras, J. (2018). Recent advances in surface-modified cellulose nanofibrils. *Progress in Polymer Science,* 1-24. https://doi.org/10.1016/j.progpolymsci.2018.09.002

Sadri-Ardekani, H., & Atala, A. (2016). Regenerative medicine. *Methods*, 99, 1–2. https://doi.org/10.1016/j.ymeth.2016.04.001

Savage, N. (2016). Technology: The promise of printing. *Nature*, *540*(7632), S56–S57. https://doi.org/10.1038/540S56a

Schacht, K., Jüngst, T., Schweinlin, M., Ewald, A., Groll, J., & Scheibel, T. (2015). Biofabrication of cell-loaded 3D spider silk constructs. *Angewandte Chemie International Edition, 54*(9), 2816–2820. https://doi.org/10.1002/anie.201409846

Schmitt, A., Csiki, R., Saldamli, B., Tübel, J., Florian, K., Siebenlist, S., Balmayor, E., & Burgkart, R. (2017). Optimized protocol for whole organ decellularization. *European Journal of Medical Research, 22*(1), 1-9. DOI 10.1186/s40001-017-0272-y

Shankar, S., Reddy, J. P., & Rhim, J.-W. 2015. Effect of lignin on water vapor barrier, mechanical, and structural properties of agar/lignin composite films. *International Journal of Biological Macromolecules,* 81, 267-273. http://dx.doi.org/10.1016/j.ijbiomac.2015.08.015

Shao, Y., Chaussy, D., Grosseau, P., & Beneventi, D. (2015). Use of Microfibrillated Cellulose/Lignosulfonate Blends as Carbon Precursors: Impact of Hydrogel Rheology on 3D Printing. *Industrial & Engineering Chemistry Research, 54*(43), 10575-10582. https://doi.org/10.1021/acs.iecr.5b02763

Shaw, R. (2015). Dynamic Light Scattering Training Achieving reliable nano particle sizing. *Malvern,* 1-132

Shi, W., Sun, M., Hu, X., Ren, B., Cheng, J., Li, C., Duan, X., Xin, F., Jiying, Z., Chen, H., & Ao, Y. (2017). Structurally and Functionally Optimized Silk-Fibroin–Gelatin Scaffold Using 3D Printing to Repair Cartilage Injury In Vitro and In Vivo. *Advanced Materials*, *29*(29), 1–7. https://doi.org/10.1002/adma.201701089

Short, A. R., Czeisler, C., Stocker, B., Cole, S., Otero, J. J., & Winter, J. O. (2017). Imaging Cell–Matrix Interactions in 3D Collagen Hydrogel Culture Systems. *Macromolecular Bioscience*, *17*(6), 1–8. https://doi.org/10.1002/mabi.201600478

Si, Y., Wang, L., Wang, X., Tang, N., Yu, J., & Ding, B. (2017). Ultrahigh-Water-Content, Superelastic, and Shape-Memory Nanofiber-Assembled Hydrogels Exhibiting Pressure-Responsive Conductivity. *Advanced Materials, 29*(24), 1-7. https://doi.org/10.1002/adma.201700339

Siqueira, G., Kokkinis, D., Libanori, R., Hausmann, M. K., Gladman, A. S., Neels, A., Tingaut, P., Zimmermann, T., Lewis, J. A., & Studart, A. R. (2017). Cellulose Nanocrystal Inks for 3D Printing of Textured Cellular Architectures. *Advanced Functional Materials*, *27*(12). https://doi.org/10.1002/adfm.201604619

Sipponen, M., Farooq, M., Koivisto, J., Pellis, A., Seitsonen, J., & Österberg, M. (2018). Spatially confined lignin nanospheres for biocatalytic ester synthesis in aqueous media. *Nature Communications,* 9, 1-7. DOI: 10.1038/s41467-018-04715-6

Sipponen, M. H., Smyth, M., Leskinen, T., Johansson, L.-S., & Österberg, M. (2017). All-lignin approach to prepare cationic colloidal lignin particles: stabilization of durable Pickering emulsions. *Green Chemistry, 19*(24), 5831–5840. https://doi.org/10.1039/c7gc02900d

Sornkamnerd, S., Okajima, M. K., & Kaneko, T. (2017). Tough and Porous Hydrogels Prepared by Simple Lyophilization of LC Gels. *ACS Omega, 2*(8), 5304-5314. https://doi.org/10.1021/acsomega.7b00602

Stocco, T. D., Bassous, N. J., Zhao, S., Granato, A. E. C., Webster, T. J., & Lobo, A. O. (2018). Nanofibrous scaffolds for biomedical applications. *Nanoscale, 10*(26), 12228–12255. https://doi.org/10.1039/c8nr02002g

Sultan, S., & Mathew, A. P. (2018). 3D printed scaffolds with gradient porosity based on cellulose nanocrystal hydrogel. *Nanoscale*, *10*(9), 4421–4431. https://doi.org/10.1039/C7NR08966J

Sultan, S., Siqueira, G., Zimmermann, T., & Mathew, A. P. (2017). 3D printing of nano-cellulosic biomaterials for medical applications. *Current Opinion in Biomedical Engineering*, 2, 29–34. https://doi.org/10.1016/j.cobme.2017.06.002

Susaimanickam, P. J., Maddileti, S., Pulimamidi, V. K., Boyinpally, S. R., Naik, R. R., Naik, M. N., Reddy, G. B., Sangwan, V. S., & Mariappan, I. (2017). Generating minicorneal organoids from human induced pluripotent stem cells. *Development, 144*(13), 2338-2351. doi:10.1242/dev.143040

Tabriz, A. G., Hermida, M. A., Leslie, N. R., & Shu, W. (2015). Three-dimensional bioprinting of complex cell laden alginate hydrogel structures. *Biofabrication, 7*(4), 1-11. *https://doi.org/10.1088/1758-5090/7/4/045012*

Takasato, M., Er, P. X., Chiu, H. S., Maier, B., Baillie, G. J., Ferguson, C., Parton, R. G., Wolvetang, E. J., Roost, M. S., Chuva de Sousa Lopez, S. M., & Little, M. H. (2015). Kidney organoids from human iPS cells containing multiple lineages and model human nephrogenesis. *Nature, 526*(7574), 564-568. doi:10.1038/nature15695

Takasato, M., & Little, M. H. (2016). A strategy for generating kidney organoids: Recapitulating the development in human pluripotent stem cells. *Developmental Biology, 420*(2), 210-220. http://dx.doi.org/10.1016/j.ydbio.2016.08.024

Tappa, K., & Jammalamadaka, U. (2018). Novel Biomaterials Used in Medical 3D Printing Techniques. *Journal of Functional Biomaterials, 9*(1), 1-17. https://doi.org/10.3390/jfb9010017

Tian, H., Guo, G., Fu, X., Yao, Y., Yan, L., & Xiang, A. (2018). Fabrication, properties and applications of soy-protein-based materials: A review. *International Journal of Biological Macromolecules,* 120, 475-490. https://doi.org/10.1016/j.ijbiomac.2018.08.110

Ullah, M. W., Aljohani, W., Zhang, X., & Yang, G. (2018). Bioprinting and its applications in tissue engineering and regenerative medicine. *International Journal of Biological Macromolecules,* 107, 261-275. https://doi.org/https://doi.org/10.1016/j.ijbiomac.2017.08.171

Unbekandt, M., & Davies, J. A. (2010). Dissociation of embryonic kidneys followed by reaggregation allows the formation of renal tissues. *Kidney International*, *77*(5), 407–416. https://doi.org/10.1038/ki.2009.482

Vedadghavami, A., Minooei, F., Hossein, M., Khetani, S., Rezaei, A., Mashayekhan, S., & Sanati-nezhad, A. (2017). Manufacturing of hydrogel biomaterials with controlled mechanical properties for tissue engineering applications. *Acta Biomaterialia*, 62, 42–63. https://doi.org/10.1016/j.actbio.2017.07.028

Vijayavenkataraman, S., Yan, W.-C., Lu, W F., Wang, C-H., & Fuh, J. Y. H. (2018). 3D bioprinting of tissues and organs for regenerative medicine. *Advanced Drug Delivery Reviews,* 132, 296-332*. https://doi.org/10.1016/j.addr.2018.07.004*

Wang, K., Loo, L. S., & Goh, K. L. (2016). A facile method for processing lignin reinforced chitosan biopolymer microfibres: optimising the fibre mechanical properties through lignin type and concentration. *Materials Research Express, 3*(3), 1–13.

Wang, Z., Abdulla, R., Parker, B., Samanipour, R., Ghosh, S., & Kim, K. (2015). A simple and high-resolution stereolithography-based 3D bioprinting system using visible light crosslinkable bioinks. *Biofabrication, 7*(4), 1-10. doi:10.1088/1758-5090/7/4/045009

Wang, Z., Kumar, H., Tian, Z., Jin, X., Holzman, J. F., Menard, F., & Kim, K. (2018). Visible Light Photoinitiation of Cell-Adhesive Gelatin Methacryloyl Hydrogels for Stereolithography 3D bioprinting. *ACS Applied Materials & Interfaces, 10*(32), 26859-26869. DOI: 10.1021/acsami.8b06607

Williams, B. J., Anand, S. V, Rajagopalan, J., & Saif, M. T. A. (2014). A self-propelled biohybrid swimmer at low Reynolds number. *Nature Communications*, 5, 1–8. https://doi.org/10.1038/ncomms4081

Witzler, M., Alzagameem, A., Bergs, M., El Khaldi-hansen, B., Klein, S. E., Hielscher, D., Kamm, B., Kreyenschmidt, J., Tobiasch, E., & Schulze, M. (2018). Lignin-Derived Biomaterials for Drug Release and Tissue Engineering. *Molecules,* 23(8), 1–22. https://doi.org/10.3390/molecules23081885

Wu, Y., Lin, Z. Y. (William), Wenger, A. C., Tam, K. C., & Tang, X. (Shirley). (2018). 3D bioprinting of liver-mimetic construct with alginate/cellulose nanocrystal hybrid bioink. *Bioprinting*, 9, 1–6. https://doi.org/10.1016/j.bprint.2017.12.001

Xu, W., Wang, X., Sandler, N., Willför, S., & Xu, C. (2018). Three-Dimensional Printing of Wood-Derived Biopolymers: A Review Focused on Biomedical Applications. *Acs Sustainable Chemistry & Engineering, 6*(5), 5663-5680. https://doi.org/10.1021/acssuschemeng.7b03924

Yu, I., Kaonis, S., & Chen, R. (2017). A Study on Degradation Behavior of 3D Printed Gellan Gum Scaffolds. *Procedia CIRP,* 65, 78-83. https://doi.org/10.1016/j.procir.2017.04.020

Yu, Y., Moncal, K. K., Li, J., Peng, W., Rivero, I., Martin, J. A., & Ozbolat, I. T. (2016). Three-dimensional bioprinting using self-Assembling scalable scaffold-free “tissue strands” as a new bioink. *Scientific Reports, 6*(1), 1–11. https://doi.org/10.1038/srep28714

Zadeh, E. M., O'Keefe, S. F., & Kim, Y.-T. (2018). Utilization of Lignin in Biopolymeric Packaging Films. *ACS Omega, 3*(7), 7388-7398. DOI: 10.1021/acsomega.7b01341

Zarrintaj, P., Manoucheri, S., Ahmadi, Z., Saeb, M. R., Urbanska, A. M., Kaplan, D. L., & Mozafari, M. (2018). Agarose-based biomaterials for tissue engineering. *Carbohydrate Polymers*, 187, 66-84. https://doi.org/10.1016/j.carbpol.2018.01.060

Zhang, B., Luo, Y., Ma, L., Gao, L., Li, Y., Xue, Q., Yang, H., & Cui, Z. (2018). 3D bioprinting: an emerging technology full of opportunities and challenges. *Bio-Design and Manufacturing*, *1*(1), 2–13. https://doi.org/10.1007/s42242-018-0004-3

Zhang, Y. S., Arneri, A., Bersini, S., Shin, S.-R., Zhu, K., Goli-Malekabadi, Z., Aleman, J., Colosi, C., Busignani, F., Dell'ERba, V., Bishop, C., Shupe, T., Demarchi, D., Moretti, M., Rasponi, M., Dokmeci, M. R., Atala, A., & Khademhosseini, A. (2016). Bioprinting 3D microfibrous scaffolds for engineering endothelialized myocardium and heart-on-a-chip. *Biomaterials,* 110, 45-59. https://doi.org/10.1016/j.biomaterials.2016.09.003

Zhang, Y. S., Yue, K., Aleman, J., Mollazadeh-Moghaddam, K., Bakht, S. M., Yang, J., Jia, W., Dell'Erba, V., Assawes, P., Shin, S. R., Dokmeci, M. R., Oklu, R., & Khademhosseini, A. (2017). 3D Bioprinting for Tissue and Organ Fabrication. *Annals of Biomedical Engineering*, *45*(1), 148–163. https://doi.org/10.1007/s10439-016-1612-8

Zheng, Z., Wu, J., Liu, M., Wang, H., Li, C., Rodriguez, M. J., Li, G., Wang, X., & Kaplan, D. L. (2018). 3D Bioprinting of Self-Standing Silk-Based Bioink. *Advanced Healthcare Materials*, *7*(6), 1–12. https://doi.org/10.1002/adhm.201701026

Zhong, C., Xie, H. Y., Zhou, L., Xu, X., & Zheng, S. Sen. (2016). Human hepatocytes loaded in 3D bioprinting generate mini-liver. *Hepatobiliary and Pancreatic Diseases International*, *15*(5), 512–518. https://doi.org/10.1016/S1499-3872(16)60119-4

Zhu, D., Wang, H., Trinh, P., Heilshorn, S. C., & Yang, F. (2017). Elastin-like protein-hyaluronic acid (ELP-HA) hydrogels with decoupled mechanical and biochemical cues for cartilage regeneration. *Biomaterials,* 127, 132-140. http://dx.doi.org/10.1016/j.biomaterials.2017.02.010

Zhu, W., Cui, H., Boualam, B., Masood, F., Flynn, E., Rao, R. D., Zhang, Z.-Y., & Zhang, L. G. (2018). 3D bioprinting mesenchymal stem cell-laden construct with core-shell nanospheres for cartilage tissue engineering. *Nanotechnology, 29*(18), 185101-185111. https://doi.org/10.1088/1361-6528/aaafa1

APPENDICES.

APPENDIX 1.

Calculations considering the dry matter content and yield of the cellulose and CLPs at the different preparation stages.

Table 10. *Dry weight analysis of the alkaline treated cellulose and the amount of moist cellulose required for TEMPO-oxidation.*

Aluminium cup (g)	Sample (g)	Aluminium cup + dm (g)	Dm (%)	Dry cellulose (g)	For TEMPO-oxidation (g)
1.160	1.006	1.500	**24**	50	**205.79**

Table 11. *Dry weight analysis and yield of the TEMPO-oxidated cellulose.*

Aluminium cup (g)	Sample (g)	Aluminium cup + dm (g)	Dm (%)	Dry TEMPO-cellulose (g)	Yield (%)
1.164	1.038	1.2975	**1.298**	41.1	**82.11**

Table 12. *Dry weight analysis and yield of the acid-treated TEMPO-oxidated cellulose.*

Aluminium cup (g)	Sample (g)	Aluminium cup + dm (%)	Dm (%)	Dry TEMPO-cellulose	Dry acid-treated TEMPO-cellulose	Yield (%)
1.149	1.036	1.417	**25.92**	4.106	3.732	**90.90**

Table 13. *Dry weight analysis of the CLP dispersion after the dialysis.*

Aluminium cup (g)	1 ml sample (g)	Aluminium cup + dm (g)	Dm (%)
1.157	9.972	1.178	**0.211**

Table 14. *Yield of the CLPs after the freeze-drying*.

Lignin in (g)	Empty bottle (g)	Empty bottle + CLPs (g)	Yield (%)
2.288	54.04	57.091	**75.0**

APPENDIX 2.

Analysis of the LVR and crossover points of the bioinks in the amplitude sweep measurements.

Table 15. *Analysis of the LVR of the amplitude sweep measurement according to the storage modulus, G' (Pa), based on the Figure 22.*

COMPOSITION	LVR - START (Pa)	LVR – END (Pa)	LVR - Δ (Pa)
CNF-alginate	2696.8	2916.5	219.7
1% CLP-CNF-alginate	3168.9	3458.6	289.7
5% CLP-CNF-alginate	**2319.0**	**2531.1**	**212.1**
10% CLP-CNF-alginate	2413.0	2650.9	237.9
25% CLP-CNF-alginate	**3117.7**	**3420.7**	**303.0**

Table 16. *Analysis of the crossover point of the storage modulus, G' (Pa), and loss modulus, G'' (Pa), curves of the amplitude sweep measurement, based on the Figure 22.*

COMPOSITION	STORAGE MODULUS, G' (Pa)	LOSS MODULUS, G'' (Pa)	STORAGE MODULUS/ LOSS MODULUS ($G'/G''_{0.5\%}$)	SHEAR STRESS, γ (Pa)
CNF-alginate	82.582	80.929	0.00255	205.29
1% CLP-CNF-alginate	**98.301**	**96.409**	**0.00255**	**244.58**
5% CLP-CNF-alginate	**65.995**	**68.673**	**0.00240**	**169.18**
10% CLP-CNF-alginate	71.821	74.083	0.00242	183.18
25% CLP-CNF-alginate	**87.833**	**90.502**	**0.00243**	**224.02**

APPENDIX 3.

Data and calculations considering the changes in hydrogel dimensions after each storage conditions.

Table 17. *Dimensional data (cm) and changes (%) for the freeze-dried hydrogels.*

Composition	Height (before)	Height (after)	Width (before)	Width (after)	%_height	%_width
CNF-alginate	2	1.7	1.5	1.2	**-15**	**-20**
1% CLP-CNF-alginate	1.8	1.8	1.5	1.3	**0**	**-13**
5% CLP-CNF-alginate	1.4	1.3	1.5	1.5	**-7**	**0**
10% CLP-CNF-alginate	2	1.2	1.5	1.2	**-40**	**-20**
25% CLP-CNF-alginate	2	1.5	1.5	1.4	**-25**	**-7**

Table 18. *Dimensional data (cm) and changes (%) for the re-wetted hydrogels.*

Composition	Height (before)	Height (after)	Width (before)	Width (after)	%_height	%_width
CNF-alginate	1.7	1.9	1.2	1.4	**12**	**17**
1% CLP-CNF-alginate	1.8	1.7	1.5	1.5	**-6**	**0**
5% CLP-CNF-alginate	1.3	1.4	1.5	1.4	**8**	**-7**
10% CLP-CNF-alginate	1.2	1.8	1.2	1.5	**50**	**25**
25% CLP-CNF-alginate	1.5	1.8	1.4	1.5	**20**	**7**

Table 19. *Dimensional data (cm) and changes (%) for the hydrogels after salt-water solution.*

Composition	Height (before)	Height (after)	Width (before)	Width (after)	%_height	%_width
CNF-alginate	1.9	1.8	1.5	1.3	**-5**	**-13**
1% CLP-CNF-alginate	1.8	1.8	1.5	1.5	**0**	**0**
5% CLP-CNF-alginate	1.2	1.2	1.5	1.5	**0**	**0**
10% CLP-CNF-alginate	1.4	1.4	1.5	1.5	**0**	**0**
25% CLP-CNF-alginate	2	2	1.5	1.5	**0**	**0**

Table 20 and Table 21. *Dimensional data (cm) and changes (%) for the hydrogels after humidity chamber and for the hydrogels after free-standing measurements.*

Composition	Height (before)	Height (after)	Width (before)	Width (after)	%_height	%_width
CNF-alginate	2	1.8	1.5	1.3	**-10**	**-13**
1% CLP-CNF-alginate	1.9	1.8	1.5	1.5	**-5**	**0**
5% CLP-CNF-alginate	1.9	1.75	1.5	1.5	**-8**	**0**
10% CLP-CNF-alginate	2	1.8	1.5	1.4	**-10**	**-7**
25% CLP-CNF-alginate	2	1.7	1.5	1.5	**-15**	**0**

Composition	Height (before)	Height (after)	Width (before)	Width (after)	%_height	%_width
CNF-alginate	1.8	1.8	1.5	1.5	**0**	**0**
1% CLP-CNF-alginate	1.8	1.8	1.5	1.6	**0**	**7**
5% CLP-CNF-alginate	1.6	1.5	1.5	1.7	**-6**	**13**
10% CLP-CNF-alginate	2	1.7	1.5	1.7	**-15**	**13**
25% CLP-CNF-alginate	2	1.8	1.5	1.5	**-10**	**0**

APPENDIX 4.

Calculations considering the volume repeatability of hydrogels after 3D bioprinting.

Table 22. *Calculations for the hydrogel repeatability in 3D bioprinting.*

Volume	CNF-alginate	1% CLP-CNF-alginate	5% CLP-CNF-alginate	10% CLP-CNF-alginate	25% CLP-CNF-alginate
Average volume (cm^3)	**13.4**	**12.3**	**10.1**	**12.3**	**14.1**
Standard deviation	1.6	2.2	2.3	2.5	0.0
Variance	2.5	4.9	5.5	6.4	0.0
Standard deviation (%)	**11.8**	**18.0**	**23.2**	**20.6**	**0.0**
Variance %	18.6	39.8	54.2	52.0	0.0

APPENDIX 5.

DMA results and their interpretation considering the CLP-CNF-alginate hydrogels with varying CLP content, 7 pp.

In this Chapter, the ability of the different hydrogel compositions to restrict the applied sress during the DMA was evaluated. The obtained data consisted of the applied stress plotted against strain, displacement, and stiffness. Only the displacement and stiffness has been evaluated in this Chapter, due to the similarity of the strain and displacement. Strain and displacement stand for the deformation occurred during the DMA, whereas stiffness is the applied stress divided by the deformation. The Figures 39 and 40 summarize the mechanical behavior of the various hydrogels with different compositions. Later, the Table 9 and Figure 41 summarize the numerical data considering Young's modulus, E (N/m^2), and slope, k (Ea/l_0), based on the Figures 39 and 40. In the case of the stress-displacement curves, the three characteristic deformation stages typically found in cellular networks can be detected (Si et al., 2017). They are a linear or Hookean elastic regime with a Young's modulus, a subsequent plateau stage, and a densification regime with the stress rising sharply (Si et al., 2017).

When observing the displacement curves, (Figures 39 and 40), in the case of the 3D bioprinted hydrogels, more stress is needed to cause a displacement or, in other words, compression when hydrogels of 10% and 25% CLP-CNF-alginate are compared to the regular hydrogel of CNF-alginate. These CLPs containing hydrogels also have a smaller overall displacement in comparison to the CNF-alginate hydrogel, which is seen as the CLPs containing hydrogel curves reacting before the CNF-alginate hydrogel. On the other hand, less stress is needed to cause a displacement in the case of the 1% and 5% CLP-CNF-alginate hydrogels in comparison to the CNF-alginate hydrogel. The hydrogels of the 1% and 5% CLP-CNF-alginate are difficult to interpret only based on this Figure 39, requiring more repeated measurements, whereas the 10% CLP-CNF-alginate hydrogel has the highest strength. In the case of the re-wetted and freeze-dried hydrogels, it is evident that the amount of applied stress needed to

cause the compression has increased, which means a considerable increase also in the strength and stiffness of the hydrogels. The freeze-drying and re-wetting increases the mechanical strength of all the hydrogels and, at the same time, unifies the occurred displacement in the case of the individual hydrogels, CNF-alginate having the smallest and 10% CLP-CNF-alginate the highest amount of displacement.

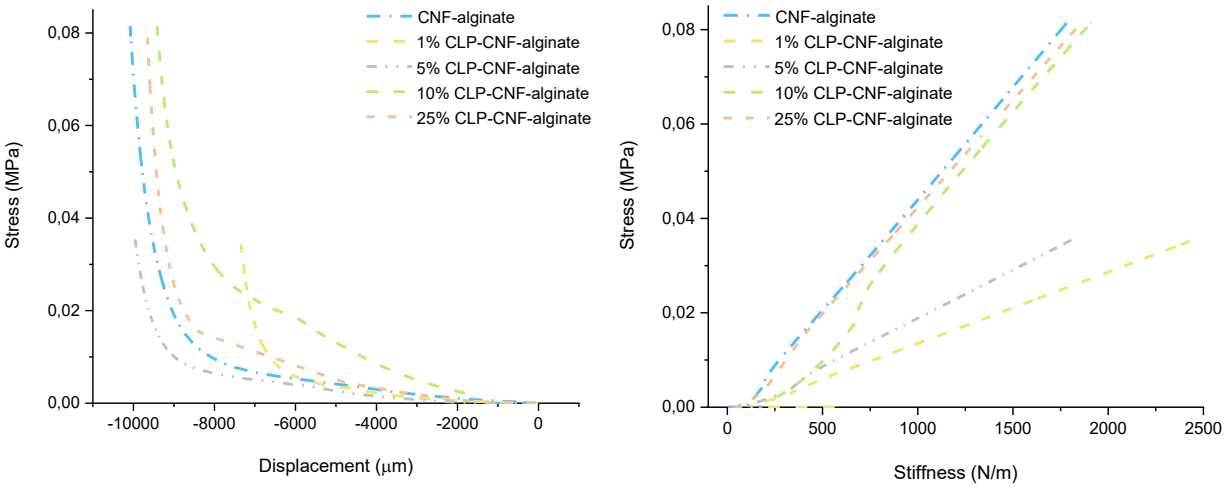

Figure 39. *DMA results in the form of graphs of the 3D bioprinted hydrogels. The graph types of stress (MPa) vs. displacement (µm) and stress (MPa) vs. stiffness (N/m) have been used as an example.*

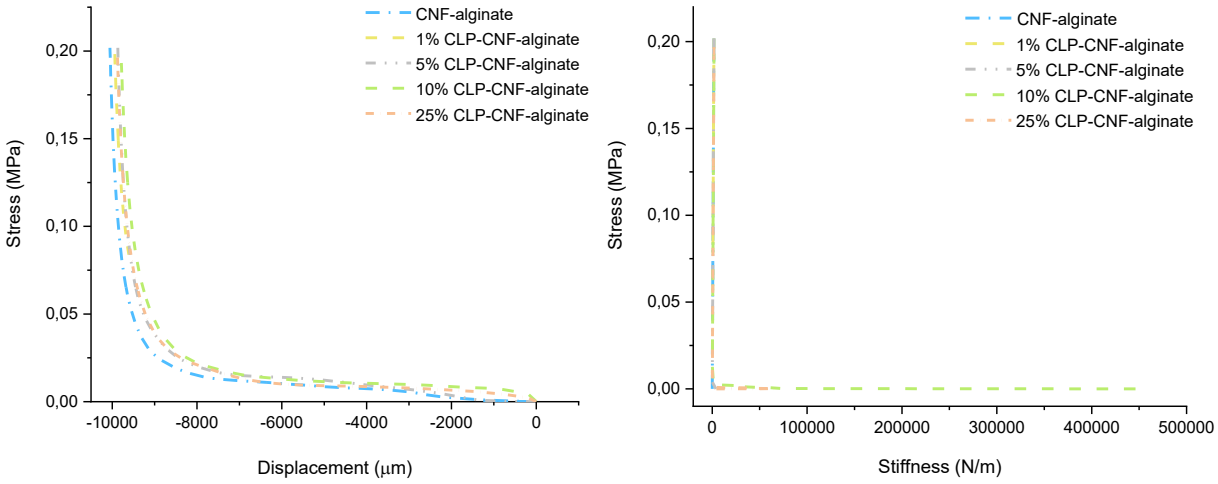

Figure 40. *DMA results in the form of graphs of the freeze-dried and re-wetted hydrogels. The graph types of stress (MPa) vs. displacement (µm) and stress (MPa) vs. stiffness (N/m) have been used as an example.*

Lastly, when having a look at the stiffness graphs (Figures 39 and 40), the amount of applied stress increases with the increased CLP concentrations. Furthermore, the end values of stiffness are in general higher with the 3D bioprinted CLP containing hydrogels than with the 3D bioprinted CNF-alginate hydrogel. Thus, it can be said that the hydrogels with CLPs are in the end stiffer than the CNF-alginate hydrogel, this result being in line also with the experimental observations after 3D bioprinting. However, the stiffness of the hydrogels does not increase sequentially. The stiffness of the hydrogel of 25% CLP-CNF-alginate is very close to the CNF-alginate hydrogel, followed by the hydrogel of 10% CLP-CNF-alginate. This is a surprising outcome, because according to the experimental observations, 25% CLP-CNF-alginate hydrogel is the toughest one. However, as mentioned in the Subchapter 8.2, a high bioink strength may be connected to the high hydrogel resolution. Therefore, the combination of high bioink strength, high resolution, average hydrogel strength and stiffness, and high overall resistance to the applied stress may result in the most stabile and toughest 25% CLP-CNF-alginate hydrogel observed by eye and touching. Another explanation can of course be small errors during the DMA.

However, in the case of the freeze-dried and re-wetted hydrogels, all the hydrogel compositions behave nearly similarly when it comes to the stiffness in the DMA. The amount of applied stress has increased, so the hydrogels need more applied stress for the compression to occur. However, nearly all the applied stress needed to be consumed before the displacement or strain started to increase in the hydrogels. This indicates that the freeze-dried and re-wetted hydrogels are very strong and stiff.

Table 9. *Young's modulus, E, (N/m^2) and slope, k, (Ea/L_0) for the hydrogels after 3D bioprinting and freeze-drying and re-wetting. The highest values have been bolded. The calculations can be seen in the Appendix 6.*

COMPOSITION	YOUNG'S MODULUS (Pa) – 3D BIOPRINTING	YOUNG'S MODULUS (Pa) – RE-WETTING	SLOPE (k) – 3D BIOPRINTING	SLOPE (k) – RE-WETTING
CNF-ALGINATE	0,008	$1,3*10^6$	0,001	391,3
1% CLP-CNF-alginate	121,2	$1,8*10^6$	7,1	545,5
5% CLP-CNF-alginate	37,4	$1,3*10^6$	2,9	388,9
10% CLP-CNF-alginate	**2 946,7**	**$133,3*10^6$**	**208,3**	**6000,0**
25% CLP-CNF-alginate	1 456,0	$4,3*10^6$	102,9	1625,0

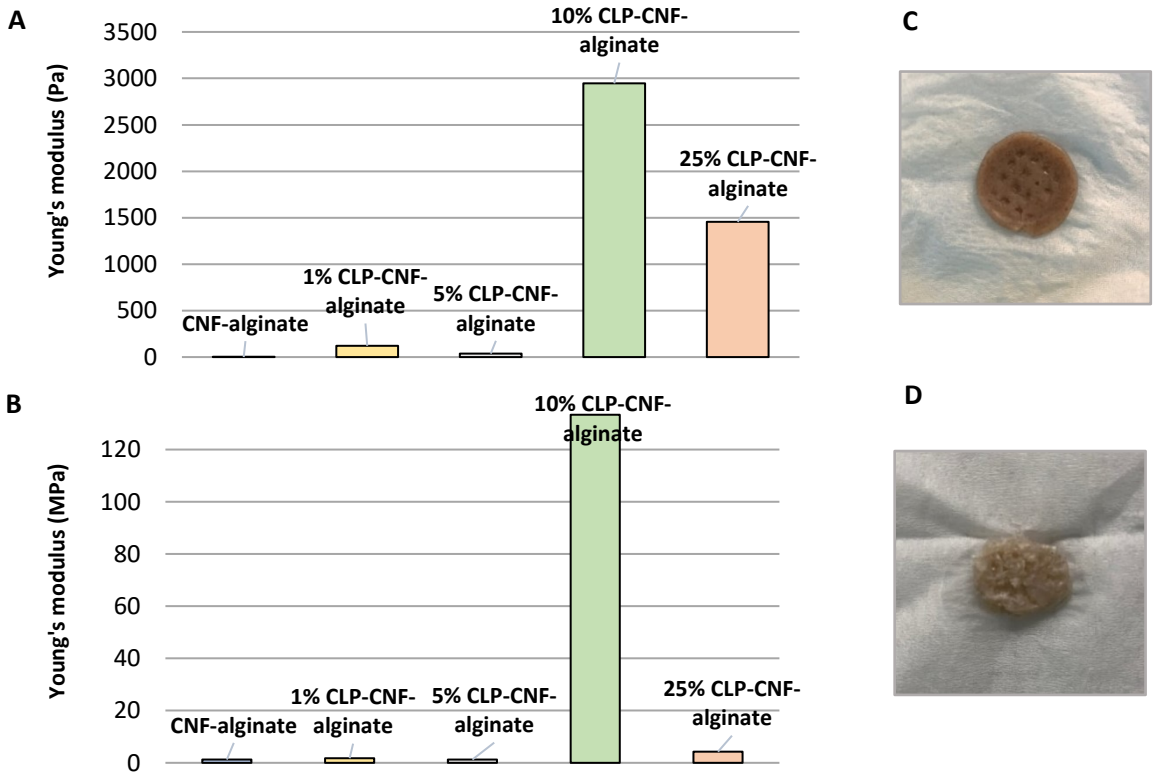

Figure 41. *Data showing the variations in the young's modulus, E, (MPa) of the hydrogels after 3D bioprinting and freeze-drying and re-wetting.* **A.** *The variations in the Young's modulus, E, (MPa) of the hydrogels after 3D bioprinting.* **B.** *The variations in the Young's modulus, E (MPa), of the hydrogels after freeze-drying and re-wetting.* **C.** *3D bioprinted hydrogel after DMA.* ***D.*** *Freeze-dried and re-wetted hydrogel after DMA.*

According to the Table 9 and Figure 41, the addition of CLPs increases the value of E and k of the bioprinted hydrogels, together with the re-wetted and freeze-dried hydrogels, indicating the improved strength and stiffness. E stands for the mechanical strength, whereas k reveals the speed of the increase in this strength. Nevertheless,

the exceptionally high peak in the hydrogel strength occurs in the case of the 10% CLP-CNF-alginate hydrogel, after which the hydrogel strength starts to decrease. This peak seems an outlier and overall, the values are slightly smaller when compared to the ones in the literature (Lê et al., 2018), which may be due to the errors, an unintentional neglicence for example in cutting the hydrogels, or the lack of repetition during the DMA. The measurements were conducted for the fresh, 3D bioprinted hydrogels twice and for the freeze-dried and re-wetted hydrogels only once due to the lack of time. Therefore, the reliability of these measurements may have suffered.

The literature findings offer a slightly different approach. According to Bian et al. (2018), the addition of lignin to the CNF-films decreased their mechanical properties, considering tensile strength and Young's modulus, probably due to the lignin's ability to interfere the hydrogen bonds between the CNF fibres. The results are also in line with the ones obtained by Lê et al. (2018) who investigated that the increased CLP concentrations first increased and later systematically decreased the tensile strength and Young's modulus of the LCNF films, the value of Young's modulus being at its highest at the lignin concentration of 1.7% (Lê et al., 2018). Last but not least, in the article of Wang et al. (2016), the addition of lignin first slightly increased the Young's modulus and thus mechanical properties, e.g. stiffness, of the chitosan fibres, followed by the maximun peak of E at around 3 wt%, and, in the end, a sharp decrease (Wang et al., 2016). The increase in E was due to the well dispersed lignin on the surface of the chitosan fibres, whereas the sharp decrease in E with the increased lignin concentration was caused by the agglomerations and thus, poor dispersibility of the lignin, which also reduced the contact between lignin and the chitosan fibres (Wang et al., 2016). However, the general strength and stiffness of the chitosan fibres were reported to be higher than the strength and stiffness of the chitosan fibres alone (Wang et al., 2016), likewise in this Master's thesis.

Therefore, in the case of the CLP-CNF-alginate hydrogels of the present work, it is evident that the addition of CLPs increases the mechanical strength and stiffness of the hydrogels, while the agglomeration and poor dispersibility of the CLPs onto the

CNF fibres with the high CLP concentrations decrease the mechanical strength of the hydrogels up to certain extent. Nevertheless, the timing and the intensity of this decrease in mechanical strength due to the interference of the hydrogen bonds between the CNF fibres or agglomeration of CLPs is unclear. In the Chapter 9, it was already evaluated that the covalent bonds between alginate and the CNF fibres are formed after cross-linking with 0.09 M $CaCl_2$. In the previous reference articles, the studies were performed only between lignin or CLPs and CNF fibres, without this third material. Therefore, it is logical that the existence of alginate and the covalent bonds hinder the interfering effect of CLPs and the agglomeration of CLPs onto the CNF fibres, at the same time maintaining the mechanical strength and stiffness of the hydrogels for longer periods. This would most probably move the decrease in mechanical strength to the higher CLP concentrations. This transfer can already be seen in the present work, because the significant decrease in the mechanical strength occurred with the CLP concentration of 25%, whereas for example in the article of Lê et al. (2018), this decrease took place already at lignin concentration of 3.1% and 4.9%. However, more studies and more repetition need to be conducted to ensure the exact effect of covalent bonds between alginate and the CNF fibres on the mechanical properties of CLP-CNF-alginate hydrogels.

When having a closer look at the Table 9 and Figure 41, the Young's modulus and slope are exceptionally high in the case of the hydrogels after freeze-drying and re-wetting than straight after 3D bioprinting. Fastly thinking, these are slightly surprising results, because freeze-drying shrinks the hydrogels and seems to deteoriorate them by changing the shape and the surface of these hydrogels. However, it is true that the freeze-dried hydrogels together with the freeze-dried and re-wetted hydrogels feel tougher and stiffer when touched in comparison to the 3D bioprinted hydrogels. According to the Figure 41, the hydrogels after freeze-drying and re-wetting are less pressed, which is also an indication of a stronger material.

After a literature search, the freeze-drying results are reasonable. According to Sornkamnerd et al. (2017), the addition and existence of pores in the lateral direction in the hydrogels increases the hydrogel strength. One of the simplest methods for

forming these pores is freeze-drying that constructs anisotropic pores on the side faces of the water-swollen, layered hydrogels, but not on the top or bottom faces of these hydrogels (Sornkamnerd et al., 2017). The formation of pores is probably due to the ice crystals, which make the material accumulate into the areas between them (Shao et al., 2015), whereas the fibres are oriented in the tightly packed lamellar direction (Shao et al., 2015), increasing the mechanical strength of the hydrogels. The mechanical strength is also increased due to the different moisture content of the hydrogels, because an aqueous environment is known to decrease the mechanical strength (Si et al., 2017), and freeze-drying removes the water from the hydrogels. Another reason is the amount of cross-linking in the hydrogels, the bigger amount of cross-linking leading to the formation of larger crystal templates and therefore, larger pores upon freeze-drying (Hossen et al. 2018).

As a conclusion, the rough feeling and the small irregularities on the side faces of the freeze-dried hydrogels in this Master's thesis have most probably been due to pores, and thus, it is natural that the freeze-dried and re-wetted hydrogels of the present work are stronger and stiffer when compared to the hydrogels measured straight after 3D bioprinting. Furthermore, as explained earlier, the addition of CLPs starts more and more to interfere the hydrogen bonds between the CNF fibres, which in turns increases the mobility of the hydrogel material, increasing the number and size of the pores upon freeze-drying, and further increasing the mechanical strength of the freeze-dried and re-wetted hydrogels.

APPENDIX 6.

Equation (2) for the Young's modulus, E, and calculations for the E and slope, k, in the DMA.

$$E = \frac{F * L_0}{\Delta L * A} \quad (2)$$

Table 23. *The values used in the calculations of E and k of the 3D bioprinted hydrogels.*

	CNF-alginate	1% CLPs-CNF-alginate	5% CLPs-CNF-alginate	10% CLPs-CNF-alginate	25% CLPs-CNF-alginate
F (N)	0.0849	4.3200	0.1410	274.9956	101.911
K	0.0006	7.1429	2.9375	208.93	102.94
ΔL (m)	0.0074	0.6048	0.477	1.32	0.99
L_0 (m)	0.01	0.012	0.009	0.01	0.01
A (m^2)	0.0007	0.0007	0.0007	0.0007	1.0007
E (N/m^2)	**0.08**	**121.2**	**37.4**	**2946.7**	**1456.0**

Table 24. *The values used in the calculations of E and k of the re-wetted and freeze-dried hydrogel.*

	CNF-alginate	1% CLPs-CNF-alginate	5% CLPs-CNF-alginate	10% CLPs-CNF-alginate	25% CLPs-CNF-alginate
F (N)	89.999	119.999	140	1200	130
K	391.3	545.45	388.89	6000	1625
ΔL (m)	0.23	0.22	0.36	0.002	0.008
L_0 (m)	0.01	0.01	0.01	0.01	0.01
A (m^2)	0.0003	0.0003	0.0003	0.0005	0.0004
E (N/m^2)	**$1.3*10^6$**	**$1.8*10^6$**	**$1.3*10^6$**	**$133.3*10^6$**	**$4.3*10^6$**

APPENDIX 7.

Evaluation of the best hydrogels.

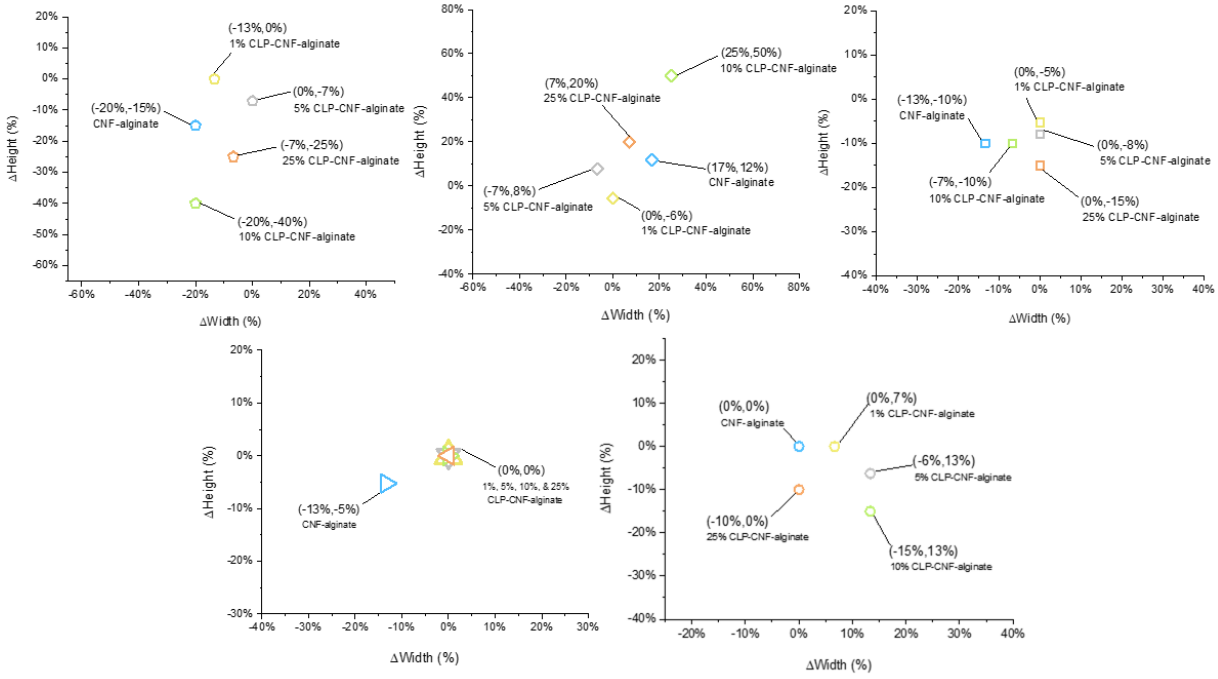

Figure 42. *Comparison of the dimensional changes of the different hydrogel compositions in various storage conditions. Hydrogels with CLP concentrations of 10% and 25% always react approximately the most which results in the change in dimensions. On the other hand, hydrogels with the concentrations of 1% and 5% react approximately the least despite the storage method.*

Table 25. *Comparison of the performance of the different hydrogel compositions in the various measurement conditions. The best hydrogel in the case of each measurement condition has a colour of red, and the second best the colour of blue. The winners have been highlighted with the red square.*

Composition	Dynamic viscosity	Amplitude sweep	Freeze-drying	Re-wetting	Humidity chamber	Salt water solution	Free-standing	DMA
CNF-alginate	5th	3rd	3rd	3rd	5th	5th	1st	3rd
1% CLP-CNF-alginate	4th	1st	2nd	5th	3rd	2nd	2nd	5th
5% CLP-CNF-alginate	3rd	5th	1st	4th	4th	1st	4th	4th
10% CLP-CNF-alginate	2nd	4th	5th	1st	2nd	4th	5th	1st
25% CLP-CNF-alginate	1st	2nd	4th	2nd	1st	3rd	3rd	2nd